H. A. H. SAADAWI

ATILIM UNIVERSITY 2022

# A STUDY ON THE WIRE ARC ADDITIVE MANUFACTURING OF DUPLEX STAINLESS STEEL PLATES: OPTIMIZATION OF PROCESS PARAMETERS AND INVESTIGATION OF MECHANICAL PROPERTIES

THE GRADUATE SCHOOL OF NATURAL AND APPLIED SCIENCES
OF
ATILIM UNIVERSITY

HASSAN A. H. SAADAWI

A DOCTOR OF PHILOSOPHY THESIS
IN
MODELING AND DESIGN OF ENGINEERING SYSTEMS
(MAIN FIELD OF STUDY: METALLURGICAL AND MATERIALS ENGINEERING)

JANUARY 2022

# A STUDY ON THE WIRE ARC ADDITIVE MANUFACTURING OF DUPLEX STAINLESS STEEL PLATES: OPTIMIZATION OF PROCESS PARAMETERS AND INVESTIGATION OF MECHANICAL PROPERTIES

A THESIS SUBMITTED TO
THE GRADUATE SCHOOL OF NATURAL AND APPLIED SCIENCES
OF
ATILIM UNIVERSITY

BY

HASSAN A. H. SAADAWI

IN PARTIAL FULFILLMENT OF THE REQUIREMENTS
FOR
THE DEGREE OF DOCTOR OF PHILOSOPHY
IN
MODELING AND DESIGN OF ENGINEERING SYSTEMS

(MAIN FIELD OF STUDY: METALLURGICAL AND MATERIALS ENGINEERING)

JANUARY 2022

Approval of the Graduate School of Natural and Applied Sciences, Atılım University.

Prof. Dr. Ender Keskinkılıç
Director

I certify that this thesis satisfies all the requirements as a thesis for the degree of **Doctor of Philosophy in Modeling and Design of Engineering Systems (Main Field of Study: Metallurgical and Materials Engineering), Atılım University.**

Prof. Dr. Ender Keskinkılıç
Program Chair

This is to certify that we have read the thesis A STUDY ON THE WIRE ARC ADDITIVE MANUFACTURING OF DUPLEX STAINLESS STEEL PLATES: OPTIMIZATION OF PROCESS PARAMETERS AND INVESTIGATION OF MECHANICAL PROPERTIES submitted by HASSAN A. H. SAADAWI and that in our opinion it is fully adequate, in scope and quality, as a thesis for the degree of Doctor of Philosophy.

Asst. Prof. Dr. Kâzım Tur
Co-Supervisor

Assoc. Prof. Dr. Erkan Konca
Supervisor

**Examining Committee Members:**

Assoc. Prof. Dr. Erkan Konca
Met. & Materials Eng. Dept., Atılım University

Prof. Dr. Bilgehan Ögel
Met. & Materials Eng. Dept., METU

Prof. Dr. C.Hakan Gür
Met. & Materials Eng. Dept., METU

Asst.Prof. Dr. Hakan Kalkan
Manufacturing Eng. Dept., Atılım University

Asst.Prof. Dr. Ozan Özkan
Met. & Materials Eng. Dept., Atılım University

**Date: January 20, 2022**

I declare and guarantee that all data, knowledge and information in this document has been obtained, processed and presented in accordance with academic rules and ethical conduct. Based on these rules and conduct, I have fully cited and referenced all material and results that are not original to this work.

Name, Last Name : HASSAN SAADAWI

Signature :

## ABSTRACT


### A STUDY ON THE WIRE ARC ADDITIVE MANUFACTURING OF DUPLEX STAINLESS STEEL PLATES: OPTIMIZATION OF PROCESS PARAMETERS AND INVESTIGATION OF MECHANICAL PROPERTIES

SAADAWI, HASSAN
PhD in Modeling and Design of Engineering Systems (MODES)
Supervisor: Assoc. Prof. Dr. Erkan Konca
Co-Supervisor: Asst.Prof.Dr. Kâzım Tur
January 2022, 140 pages

In recent years, additive manufacturing (AM) for metals, which is used to create products using layer-by-layer deposition of materials, has been a subject of interest as a means of enhancing the efficiency of manufacturing processes in various industries. In this thesis, super duplex stainless steel parts have been wire arc additively manufactured (WAAM) using the cold metal transfer welding technique. To obtain the optimum combination of additive manufacturing parameters (voltage, current and speed) that yields the desired bead quality, response surface method has been used to build statistical models based on numerical simulation of additive welding process. COMSOL Multiphysics 5.5 software has been used to perform the experimental instead of real process and Expert-Design software was used to obtain the statistical models. The optimal values of the controlled variables were found as 200 amperes and 15 volts for current and voltage, and 10 mm/s for welding speed. Then, the fracture toughness tests using the single edge notched tension (SENT) specimens were implemented at a sub-zero temperature. Fracture toughness data has been used to establish crack-growth resistance curves for both, as-received rolled plate and additively manufactured parts and compare the results based on J-integral (energy release rate). The J-integral value at the initiation of stable crack growth (Ji) of SDSS Grade 2507 as-received plate specimens is approximately 17% higher than the ($J_i$) value of WAAM’d DSS Grade 2209 and 31% higher than the ($J_i$) value of WAAM’d SDSS Grade 2509.


**Keywords:** Additive Manufacturing, Super Duplex Stainless Steel, Cold Metal Transfer Welding, Response Surface Method.

# ÖZ

## TEL ARK EKLEMELİ İMALAT YÖNTEMİYLE DUBLEKS PASLANMAZ ÇELİK PLAKA ÜRETİMİNDE PROSES PARAMETRELERİNİN OPTİMİZASYONU VE PLAKA MEKANİK ÖZELLİKLERİNİN İNCELENMESİ

SAADAWI, HASSAN

Doktora, Mühendislik Sistemlerinin Modellenmesi ve Tasarımı Ana Bilim Dalı
Tez Yöneticisi: Doç.Dr. Erkan Konca
Ortak Tez Yöneticisi: Dr. Öğr.Üyesi Kâzım Tur
Ocak 2022, 140 sayfa

Son yıllarda, malzemelerin katman katman biriktirilmesi yoluyla ürünler oluşturmak için kullanılan eklemeli imalat (Eİ), çeşitli endüstrilerde üretim süreçlerinin verimliliğini artırmanın bir yolu olarak ilgi konusu olmuştur. Bu tezde, süper dubleks paslanmaz çelik plaka parçalar soğuk metal transferi kaynak tekniği kullanılarak tel ark eklemeli imalat (WAAM) ile elde edilmiştir. İstenen kaynak kalitesini veren eklemeli üretim parametrelerinin (voltaj, akım ve hız) optimum kombinasyonunu elde etmek için, eklemeli kaynak işleminin nümerik simülasyonuna dayalı istatistiksel modeller oluşturmak üzere yanıt yüzeyi yöntemi kullanılmıştır. Deneysel süreci çalışmak üzere COMSOL Multiphysics 5.5 yazılımı ve istatistiksel modelleri elde etmek için Expert-Design yazılımı kullanılmıştır. Kontrol edilen değişkenlerden akım ve gerilim için optimum değerler sırasıyla 200 amper ve 15 volt, kaynak hızı için ise 10 mm/sn olarak bulunmuştur. Daha sonra, sıfır altı sıcaklıklarda tek kenar çentikli çekme (SENT) numuneleri kullanılarak kırılma tokluğu testleri gerçekleştirilmiştir. Kırılma tokluğu verileri, hem haddelenmiş plaka hem de eklemeli imalat ile üretilmiş plaka parçalar için çatlak ilerleme direnci eğrileri oluşturmak ve J-integraline (enerji salım hızı) dayalı sonuçları karşılaştırmak için kullanılmıştır. SDSS Grade 2507 haddelenmiş plaka numuneleri için kararlı çatlak büyümesi başlangıcındaki J-integral değeri (Ji), WAAM DSS Grade 2209'un (Ji) değerinden yaklaşık %17 ve WAAM SDSS Grade 2509'un (Ji) değerinden ise %31 daha yüksek olarak belirlenmiştir.

**Anahtar Kelimeler**: Eklemeli İmalat, Süper Dubleks Paslanmaz Çelik, Soğuk Metal Transfer Kaynağı, Tepki Yüzey Yöntemi.

# DEDICATION

I would like to dedicate this small piece of work to

My mother soul, My father soul and My wife and children

## ACKNOWLEDGMENTS

Thanks to Allah almighty who enabled me to finish my thesis successfully. It is a privilege for me to express my sincere gratitude to my thesis supervisors **Assoc.Prof.Dr. Erkan Konca** and **Asst.Prof. Dr. Kâzım Tur** for their supervision, guidance, training, help and continuous encourage during my work. My gratitude is also extended to my committee members: **Prof. Dr. Bilgehan Ögel** and **Asst.Prof. Dr. Ozan Özkan** for their comments and suggestions during all phases of thesis. I am grateful to all my thesis committee members for their contributions. I also would like to express my appreciation and gratefulness to **Prof. Dr. C. Hakan Gür,** the chair of the Department of Metallurgical and Materials Engineering, and the director of Welding Technology and Non-Destructive Testing Research/ Application Center (KTTMM) at Middle East Technical University, **Dr. Koray Yurtışık** the head of Welding R&D unit at KTTMM, engineers and technicians of KTTMM who made all possible faithfully to help me especially, **Eng. Mine Kalkancı** and **Eng. Batuhan Ersan**. Finally, my appreciation goes to my parents, my wife, my children and my brothers who encouraged and supported me throughout the time of this work.

## TABLE OF CONTENTS

## LIST OF FIGURES

## LIST OF TABLES

## LIST OF SYMBOLS AND ABBREVIATIONS

| | | |
|---|---|---|
| AM | : | Additive Manufacturing |
| PBF | : | Powder Bed Fusion |
| DED | : | Directed Energy Deposition |
| WAAM | : | Wire Arc Additive Manufacturing |
| SDSS | : | Super Duplex Stainless Steels |
| CMT-W | : | Cold Metal Transfer Welding |
| PREN | : | Pitting Resistance Equivalent Number |
| HAZ | : | Heat Affected Zone |
| SENT | : | Single Edge Notched Tension |
| q | : | Heat Flux ($W/m^2$) |
| Q | : | Power of Heat Source (W) |
| CMOD | : | Crack Mouth Opening Displacement (mm) |
| CTOD | : | Crack Tip Opening Displacement (mm) |
| J | : | J-integral Fracture Toughness (N/mm) |
| K | : | Stress intensity factor ($N/mm^{1.5}$) |
| $a_0$ | : | Initial crack length (mm) |
| $a_f$ | : | Final crack length (mm) |
| E | : | Modulus of elasticity (GPa) |
| Jel | : | Elastic component of J (N/mm) |
| Jep | : | Plastic component of J (N/mm) |
| Up | : | Area under the plastic part of the load - CMOD curve (N·mm) |
| np | : | Dimensionless function of geometry |

# CHAPTER 1

# INTRODUCTION

## 1.1 Background

Competition in the manufacturing industry is very harsh and in order to obtain competitive advantages the companies must continuously work on product development. Meanwhile, the companies should also follow the developments in the manufacturing technology. This is because there is a symbiosis between technology and product development, and it is only if both are concurrently enhanced then successful products can be accomplished with optimal lead time [1].

In recent years, additive manufacturing (AM) for metals has been a subject of great interest as a means of enhancing the efficiency of manufacturing processes in various industries, such as aircraft, military, automotive, oil, medical [2, 3]. AM is the formalized term for what was originally called as rapid prototyping or 3D printing, and today it is commonly used to create products using layer-by-layer deposition of materials. Metal AM process can be broadly classified into two groups, Powder Bed Fusion Additive Manufacturing (PBF) and Directed Energy Deposition Additive Manufacturing (DED). In PBF AM, material in powder shape is fused in layers by a heat source. In the DED AM, the products are produced by adding material in the shape of powder, wire or sheets in layers and fused with a heat source [2, 4].

Among various AM processes, wire arc additive manufacturing (WAAM) deposits a metal wire using an arc heat source. In the WAAM process, a traditional welding machine may be used as a heat source that decreases the initial investment costs compared to the laser and electron beam heat sources. In addition, the cost of raw materials of the wire type is roughly 10 per cent of the cost of raw materials of the powder type. The WAAM process therefore produces a high deposition rate at a low cost, making it a highly favored process for the manufacturing of large components using expensive materials [3, 5].

Today, WAAM has become a popular manufacturing tool for various engineering materials such as titanium, aluminum, nickel alloys and steels. Compared to traditional subtractive manufacturing, WAAM technology can reduce fabrication time and post-machining time depending on the component size [1, 6].

More recently, there has been an increasing interest in applying AM to super duplex stainless steels (SDSS) due to the greater demand for SDSSs in the offshore applications. Since SDSSs have excellent mechanical properties and corrosion resistance, they are suitable for use in harsh corrosive environments containing chlorides such as seawater [7, 8]. It is well known that an adequate percentage of austenite ($\gamma$) and ferrite ($\alpha$) phases in the resulting duplex stainless steels microstructure plays a key role in the final properties needed. The ferrite phase offers strength and corrosion resistance while the austenite phase increases the ductility. However, when SDSS parts are made using additive manufacturing technology the subsequent pass reheats the metal deposited by the preceding pass. As result, undesired ratio of $\alpha/\gamma$ phases is obtained since austenite fraction is increased due to precipitation of secondary austenite [8, 9].

As mentioned earlier, SDSSs are used in marine structures where low temperatures are not uncommon. At sub-zero temperatures, the fracture mechanism for ferrite goes from ductile to brittle with low fracture deformation. The move from one mechanism to another is called as the ductile-to-brittle transition [10]. Therefore, precise prediction of fracture toughness plays a critical role in any structural integrity assessment. These structural integrity assessments rely on the assumption that the fracture resistance of the product is equal to the resistance obtained from the toughness test specimen [11].

The focus of the present work has been the study of the fracture toughness of wire arc additively manufactured super duplex stainless steels at sub-zero temperatures using single edge notched tension (SENT) specimens. To obtain the optimum combination of additive manufacturing parameters that yield the desired bead quality, response surface method has been used to build statistical models. Numerical simulation was used to perform the experimental instead of real welding process. Experimental work of this thesis study has been carried out at the Welding Technology and Non-Destructive Testing Research/Application Center at Middle East Technical University (KTTMM-METU) in Ankara, Turkey.

## 1.2 Relevant Studies

Few studies have investigated additive manufacturing of duplex stainless steels. Davidson et al. [12] fabricated super duplex stainless steels (type-2507) using selective laser melting (SLM) and found that the as-built piece contained 93% ferrite with some $Cr_2N$ particles. Heat treatment at 1040°C reduced the ferrite fraction to 55%. Hengsbach et al. [13] used SLM technology to produce a type-2205 DSS piece, where 99% ferrite was obtained, while heat treatment at 1000°C reduced the ferrite fraction to 66%. Posch et al. [14] investigated WAAM of DSS using 2209 grade filler metal and cold metal transfer (CMT) welding process. The microstructure obtained had a ferrite number of 30 FN (standardized value which is related to the ferrite content in austenitic and duplex stainless steels weld metal) and mechanical properties were comparable with the filler metal. Eriksson et al. [15] also studied the CMT process for the additive manufacturing of SDSS, where a 20% ferrite fraction and acceptable mechanical properties were achieved. Papula et al. [16] produced a high-density duplex stainless steel 2205 specimens (<0.03% porosity) by selective laser melting (SLM) and good mechanical properties were achieved. The microstructure was almost fully ferritic, but the desired microstructure was obtained by post-processing heat treatment. Hejripour et al. [17] studied the thermal behavior of two different parts (Wall and Tube) made of 2209 duplex stainless steel (DSS) using GMAW process. They used the thermal cycle data to study the evolution of microstructure and found that slow cooling significantly promoted austenite formation in a ferrite matrix. Hosseini et al. [18] studied the microstructures of 2209 duplex stainless steel additively manufactured by GMAW technique with high and low heat input and they found that the austenite fraction increased up to 10% in the reheated beads rather than first bead that increased up to 8% for high and low heat input. Stützer et al. [19] used GMAW-cold wire AM technique to improve alloy compositions of DSS by mixing filler wires with different nickel contents. They melted approximately 23% cold wire with the wire electrode in the AM experiments and made it possible to achieve 39–72% ferrite in the specimens. Lervåg et al. [20] fabricated additively manufactured super duplex stainless steel parts using CMT process with three different heat inputs and studied the effect of heat input on the mechanical properties. They found that a slight reduction in toughness occurs when the heat input was increased, also yield strength, tensile strength and hardness were decreased with increasing heat input.

## 1.3 Knowledge Gap

Duplex stainless steels are increasingly used for marine applications which are exposed to low service temperatures. Cold metal transfer wire arc additive manufacturing has a very good potential to produce DSS components. However, there is a significant lack of information/knowledge on different aspects of this manufacturing technique that must be clarified/explored before it can be proposed to be used in practice. For example, the effects of wire arc welding process parameters on the distortion of SDSS parts produced by WAAM have not been studied yet. In addition, the knowledge on the mechanical properties of SDSS components produced by WAAM, especially their fracture behavior at sub-zero temperatures, is very limited.

## 1.4 Objectives

The objectives of this research are:

- To perform heating-cooling/thermal cycle simulations in order to find the optimum combination of wire arc welding process parameters that minimize the distortion of DSS parts produced by WAAM.
- To conduct WAAM of DSS Grade 2209 and Grade 2509 using CMT welding technology with optimized process parameters.
- To examine the microstructural evolution and to determine the strength of DSS parts produced by CMT WAAM.
- To perform and evaluate fracture toughness testing of additively manufactured DSS at sub-zero temperatures using the single edge notched tension (SENT) specimens and compare the results with those of as received DSS Grade 2507 rolled plate..

## 1.5 Details of Thesis Format

The thesis starts with the background literature relevant to this research project in Chapter 2. It includes a history of AM and a few of the technologies available today. This chapter also briefly describes the properties of duplex stainless steel, which lead into the specific super duplex stainless steel. The fracture mechanics analysis approach employed in this project is also detailed. The simulation works are presented in

Chapter 3. The experimental procedures of the project, as well as the equipment used to achieve results, are described in Chapter 4. Chapter 5 discusses the results of all experiments and the information that can be derived from them. In Chapter 6, the thesis is ultimately concluded together with suggestions for future work.

# CHAPTER 2

# THEORY

## 2.1 General

This chapter provides a theoretical background for,

- Additive manufacturing technologies, concepts and classifications including cold metal transfer, as the wire arc additive manufacturing process.
- Super duplex stainless steel, as the material
- Fracture toughness, as the property

## 2.2 Additive Manufacturing Technologies

Additive Manufacturing (AM) has been in existence for three decades and was initially used for model making and prototyping. AM technology has now evolved into a rapid manufacturing process [2]. AM refers to a collection of techniques used to create three-dimensional parts by depositing and melting successive layers of base material using an additive technique. AM is seen as opposed to conventional subtractive processes using machining operations (such as turning, milling, grinding) or molding methods (such as pressing, casting, injection molding). AM processes are often described by terms such as 3D printing, rapid prototyping, direct digital manufacturing, fast manufacturing, and solid freeform manufacturing. Although AM does not replace any of the conventional manufacturing processes, it represents a key enabler for development and innovation, and it also adds capacity to complement traditional processes as well. Therefore, AM is receiving more and more attention and effort around the world because there is a tremendous worldwide interest in evaluating AM's potential as a useful and possibly disruptive technology. AM technology is rapidly developing and getting more and more integrated into manufacturing industry and our daily lives [21]. AM can handle different kinds of materials such as polymers, ceramics, and metals [2]. Indeed, AM's excitement encompasses many fields, from computer science and product design to new materials and lean engineering [22]. Figure 2.1 shows some applications of AM.

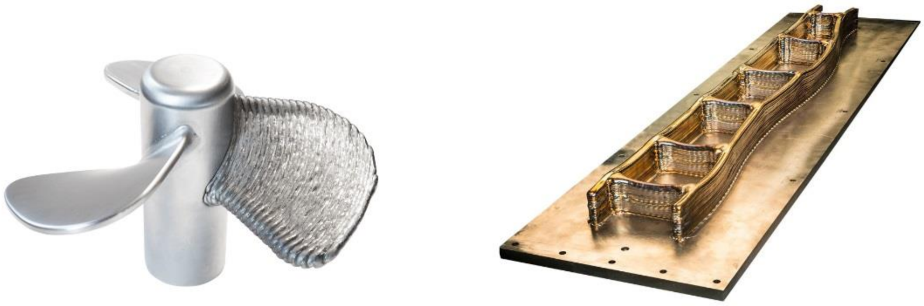

(a) (b)

Figure 2.1 Examples of AM application: (a) steel propeller, (b) titanium structure element of aircraft wing [22]

However, public attention has been focused on AM only in recent years [22]. AM innovations have already developed themselves at the level of actual production in some sectors [22].

One of the current problems for AM is that many traditional manufacturing sectors are not fully aware of, or do not fully understand, how AM can be used. AM will replace some of the production methods, but not all of them, while it has the added potential to complement many of those it cannot replace [22]. AM is much more than a process used to make customized novel items or prototypes. With new developments in AM, we are living in an age at the cusp of industrialized rapid manufacturing taking over as a process for producing many products as well and making designing and creating new ones possible [21].

## 2.3 Benefits and Constraints

### 2.3.1 Benefits of AM Technologies

Nowadays AM of metal parts is well known as an important alternative to traditional processes because of its ability to minimize component costs by minimizing material wastage and time to market. In addition, AM can also enable greater design freedom, which potentially leading to weight savings as well as facilitating the manufacture of complex assemblies that used to consist of many subcomponents [22, 23].

### 2.3.2 Limitations of AM Technologies

In order to take full advantage of AM technology, it is important to be aware of certain limitations of this technology, such as:

- Part size: Part size limited to system size in some AM technologies.
- Processability of different materials: Although many alloys are available, specific approaches are required for difficult-to-weld alloys.
- Post-processing: In some cases, machining is required to achieve better surface finishing or dimensional precision.
- Residual stresses and distortions are major concerns for AM. Part tolerances could be affected. Premature failure has also been an issue [22].

## 2.4 Classification of Additive Manufacturing Technologies

The AM area has been developed over the past two decades as a result of various technologies being researched and developed [2]. In the frame of AM technology, various processes can be described, where a range of materials (including polymers, metals, ceramics and composites), different techniques of deposition and fusion are applied [22]. Because of its intrinsic characteristics, each method is naturally suited to some applications [23]. American Society of Testing Materials (ASTM) Committee F42 has categorized AM processes to seven categories as Vat polymerization, Material jetting, Material extrusion, Sheet lamination, Binder jetting, Powder bed fusion and Directed energy deposition [22].

The uses of metal have been gaining popularity in AM technology. For the AM of metallic parts, AM processes could be classified based on the state of the raw material as liquid, powder and wire based processes as shown in Figure 2.2 [22, 24].

### 2.4.1 Liquid Based Technologies

The application of liquid-based material is relatively new in metal AM. This technology melts the raw material and propels the fused metal droplets to build up a metal component using an electromagnetic field. This speeds up the manufacturing of components with high-intensity [24].

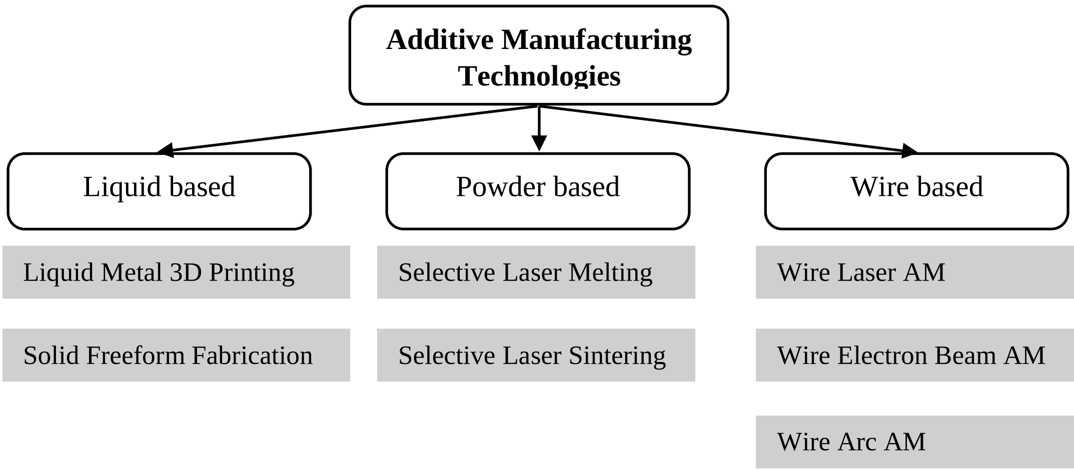


Figure 2.2 Classification of AM processes based on the state of the raw material

### 2.4.2 Powder Based Technologies

Powder bed fusion (PBF) is an additive manufacturing process based on powder as raw material where a source of heat selectively fuses a region of a powder bed. Powder bed fusion is the most commonly used method for metal build up with AM. Although PBF process is suitable for the fabrication of small components because of better geometrical and dimensional accuracy, its deposition rate and the fabricated build volume is relatively low. In order to melt powder bed regions either a laser beam or an electron beam is used [22, 24].

### 2.4.3 Wire Based Technologies

Due to their high potential for use in metal AM, wire based additive manufacturing has been extensively studied recently. A simple system of wire based AM consists of a motion system, heat source and feedstock [23, 24]. Wire based AM includes three different techniques: laser, electron beam and arc welding. Laser and electron beam based techniques are typically the same [24] as schematically represented in Figure 2.3 [22].

## 2.5 Wire Arc Additive Manufacturing (WAAM)

WAAM is a near-net shape AM system that allows complex parts to be built with minimum finishing. The system builds up the components with layer-by-layer deposition of material. Complex parts can be built up with enhanced material properties, and hybrid components can be created. The savings in time and material are expected to make WAAM an attractive option for large part manufacturing [25].

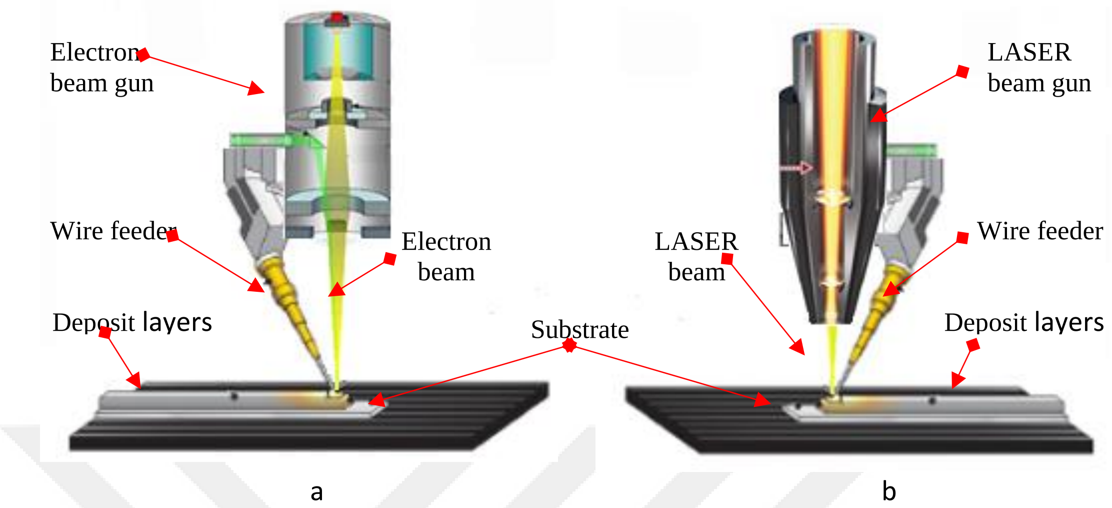


Figure 2.3 Electron beam and Laser-beam AM [22]

WAAM technologies have been investigated to be used as an AM method since 1990s. Recent improvements in welding have made it possible to use a multi-choice welding source instead of a laser or an electron beam source [26]. WAAM uses welding equipment: welding power source, torches and wire feeding systems. Motion can be provided by robotic systems or computer numerical controlled table [22, 24].

High deposition rates, low cost of materials and equipment, and good structural integrity make WAAM a suitable candidate for replacing the current manufacturing process, especially with respect to parts of low and medium complexity. For this AM process, a wide variety of materials are available including steels, stainless steels, nickel and titanium alloys [22, 23, 27].

Residual stresses and distortions are of great concern for the WAAM of large scale components. Distortions result in poor tolerances while residual stresses affect the component's mechanical behavior. In addition, post-processing operations are required due to the poor finish of the surface obtained with WAAM [22].

In the WAAM process, 3D metallic components are built by depositing beads of weld metal layer by layer, using welding processes such as gas metal arc welding (GMAW), gas tungsten arc welding (GTAW), and plasma arc welding (PAW) combined with a motion system [24, 26].

### 2.5.1 GTAW Based WAAM System

GTAW uses a non-consumable tungsten electrode combined with a separately fed wire to produce the weld deposit, as shown in Figure 2.4. During the deposition process, wire feed orientation affects material transfer and the deposit consistency. Back feeding, side feeding, and front feeding can be used. A GTAW torch with a gas lens is used to generate laminar flow of shielding gas to reduce oxidation. Gas lens is one of modern GTAW torch components, composed of a copper body with layered mesh screens of steel or stainless steel [27].

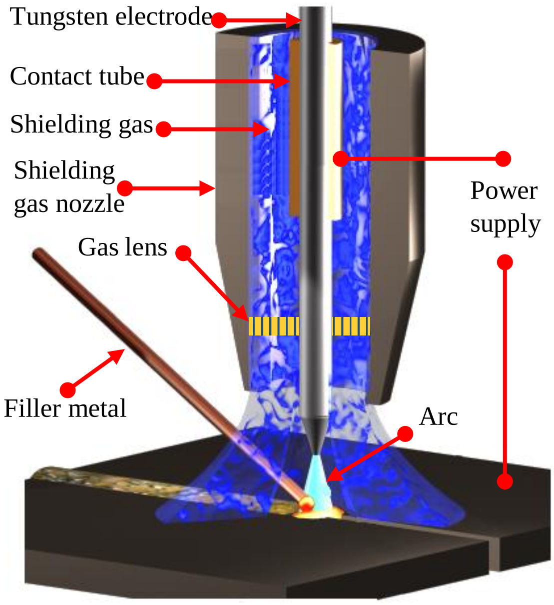


Figure 2.4 Gas tungsten arc welding [27]

### 2.5.2 PAW Based WAAM System

PAW has also been widely studied as a process for the AM processing of metallic materials. In plasma welding, arc energy density can reach three times that of GTAW, resulting in fewer weld distortions and smaller welds with higher welding speeds. Figure 2.5 shows WAAM system based on PAW [27].

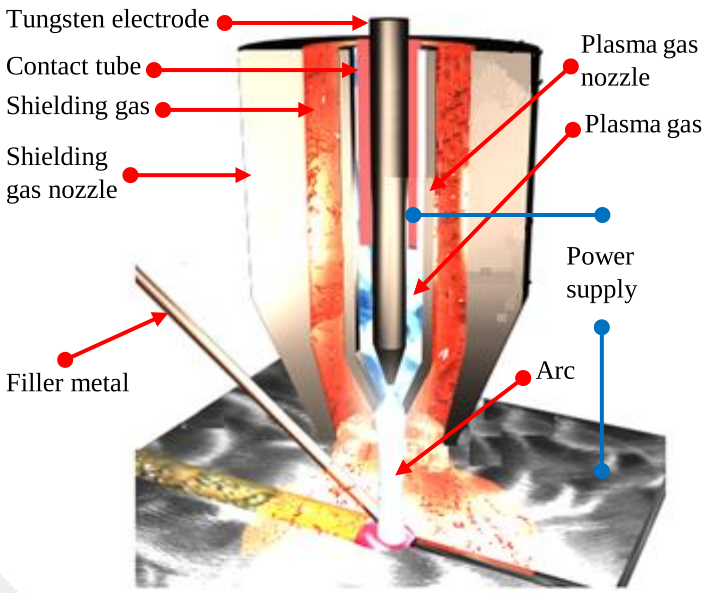


Figure 2.5 Plasma arc welding [27].

### 2.5.3 GMAW Based WAAM System

GMAW is a welding process in which an electric arc is formed between a consumable wire electrode and the substrate metal. The wire is usually perpendicular to the workpiece [27]. GMAW is the most common heat source choice for AM due to its welding wire direct-feeding spool, which is coaxial to the welding torch [24]. As depicted in Figure 2.6, there are four welding modes in GMAW: the globular mode, short-circuiting mode, spray mode, and pulsed-spray mode. Cold metal transfer (CMT) was later introduced as modified GMAW [28]. CMT performs better than GMAW because of its capacity to produce a high deposition rate with a lower heat input [23, 24, 27]. Figure 2.7 shows a GMAW based WAAM system.

## 2.6 Cold Metal Transfer

Cold Metal Transfer welding is a modified GMAW process which was developed by Fronius of Austria in 2004 [29]. An illustration of Fronius CMT welding set-up is shown in Figure 2.8 [30]. CMT can be regarded as a short circuit GMAW method in its most elementary form. GMAW short circuit comprises the lowest range of welding currents and electrode diameters.

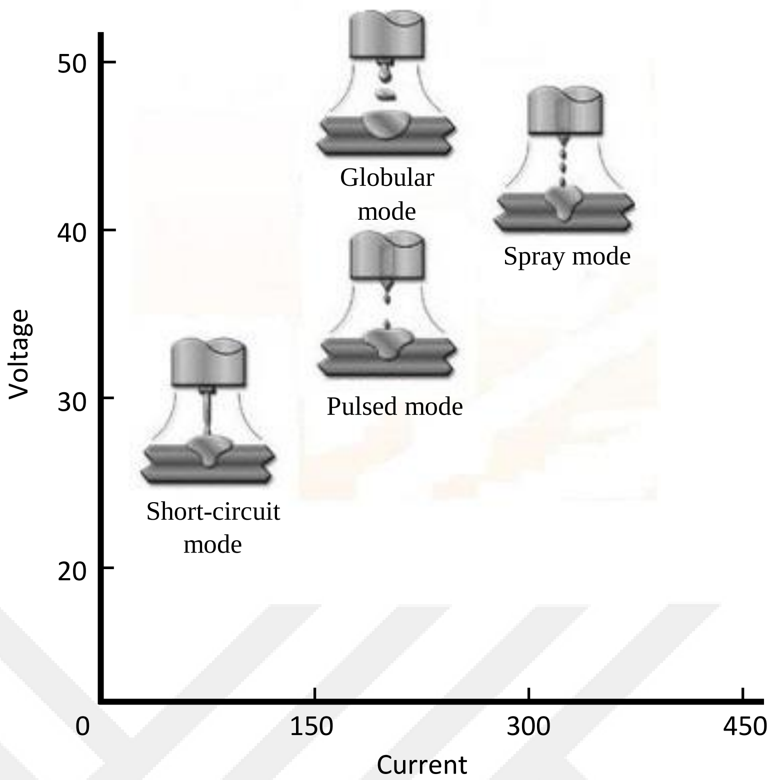


Figure 2.6 GMAW welding transfer modes. [28]

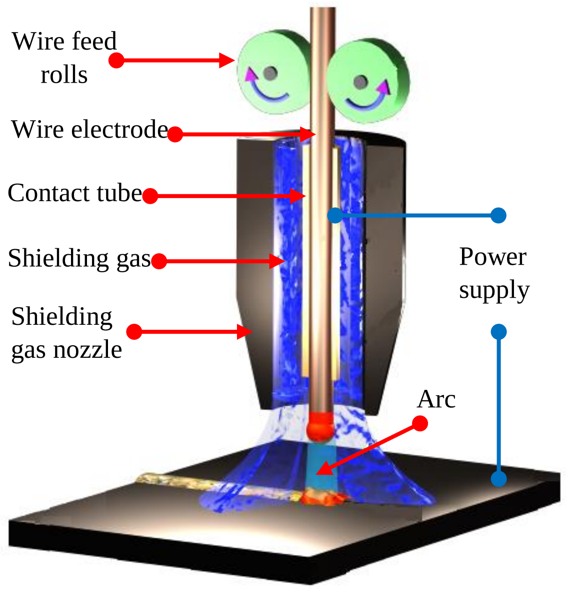


Figure 2.7 Gas metal arc welding [27]

This kind of transfer provides a tiny, quick-freezing deposited metal. During the arcing process, metal is transferred from the wire to the substrate only in a short period of time, when the electrode is in contact with the weld pool; hence the term "short circuit transfer" which means no metal is transferred across the arc gap [31]. It is critical that the current density must be sufficiently high to heat the electrode and facilitate metal transfer, but low enough to reduce spatter caused by violent separation of the metal drop [31].

The CMT unit consists of two separate wire-drives (front and rear), separated by the wire buffer. The front drive (servomotor), located in the torch, (see Figure 2.8-a), drives the wire forth and back at a pace of up to 90 times per second in a dabbing motion. At the same time, the rear drive drives the wire directly from the filler spool within the wire drive. It is important to note that Process Control digitally controls both drives. A wire buffer (Figure 2.8-b) is interposed between the two drives to decouple them from one another to ensure a constant wire feed [31].

Unlike the GMAW, CMT incorporates a digital process-control that detects the short circuit at the workpiece, and then retracts the wire mechanically to help detach the molten droplet. The retraction of the wire significantly reduces the spatter which is usually associated with traditional short circuit GMAW. The second most noticeable difference is a reduction in the thermal input, since the droplet detachment is practically current-free, hence the word “Cold Metal Transfer.” [31].

### 2.6.1 Cold Metal Transfer Welding Cycle

A typical electrical cycle of CMT process can be defined as the time required to deposit a droplet of molten metal on the substrate. Current and voltage waveform analysis is important for the study of the energy distribution of different phases in droplet transfer process. As shown on Figure 2.9, the process is divided into three phases:

(i) The peak current phase: High current with constant voltage causes the easy ignition of the arc and then heats the wire to form a droplet.

(ii) The background current phase: The current is dropped to prevent the globular transfer of the droplet produced on the tip of the wire. This phase continues till short circuiting takes place.

(iii) The short-circuiting phase: The arc voltage is brought to zero in this phase. At the same time, the wire feeder is given a return signal which gives the wire a backdrawing force. This phase helps detachment of the liquid and its transfer onto the substrate [29].

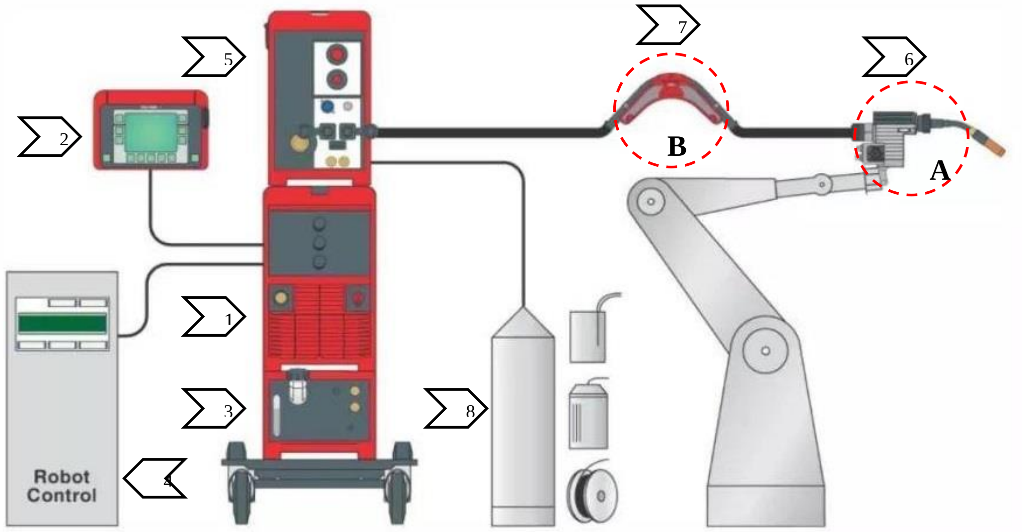


1. Power source
2. Remote-control unit
3. Cooling unit
4. Robot interface
5. Wire feeder
6. Robacta Drive CMT
7. Wire buffer
8. Wire supply

A

B

Figure 2.8 Fronius CMT welding system [30]

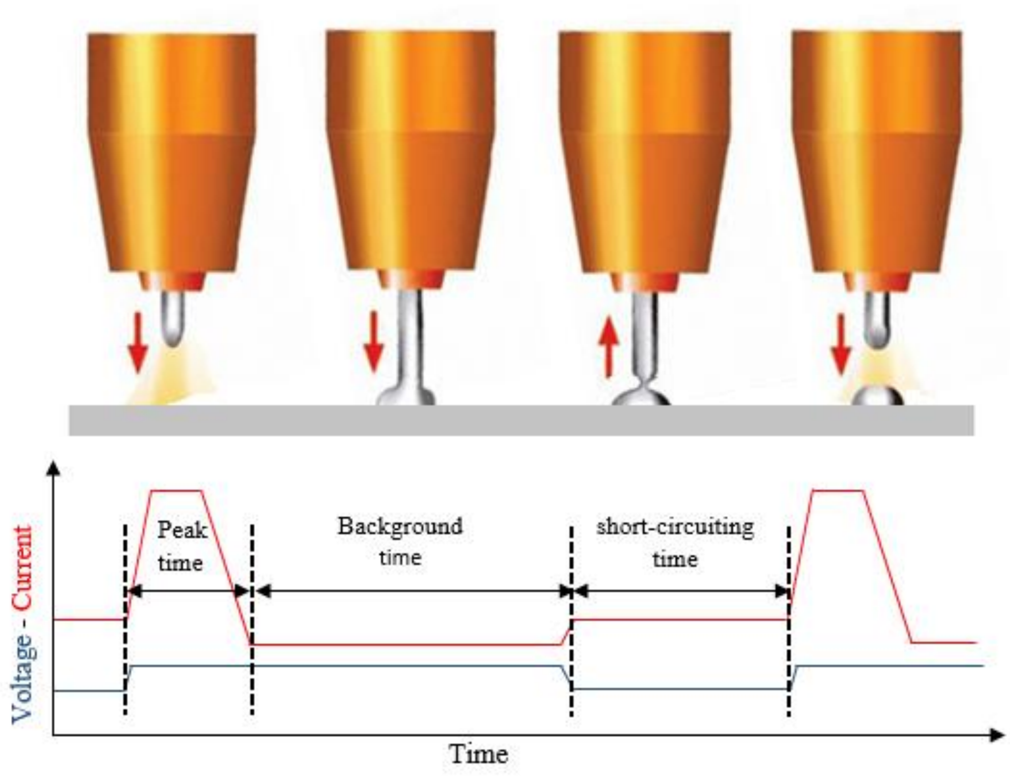


Figure 2.9 CMT welding cycle [29, 31]

### 2.6.2 Cold Metal Transfer Welding Parameters

The most important variables of the CMT process which affect the AM quality are welding current (wire feed speed), arc voltage (arc length), travel speed, electrode extension, torch angle, and electrode diameter. Knowledge and control of these variables are necessary to consistently produce appropriate quality product. Nonetheless, modifying one variable usually involves adjusting additional parameters to maintain an appropriate quality since the variables are not entirely independent of each other [31].

#### 2.6.2.1 Arc Length

With the CMT, the arc length is mechanically acquired and adjusted. That means the arc remains stable irrespective of the surface condition of the workpiece itself. The CMT uses a self-correction mechanism via a constant-potential power source in addition to a mechanical response [31].

#### 2.6.2.2 Wire Feed Speed

With the CMT, current and voltage are linked together via a linear mathematical relationship (proprietary to Fronius International LLC) that integrates voltage and amperage process controls into the feed speed of the wire and depends on the thermal and electrical resistivity properties of the material substrate and filler used [31].

#### 2.6.2.3 Welding Speed

Welding speed in the CMT process affects the weld quality deeply. The deposition rate of filler metal per unit length increases when the welding speed is reduced. As the welding speed increases, the thermal energy per unit length of weld transmitted from the arc to base metal is decreased [31].

## 2.7 The Material; Super Duplex Stainless Steel

### 2.7.1 General

The microstructure of Duplex Stainless Steels (DSS) consists of ferrite and austenite phases as shown in the Figure 2.10. DSSs are considered to be the preferred material for many applications such as marine equipment, chemical, oil and gas industries because they offer a unique combination of corrosion resistance properties and high mechanical properties to be considered when selecting materials [32, 33, 34].

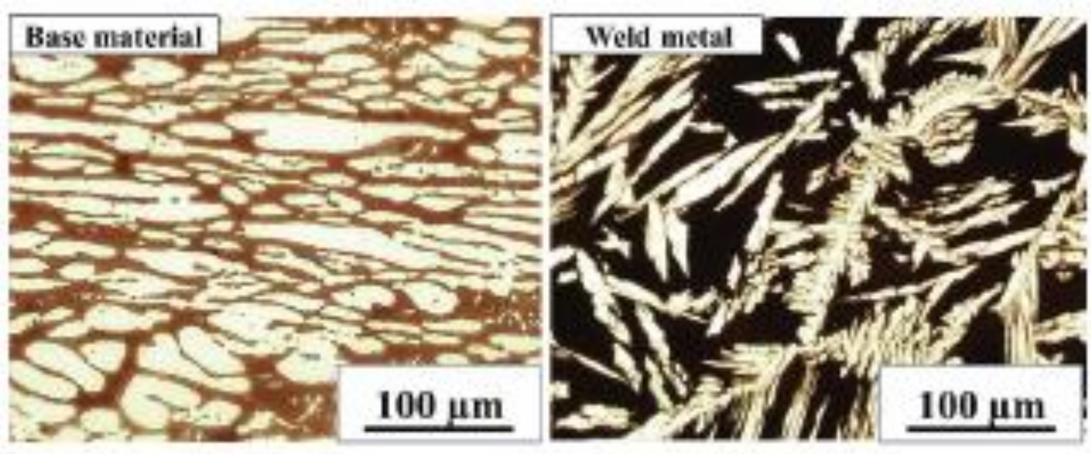


(a) (b)

Figure 2.10 Microstructure of duplex stainless steels: (a) wrought base material and (b) weld metal [35]

A stainless steel's resistance to localized corrosion and mechanical properties is closely related to its alloy content. Chromium (Cr), molybdenum (Mo), and nitrogen (N) are the primary elements which contribute to the pitting corrosion resistance, strength, and toughness. An empirical relationship called the Pitting Resistance Equivalent Number (PREN) was developed to relate the composition of a stainless steel to its relative pitting resistance in solutions containing chloride [36]. For austenitic and duplex stainless steels, the PREN is calculated as follows:

$$PREN = Cr + 3.3(Mo + 0.5W) + 16N \quad (2.1)$$

Where alloying elements are in weight percentages.

### 2.7.2 Brief History

Development of stainless steels in UK and Germany dates back to the first decades of the 20th century. First grades of stainless steel have only been rich in Cr. After the inventions of martensitic and ferritic grades, austenitic grades were developed by Ni alloying and became the most popular stainless steel grades [37].

In stainless steels, there are three main types of microstructures, i.e., ferritic, austenitic, and martensitic. These microstructures could be obtained by adjusting the steel chemistry appropriately. Stainless steels can be classified into several different groups of these three major microstructures which are ferritic stainless steels, austenitic stainless steels, martensitic stainless steels, duplex stainless steels, and precipitation hardening stainless steels [38]. Figure 2.11 includes the most popular diagram developed experimentally by Schaeffler for weld metal, which allows the identification of different categories of stainless steels on the basis of chemical composition [38].

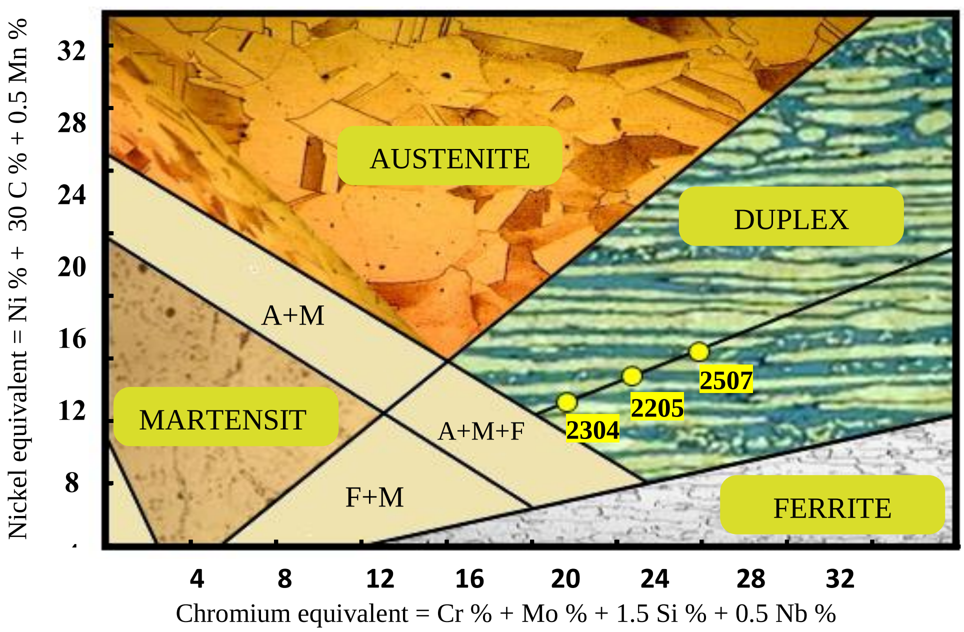


Figure 2.11 Schaeffler diagram [39]

### 2.7.3 Duplex Stainless Steels Grades; Past and Present

Duplex stainless steel is a general term for stainless steels with ferrite and austenite phases having a ratio of approximately 1:1. Various improvements have been made to duplex stainless steel in the course of its history, and it has reached the present day [7]. The material can be made available in as-cast and wrought forms. Both grades are increasingly employed for a wide range of applications, such as heat exchangers, pressure vessels, storage tanks, desalination systems, piping assemblies in off-shore platforms, and reaction vessels as shown in Figure 2.12 [37].

(a)

(b)


(c)

Figure 2.12 Some applications where DSSs are employed; (a) shell-tube-heat-exchanger, (b) pipe line, and (c) food processing.

The development of DSSs could be divided to four generations:

#### 2.7.3.1 First Generation from Dawn -Development of Duplex Stainless Steels

Duplex stainless steel was initially used as a casting in the 1930s. At the beginning, it was difficult to process sheet and tube products. These first-generation duplex stainless steels have sufficient mechanical properties and corrosion resistance for practical use. However, these steels were not sufficient for use in welded structures. The reason for this is that the welded portion has the disadvantage that the mechanical properties and corrosion resistance are greatly reduced as compared to the base metal because of excessively big coarsened ferritic grains in the heat affected zone (HAZ) [7, 34, 38].

#### 2.7.3.2 Second Generation-Ensuring Weldability

With the 70's, new refining processes with VOD (Vacuum Oxygen Decarburization) and AOD (Argon Oxygen Decarburization) in addition to continuous casting allowed the production of much cleaner steels with a very low carbon content (0.03% or less) and a high nitrogen content (0.1% or more) [34, 38]. These second-generation duplex stainless steels like UNS S32205 have been improved in weldability. The above-mentioned problems with HAZ were greatly improved by controlling of N and C contents [7].

#### 2.7.3.3 Third Generation-High Corrosion Resistance

In the 1990s, the need for even more corrosion-resistant duplex stainless steels increased, and third-generation super duplex stainless steels were developed with a high value of pitting corrosion index PREN and are being used in marine oil well-related facilities. By convention, stainless steels with a PREN value of more than 40 are considered super stainless steels, so duplexes in this category are called super duplex stainless steels [7].

#### 2.7.3.4 At Present-Resource Saving and Ultra High Corrosion Resistance

In recent years, the direction of development of duplex stainless steel has largely been focused on higher corrosion resistance. With a pitting resistance of 49, the SAF 2707 hyper-duplex stainless steel has significantly improved corrosion resistance in chloride solutions compared to super duplex stainless steels [7, 40]. Table 2.1 lists the chemical compositions and PREN values of the modern wrought duplex stainless steels. [36]

Table 2.1 Chemical compositions and PREN values of the modern duplex stainless steels [36]

| USN | Grade | C | Cr | Ni | Mo | N | Si | Mn | PREN |
|---|---|---|---|---|---|---|---|---|---|
| **Early grade** | | | | | | | | | |
| S32900 | 329 | 0.08 | 23-28 | 2 - 5 | 1 - 2 | -- | 0.7 | 1 | 32 |
| **Lean duplex** | | | | | | | | | |
| S32304 | 2304 | 0.03 | 21 – 24 | 3 – 5.5 | 0.05-0.6 | 0.05-0.2 | 1 | 2.5 | 28 |
| **Standard duplex** | | | | | | | | | |
| S31803 | 2205 | 0.03 | 21-23 | 4.5-6.5 | 2.5-3.5 | 0.08-0.2 | 1 | 2 | 34 |
| **Super duplex** | | | | | | | | | |
| S32750 | 2507 | 0.03 | 24-26 | 6-8 | 3-5 | 0.2-0.3 | 0.8 | 1.2 | 42.5 |
| **Hyper duplex** | | | | | | | | | |
| S32707 | 2707 | 0.03 | 26-29 | 5.5-9.5 | 4-5 | 0.3-0.5 | 0.5 | 1.5 | 49.2 |

### 2.7.4 Super Duplex Stainless Steel Grades

In the 70s, a famous super duplex grade, which is known as Ferralium 255 (UNS S32550) with 25 % Cr and high Mo additions, was developed by Langley alloy. The grade had nitrogen additions but well below today's levels; it remained difficult to weld. The new generation of super duplex grades was produced in the 90s, with 25-26 % Cr and increased Mo and N contents. These grades include 2507 and Zeron 100. Additions of nitrogen in duplex stainless steels seemed extremely significant. It contributes to many properties particularly in the welded areas, including the high temperature stability of the two-phase microstructure [34]. In addition, nitrogen is also considered to strengthen the localized corrosion resistance (pitting and crevice) properties of the stainless steels. Such two main contributions of nitrogen explain why nitrogen content in duplex grades has been gradually increased to the levels close to the solubility limit value as shown in Figure 2.13 [41]. The solubility limit of nitrogen steadily increases with increase of chromium and molybdenum contents and hence improve the corrosion behavior of the SDSS [34].

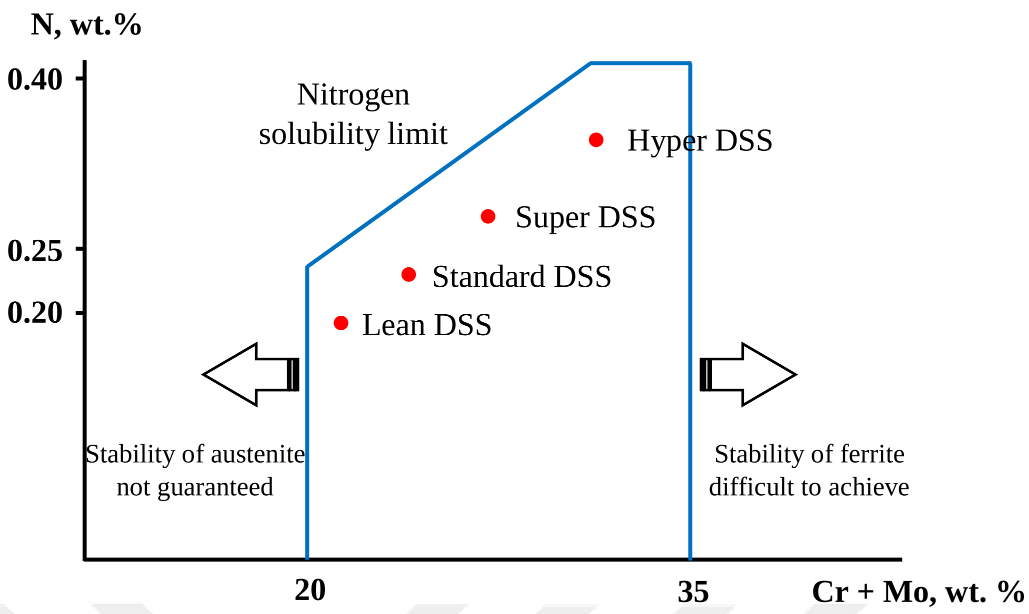


Figure 2.13 The solubility limit of nitrogen in DSS [41]

## 2.8 Physical Metallurgy and Microstructure of SDSS

### 2.8.1 Structure Stability and Solidification Mode

The stainless steel solidification mode is very important as it affects the corrosion and mechanical properties of welded and cast components. The volume fraction of austenite and ferrite are influenced by the solidification mode [42]. The ternary phase diagram of iron-chromium-nickel system is a roadmap of the duplex stainless steels' metallurgical behaviour. A 68% iron section through the ternary diagram (Figure 2.14) shows that these alloys solidify as ferrite (α), which then partially transforms into austenite (γ) as temperature drops, depending on the composition of the alloy. Austenite / ferrite volume fractions are specifically related to composition and temperature. As a result, the properties and microstructure at room temperature are closely related to the solution annealing temperature i.e. higher solution annealing temperatures produces higher ferrite contents [34]. A microstructure of approximately 50:50 percent of ferrite and austenite can be achieved at room temperature by water quenching from the appropriate solution annealing temperature [36]. Nitrogen is typically added as an alloying element to stabilize and accelerate the formation of the austenite phase [43, 44].

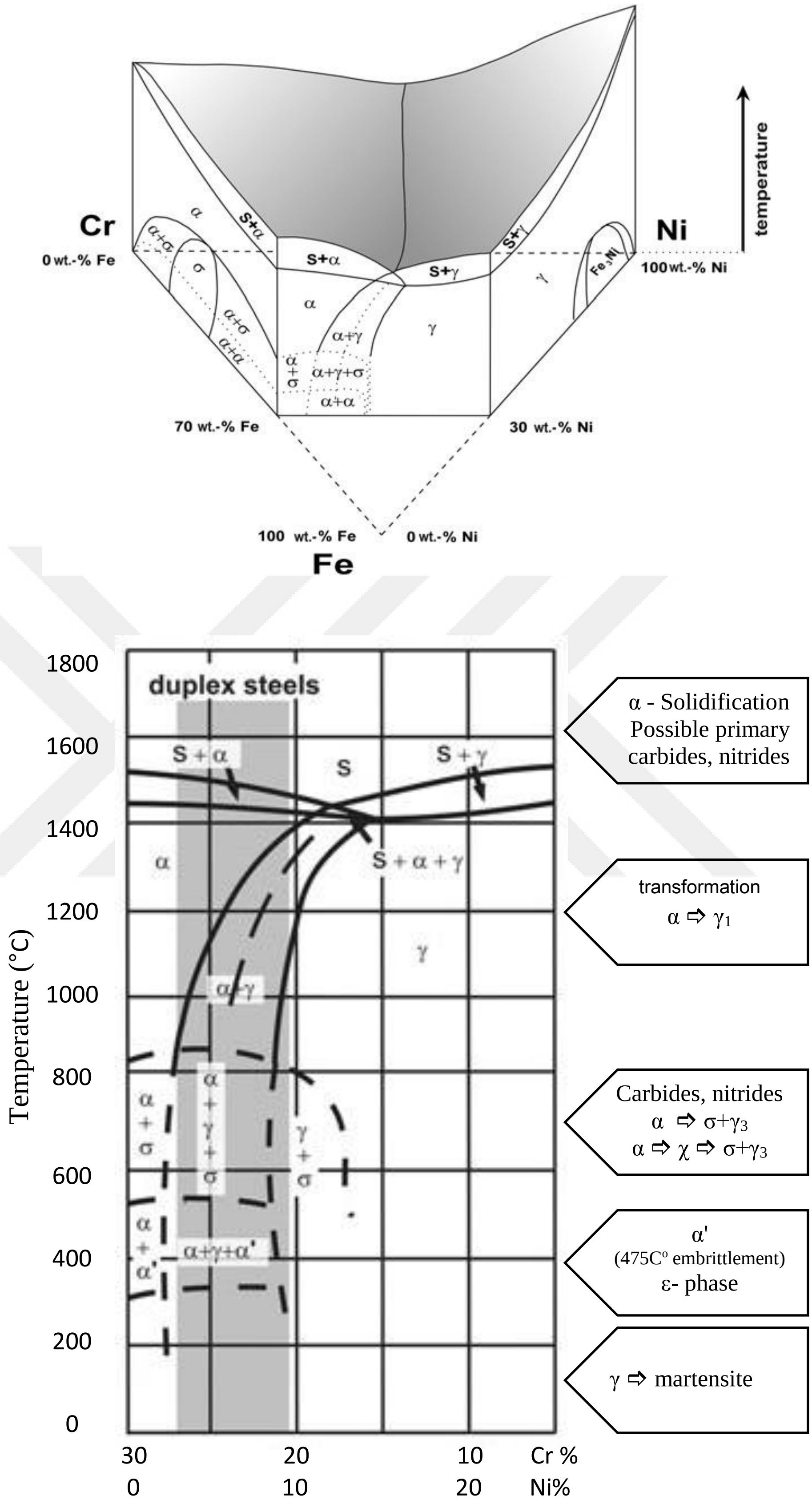


Figure 2.14 Pseudo-phase binary diagram of duplex grades (2205/2507) [44]

### 2.8.2 The Role of Alloying Elements in Duplex Stainless Steels

The interactions between the main alloying elements, especially chromium, molybdenum, nitrogen, and nickel, are very complex. To achieve a stable duplex structure that can be well fabricated, care must be taken to ensure that each of these elements is at the correct level. In addition to the phase balance, a second major concern is the formation of harmful intermetallic phases [36].

Chromium and molybdenum are ferrite stabilizers as they promote the body centered cubic (BCC) crystal structure of iron and they are used to increase the strength, corrosion resistance, hardenability and wear resistance of DSS. Whereas nickel and nitrogen are austenite stabilizers as they promote the transformation of crystal structure from BCC to face centered cubic (FCC) structure which increases the precipitation mechanism of austenite phases and these two alloying elements increase the pitting corrosion resistance, impact toughness and the tensile properties of DSS. To develop the duplex structure, the ferrite formers, chromium and molybdenum should be balanced by the austenite formers, nickel and nitrogen [45].

### 2.8.3 Desired Microstructure

The microstructure of super duplex stainless steels is a ferritic-austenitic structure, and hot-rolled material has elongated grains in the rolling direction (Figure 2.10). The ferrite / austenite ratio will impact the DSS properties. Report 938-C of the American Petroleum Industry (API) states that the ferrite content in DSS is to be within the range of 30-65% . However, the best properties are obtained when the ferrite content is about 50% [35, 46].

### 2.8.4 Precipitation of Secondary Phases

Slow cooling in the critical temperature ranges can result in the formation of various types of intermetallic phases that are detrimental to the mechanical and corrosion properties of SDSS [47]. The amount and the type of alloying elements have a direct influence on the precipitation actions of different phases, as shown in Figure 2.15 [36]. By increasing the Cr and Mo concentrations, the Time-Temperature Transformation (TTT) curves of the precipitation reactions can be shortened, thus increasing the stability area of the sigma phase [47]. Different types of precipitates, which can form in SDSS after thermal aging, are introduced taking into account two temperature ranges:

1- High Temperature Range (550-1000°C) Precipitations
2- Low Temperature Range (250-550°C) Precipitations

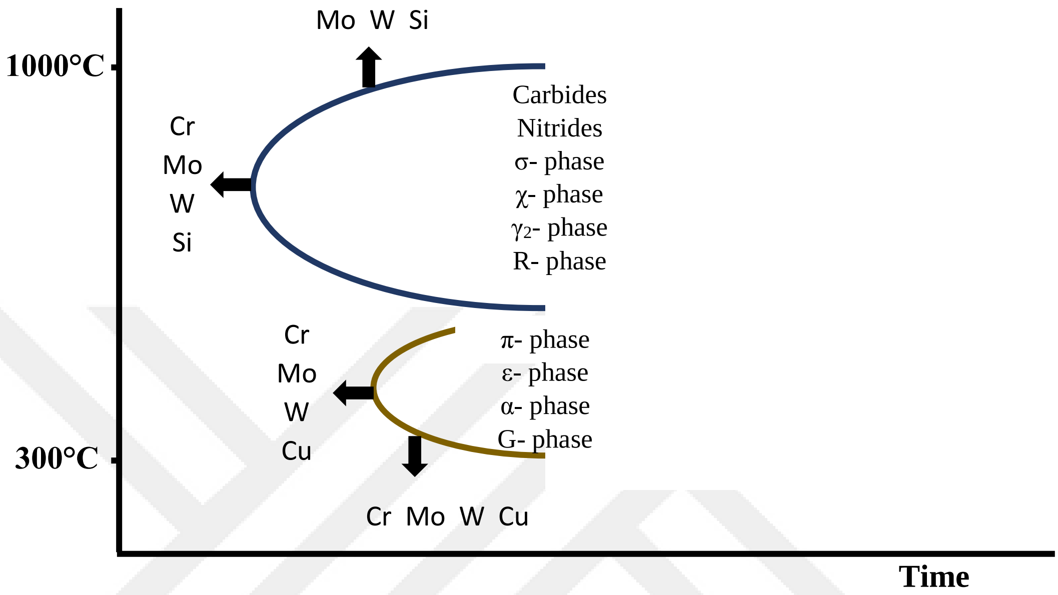


Figure 2.15 Time-temperature precipitation diagram of duplex stainless steels [35]

#### 2.8.4.1 High Temperature Range (550-1000°C) Precipitations

Sigma (σ) phase, which is a Fe-Cr-Mo rich phase with a tetragonal structure is the most well-known deleterious phase precipitating in DSS from the ferrite at temperatures below austenite formation between (600-1000°C) [35]. In addition, because of the eutectoidal formation of the sigma phase, secondary austenite ($\gamma_2$) is present at the ferrite-austenite boundaries. Sigma phase has a powerful embrittlement effect that decreases toughness. Secondary austenite is normally chromium-depleted compared to the primary form, resulting in a localized reduction in resistance to the pitting corrosion [10].

SDSS can precipitate chi (χ) phase, R phase, and chromium nitrides, in addition to sigma phase and secondary austenite. The R phase is an intermetallic compound rich in molybdenum and usually forms between 550-700°C but its practical significance is lower since its nucleation takes longer [47]. Chi (χ) is a cubic intermetallic phase rich of Mo, precipitating between 700°C and 900°C. It precipitates in smaller amounts compared to σ. Chi (χ) nucleation is rapid due to its cubic structure, whereas its growth rate is slow. Chi (χ) is usually considered to be an intermediate phase, replaced at longer aging periods by the sigma phase [35].

Chromium nitride is formed in the temperature range of 700 - 900°C followed by rapid cooling. At this temperature range, nitrogen does not have enough time to diffuse in austenite and has limited amount of austenite formation. As a result, when ferrite formations are supersaturated with nitrogen, chromium nitrides form at the grain boundaries [47]. The chromium nitride precipitation reduces the pitting corrosion resistance due to loss of chromium and nitrogen [38].

#### 2.8.4.2 Low Temperature Range (250-550°C) Precipitations

The most popular transformation that occurs below 500°C is the spinodal decomposition of the ferrite into chromium-rich ferrite (α') and iron-rich ferrite (α) on a very small scale, which also known as the 475°C embrittlement. A subsequent hardening and embrittlement of the ferrite is observed. This explains why most applications are confined to temperatures below 250°C. SDSS grades with 25% Cr are very sensitive to this phenomenon [34, 35].

#### 2.8.4.3 Microstructure and Mechanical Properties of DSS

Mechanical properties of SDSSs are described as a mixture of austenite and ferrite properties. Combination of the toughness of austenite and strength of ferrite make DSS a desirable material, which can be used in a wide variety of applications. Interestingly, due to their finer microstructure, their strength is higher than both austenitic and ferritic stainless steels. The excellent mechanical properties of SDSSs are restricted to temperatures lower than 250°C due to the danger of 475°C embrittlement as discussed previously [34, 35, 36].

## 2.9 Metallurgy of Additively Manufactured SDSS

The superior mechanical properties and pitting corrosion resistance of SDSS are due to the balanced microstructure consisting of austenite and ferrite phases. This microstructure is significantly influenced and altered by heating, and it has been noticed to suffer the loss of corrosion resistance and reduced impact toughness [48].

WAAM is a layer-by-layer additive manufacturing process based on welding technology. In this process the fresh runs reheat the underlying deposited beads. Reheated beads have a distinct microstructure compared to single pass welds. Common observations are the possible precipitation of secondary austenite and deleterious secondary phases [35]. Maintaining a proper austenite / ferrite phase balance while avoiding brittle phase formation is necessary to maintain acceptable toughness and corrosion resistance of the beads [48].

### 2.10 The Property: Fracture Toughness

Although metallic materials are characterized, with some exceptions, by a significant ductility, metallic structures and components may show, under particular conditions, sudden unexpected failures, where plastic strains are limited or absent at all. This phenomenon, which may occur even if stresses acting on structural elements are well below material's yield strength, and is generally correlated to the presence of planar flaws and called brittle failure. Brittle failure phenomena may occur in structures and/or components where safety and cost aspects are of particular significance. Repair operations may be critical or impossible. These considerations underline the importance of defining assessment procedures, in order to check if materials are fit for their intended use in design conditions or a detected flaw in service can be considered acceptable or not [49].

### 2.11 Fracture Mechanics

The aim of fracture mechanics is to establish the limit conditions beyond which the propagation of an unstable flaw occurs (i.e. crack driving forces determining the flaw propagation overtake material's resistance to fracture, see Figure 2.16) [49]. According to fracture behavior of materials, two main branches of fracture mechanics are taken into consideration: Linear Elastic Fracture Mechanics (LEFM) for brittle materials and Elastic-Plastic Fracture Mechanics (EPFM) for ductile materials [50, 51].

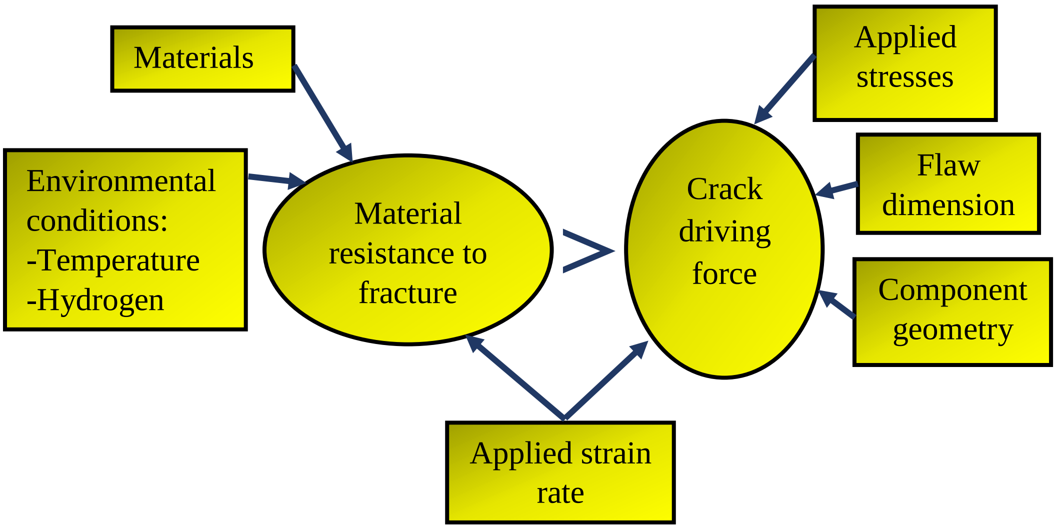


Figure 2.16 Conditions of flaw propagation [49]

### 2.12 Linear Elastic Fracture Mechanics

The basic work for linear elastic fracture mechanics is by Griffith, where he defined a critical stress for failure. As seen in Figure 2.17 a plate with an initial crack length (2a) subjected to tensile stress σ, was used to describe the flaw propagation. At the tip of the crack, the stress is greater than the average stress of σ. Because of this high stress, the material near the tip of the crack will experience large strains and ultimately collapse, allowing the crack to spread ahead [50, 52, 53].

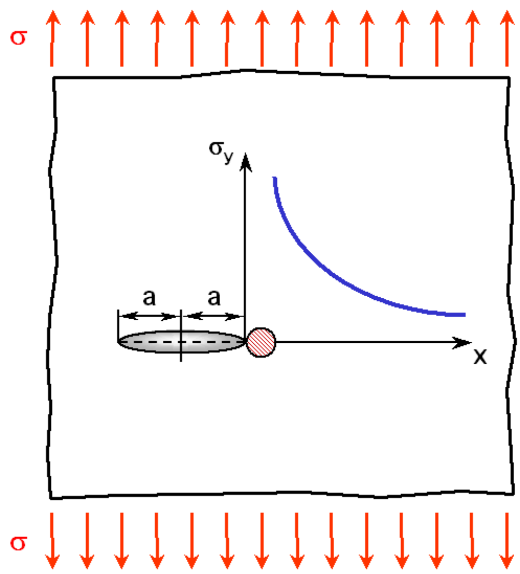


Figure 2.17 Plate with the initial crack [49]

The critical stress $\sigma_c$ required for crack propagation in a brittle material is described by the expression:

$$\sigma_c = \sqrt{\frac{2\gamma_e E}{\pi a}} \tag{2.2}$$

Where:

E is modulus of elasticity

$\gamma_e$ is specific surface energy

a is one half of the length of an internal crack [54]

The modern theory of fracture mechanics started with the analyses carried out by Irwin, where the stress and strain distributions occurring at the tip of a two-dimensional crack can be defined by means of Stress Intensity Factor “K”.

As shown in Figure 2.18, crack propagation may occur according to three different modes, namely the opening mode (mode I), the in-plane shearing mode (mode II), and the out-of-plane shearing mode (mode III) [54]. From an engineering point of view, Mode I is the most important mode as the propagation of crack-like flaws tends to occur perpendicular to the maximum tensile stress direction.

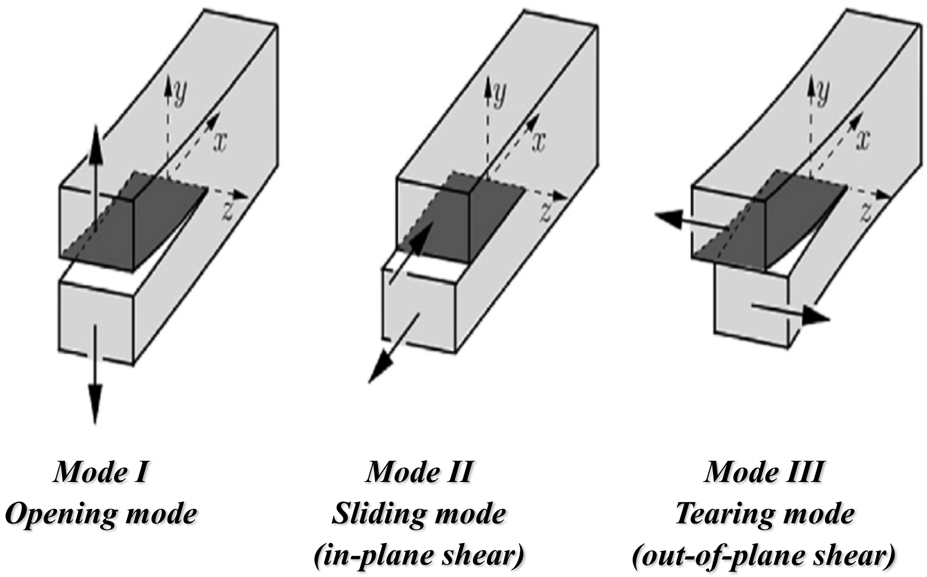


Figure 2.18 The three modes of loading [54]

The mode I stress intensity factor ($K_I$) can be represented by the following general equation:

$$K_I = Y\sigma\sqrt{\pi a} \quad (2.3)$$

The parameter Y depends on:

-Structural component geometry,

-Flaw geometry,

-Type of stress distribution

**σ** represents the *nominal value* characterising the stress distribution;

**a** represents the characteristic flaw dimension [49].

Under an increasing load crack propagation/initiation may initiate when $K_I$ reaches a special critical value $K_{IC}$.

$$K_I = K_{IC}$$

$K_{IC}$ is a real material characteristic called fracture toughness [55].

### 2.13 Elastic Plastic Fracture Mechanics

Linear elastic fracture mechanics (LEFM) lose its legitimacy for ductile materials because the fracture processes at the crack tip are followed by severe plastic deformation in these materials [54]. Therefore, the characterization of the fracture behavior of ductile materials requires Elastic Plastic Fracture Mechanics (EPFM) [51]. The most important concepts in EPFM are crack tip opening displacement (CTOD) and J-integral proposed by Wells (1961) and Rice (1968), respectively [54]. The mechanical behavior near the crack-tip of ductile materials can be defined by both concepts (J and CTOD). Each of them can serve as a measure of the toughness of the material and can therefore be used to determine criteria for fracture [50, 51].

#### 2.13.1 Crack Tip Opening Displacement (CTOD)

For elastic-plastic materials (ductile materials), the crack tip opening displacement (CTOD) is a fracture mechanics parameter describing crack-tip conditions. It is observed that for materials with high toughness, the high degree of plastic deformation give rise to blunt the crack tip before subsequent ductile tearing as shown in Figure 2.19. The CTOD (δ) value can be connected to $K_I$ as follows:

$$\delta = \frac{K_I^2}{m\sigma_{YS}E'} \tag{2.4}$$

where

*m* is a dimensionless constant that is approximately 1.0 for plane stress and 2.0 for plane strain.

E′ is the effective Young's modulus, defined as:

E′=E for plane stress and E′=E/(1-v$^2$) for plane strain

$\sigma_{ys}$ is the 0.2% offset yield stress [51, 54].

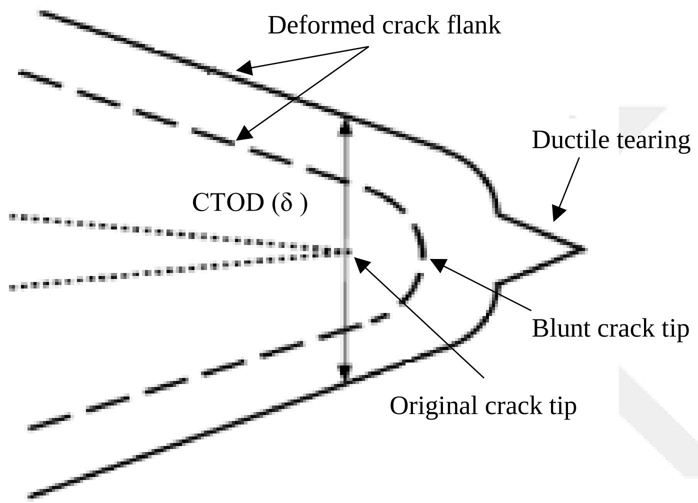


Figure 2.19 Displacement at the original crack tip [54]

### 2.13.2 J- Integral

Plastic deformation takes place in front of the crack tip for common structural steels including DSS with a relatively high toughness. The J-integral can be determined for these materials, which describes the rate of energy release of non-linear elastic materials. This toughness determination method is based on the amount of energy required to initiate and propagate a crack [56]. J reflects the energy "spent" for crack propagation per unit fracture surface under the most general conditions, both when the material behavior is primarily linear elastic and when the size of the plastic zone is large. The following equation is valid for materials with elastic behavior:

$$J = G = \frac{K^2}{E'} \tag{2.5}$$

G=Crack extension force

E′=E for plane stress

E′=E/(1-v$^2$) for plane strain [49]

### 2.14 Crack-Growth Resistance Curves

Many high toughness materials do not show catastrophic failure at a particular value of J or CTOD. Instead, these materials display an increasing R curve, where J and CTOD rise with the progress of cracks. An increasing of R curve is typically correlated with micro voids coalescence. Figure 2.20 demonstrates a standard J resistance curve for a small amount of visible crack growth due to blunting. When J increases, the material at the crack tip fails locally and the crack progresses further. Due to the rising of R curve, the initial crack growth is usually stable but instability may later be encountered [54].

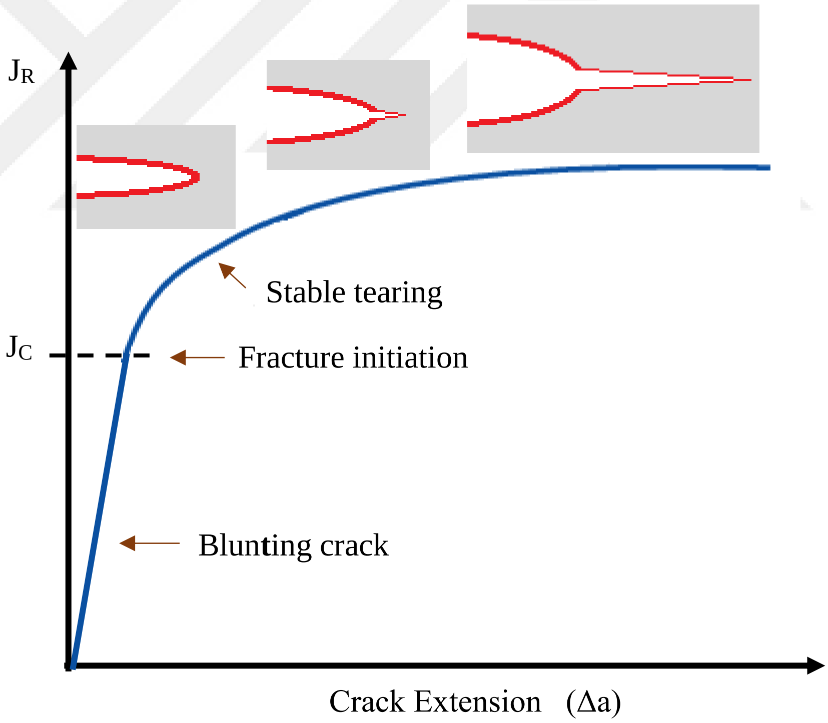


Figure 2.20 Crack-growth resistance, R- curve [54]

### 2.15 Methods of Measuring and Types of Specimen

For fracture toughness testing of a material a lot of specimens are used to analyse characteristic values [55]. Single edge notched bend (SENB) (Figure 2.21-a) and compact tension (CT) (Figure 2.21-b) specimens with a high crack depth are the most frequently used types of specimens [57], and their use is defined in international standards such as ASTM E1820 and BS-7448 [58]. These specimens are subjected to a bending load that results in a high crack-tip constraint condition, which is unrepresentative of constraint at the crack tip in conditions like a surface crack in a pipe [58]. In recent years, the clamped single edge notched tension (SENT) specimens (Figure 2.21-c) have been commonly used [57]. Generally, the lower constraint of the SENT specimen, compared to the SENB specimen, results in higher values of fracture toughness [59, 60].

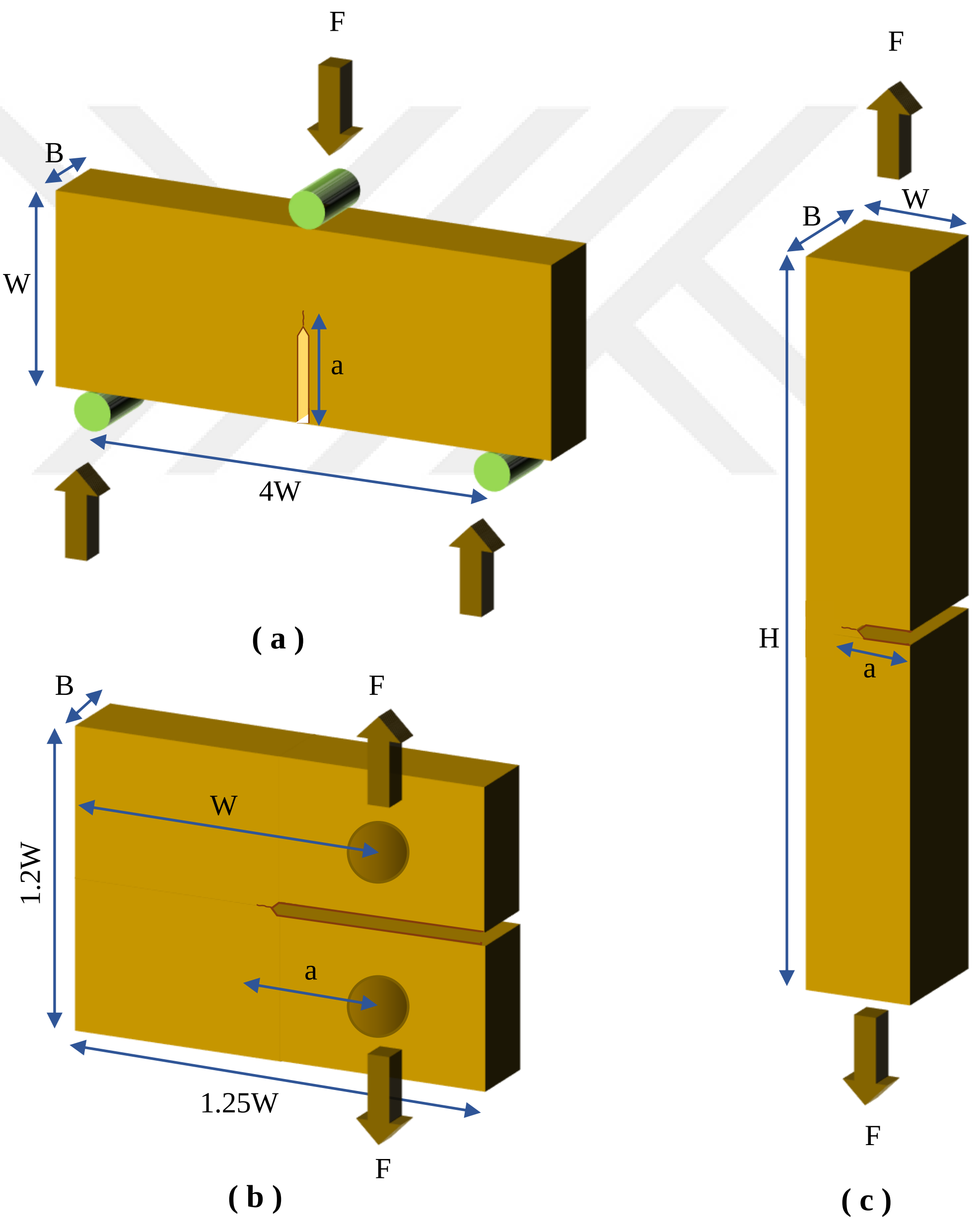


Figure 2.21 Standardized fracture mechanics test specimens: (a) single edge-notched bend, (b) compact specimen, (c) single edge notched tension. [61, 62]

Fracture toughness testing with SENT specimens is now standardized in BS 8571 and SENT specimens can be used for higher and lower temperature testing, different material thicknesses and wide range of engineering applications. SENT test results can be considered for use with fitness-for-service evaluation provided that the structural specification to be tested has lower constraints than the specimen [59].

### 2.16 Fracture of Duplex Stainless Steels

The room temperature fracture behaviour of duplex stainless steels is well established. Compared to other stainless steels the fracture toughness of DSS is very high and this high toughness could be ascribed to the presence of austenite [10, 63]. The ductile austenite retards the cleavage fracturing of ferrite [63, 64]. The grain size together with crystallographic texture of SDSS can also influence the behavior of the fracture. It has been shown that there is a strong rolling texture in specimens which results in highly anisotropic resistance properties [10]. The fracture toughness values are higher in the transverse than in the longitudinal direction with respect to the rolling direction [63].

When a DSS part is additively manufactured using arc welding, the fracture toughness of welded layers and their heat affected zones are generally much lower compared to that of the rolled plate.. Deposited metals have a fine grain size because of their rapid cooling rate. In addition, there can be partial dissolution of austenite grains in the heat affected zone, as well as general matrix ageing. Ductility is therefore limited, and the work hardening rate is much higher than that of the rolled plate.. During additive manufacturing, reheating of welded layers can also nucleate brittle intermetallic phases within the matrix that further promote cleavage fracture. The fracture behavior of welded layers is thus often the critical factor in a product's performance [10].

At sub-zero temperatures, the fracture mechanism for ferrite shifts from ductile to brittle fracture. This phenomenon called the ductile-to-brittle transition. The cause for this change in fracture behavior for the ferrite is the restricted slip and dislocation/twin interactions. The ductile-to-brittle transition temperature (DBTT) of SDSS depends on the chemical content, microstructure, existence of detrimental phases and precipitations [10, 64, 65]. In conclusion, although the fracture toughness of duplex stainless steels is generally well studied, fracture behavior of additive manufactured duplex stainless steels (especially at low temperatures) needs further studies to be conducted [10].

## CHAPTER 3

## NUMERICAL SIMULATION STUDY

### 3.1 General

Wire arc additive manufacturing is a welding based process and can be abbreviated it as (WAAM). The process is commonly used in industrial applications due to its high efficiency, durability and low cost compared to some other processes. One of the challenges faced by engineers and technicians in this process is the selection of the best welding parameters to achieve high quality at low cost. By strategic planning of experiments design, effective statistical models can be developed to solve these significant problems. In this work, response surface method has been used to build statistical models to study the effect of WAAM process variables (welding voltage, current and welding speed) on longitudinal and transversal distortion of product. The statistical models would be helpful in setting process parameters at optimum values to achieve a low displacement resulted from longitudinal and transversal distortion. The plan of study is shown in Figure 3.1. Instead of doing real WAAM process, which leads to additional costs caused by losing expensive material, numerical simulation was used to simulate the WAAM process and predict the longitudinal and transversal distortion. Design-Expert version 7.1.3 software [66] was used to obtain the statistical models and optimization. For the simulation, a commercial software package, COMSOL Multiphysics 5.5 [67] has been used to perform the thermal and mechanical tests.

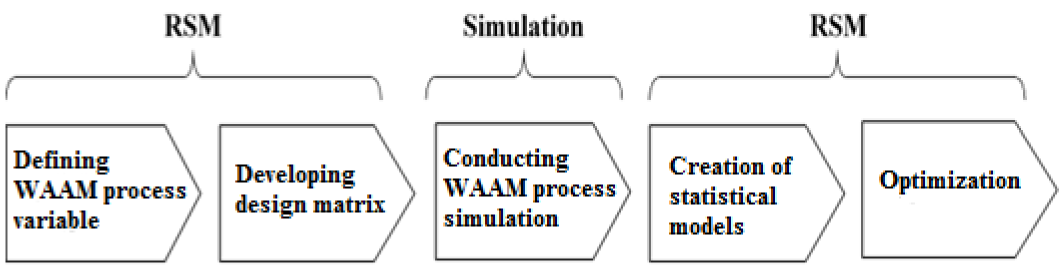


Figure 3.1. The plan of study

## 3.2 Wire Arc Additive Manufacturing Process Variables

According to the previous studies that covered CMT welding based AM of SDSS, the upper and lower values of welding parameters are decided as given in Table 3.1. [15, 17, 18, 19]

Table 3.1 Control variables

| | Lower | Upper |
|---|---|---|
| Current I (A) | 140 | 220 |
| Voltage U (V) | 15 | 25 |
| Speed S (mm/s) | 4 | 10 |

The response surface design constructed from three sets of points, first set based on factorial design which consist of 2k experiments and coded as (±1, ±1, ±1). Second set, center points, coded as (0, 0, 0). Third set, star points, consist of 2k experiments and located at a specified distance α from the center point and coded as (±α,0, 0), (0, ±α, , 0 ), (0, 0, ±α). The value of α can be calculated by the equation (3.1). [68]

$$\alpha = 2^{k/4} \tag{3.1}$$

k = Number of process parameters.

For k=3 ⇨ α = ± 1.682

All sets are shown diagrammatically in Figure 3.2 for k = 3

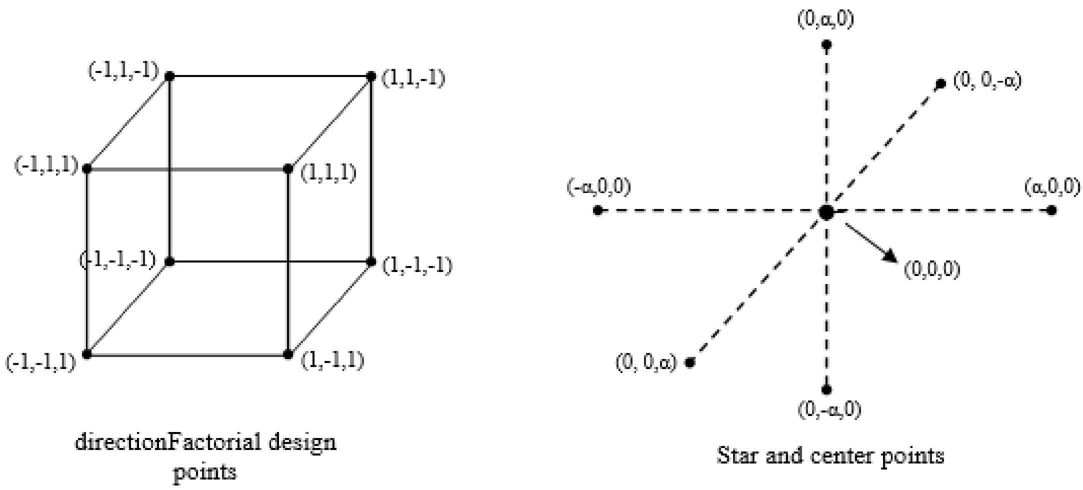


Figure 3.2 Response surface design for k=3 variables

Five levels for each WAAM process variables have been defined based on the response surface method. The five levels were coded as (-α , -1 , 0 , 1 ,  α). The original values (X) of the variable at α can be calculated by the equation (3.2). [68]

$$X = (((\pm\alpha+1)/2) \times (X_U - X_L)) + X_L \tag{3.2}$$

Where:

X : the original value of the variable at α.

$X_U$ : the upper variable value.

$X_L$ : the lower variable value.

The selected WAAM process variables with their limits and codes are given in Table 3.2

Table 3.2 WAAM process variables with their limits

| Parameter | Units | Notation | Factor levels | | | | |
|---|---|---|---|---|---|---|---|
| Coded value | | | -1.682 | -1 | 0 | 1 | 1.682 |
| Current | (A) | I | 112.72 | 140 | 180 | 220 | 247.28 |
| voltage | (V) | U | 11.6 | 15 | 20 | 25 | 28.41 |
| Speed | (mm/s) | S | 2 | 4 | 7 | 10 | 12 |

### 3.3 Response Surface Design Matrix

In factorial design, experiments are carried out on all possible combinations of parameter levels, and these combinations form a design matrix when written in the form of a table. The total number of the experimental runs (N), based on full factorial central rotatable design, is given by the equation (3.3): [69]

$$N=2^k+2k+n_o \tag{3.3}$$

Where $n_o$ refers to the number of the center point.

In the present work, k = 3 which leads to α = 1.682 (formula 3.1*)*. There are 8 corner points, 6 star points and 6 runs for the center point, yielding a total number of twenty experimental runs, N = 20 (formula 3.3). The selected design matrix is shown in Table 3.3 .

Table 3.3 Established design matrix

| Experiment No | Current I (A) | Voltage U (V) | Speed S (mm/s) |
|---|---|---|---|
| 1 | 140 | 15 | 4 |
| 2 | 220 | 15 | 4 |
| 3 | 140 | 25 | 4 |
| 4 | 220 | 25 | 4 |
| 5 | 140 | 15 | 10 |
| 6 | 220 | 15 | 10 |
| 7 | 140 | 25 | 10 |
| 8 | 220 | 25 | 10 |
| 9 | 112.72 | 20 | 7 |
| 10 | 247.28 | 20 | 7 |
| 11 | 180 | 11.6 | 7 |
| 12 | 180 | 28.41 | 7 |
| 13 | 180 | 20 | 2 |
| 14 | 180 | 20 | 12 |
| 15 | 180 | 20 | 7 |
| 16 | 180 | 20 | 7 |
| 17 | 180 | 20 | 7 |
| 18 | 180 | 20 | 7 |
| 19 | 180 | 20 | 7 |
| 20 | 180 | 20 | 7 |

### 3.4 Numerical Modelling and Simulation of WAAM Process

In particular, the selection of the optimum process parameters in this study is based on the evolution of the longitudinal and transversal distortion simulating the welding of super duplex stainless steel Grade (2507), the process simulations are designed in the form of single layer and 3 runs using COMSOL Multiphysics software. The process parameters are selected according design matrix given in Table 3.3 and material properties are given in Table 3.4. [36]

Table 3.4 Super duplex stainless steel properties [36]

| Property | Value | Unit |
|---|---|---|
| Thermal conductivity | 20 | W/(m.K) |
| Heat capacity at constant pressure | 487 | J/(kg.K) |
| Poisson's ratio | 0.3 | -- |
| Young's modulus | $200 \times 10^9$ | Pa |
| Density | 7750 | $kg/m^3$ |
| Coefficient of thermal expansion | $14 \times 10^{-6}$ | 1/K |

### 3.5 Numerical Model Description

Figure 3.3 shows the schematic diagram and geometrical size of the computational domain considered. Points T1, T2 and T3 were selected to estimate the temperature. The distance between each point was 2 mm. Points D1 and D2, with a distance of 50 mm in between, were selected to estimate the longitudinal and transversal distortion.

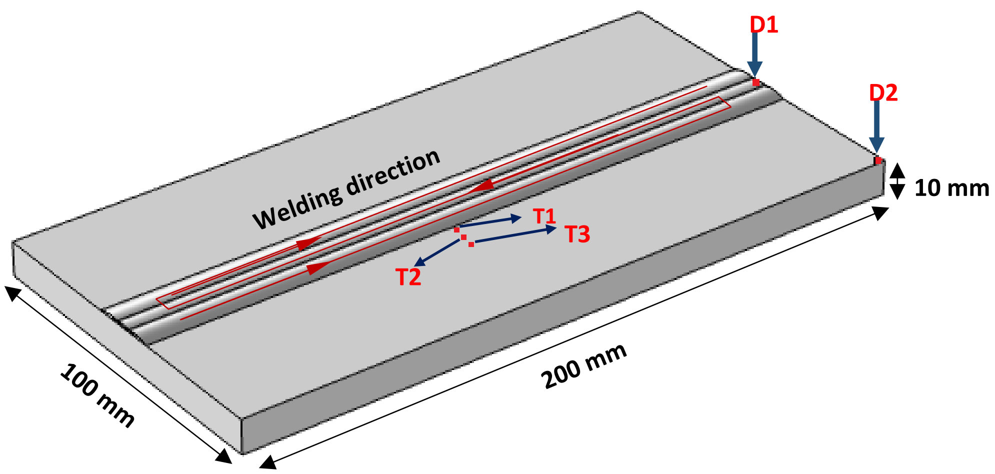


Figure 3.3 Schematic diagram and geometrical size of the computational domain

### 3.6 Numerical Model Assumptions

- Heat flux is deemed at top surface.
- The arc heat flux is defined by the Gaussian distribution.
- The established model does not consider the molten pool's flow but takes into account the simple transfer of heat.

### 3.7 Governing Equations and Boundary Conditions

For the accuracy of the finite element results, the accurate modeling of the heat source is of most significance since it determines the heat input from the welding process and the resultant distortions. A Gaussian distribution can approximate the heat source energy, and the heat flux (q) on the top surface is given by the following expression [2]:

$$q = \frac{2Q}{\pi R_S^2} exp\left(-\frac{2R^2}{R_S^2}\right) \tag{3.4}$$

$$Q = \eta VI \tag{3.5}$$

where Q is the arc power of the heat source, Rs is radius of heat source, R is distance from local point and $\eta = 0.8$.

Equations (3.6) and (3.7) [2], were used to calculate the boundary conditions of cooling between the workpiece and the environment through convection and radiation, respectively.

$$q_c = h(T - T_0) \tag{3.6}$$

$$q_r = \varepsilon \sigma (T^4 - T_0^4) \tag{3.7}$$

where $\varepsilon = 0.6$ is the emissivity of SDSS and h (10 $W/m^2.K$ ) is the natural convective heat transfer coefficient. [70, 71]

### 3.8 Model Validation

To demonstrate the efficacy of the numerical model, an experimental validation is provided by comparing the actual temperature of a WAAM with the simulated ones. The model was validated using data obtained from two published work and data obtained from laboratory works as described below:

**Case 1**

Vahid et al. [18] studied the wire arc additive manufacturing of a duplex stainless steel in terms of thermal cycle analysis and microstructure characterization. A voltage of 24.5 V, a current of 147 A, and a welding speed of 6.5 mm/s were used. The temperature was 1043$^{o}$C at 3.75 mm away from the fusion line of the first pass.

**Case 2**

Carlos et al. [72] studied the welding effects on the duplex stainless steel microstructure by carried bead-on-plate welding. A voltage of 25 V, a current of 180 A, and a welding speed of 6 mm/s were used. The temperature was 1250$^{o}$C at 4 mm away from the fusion line of the first pass.

**Case 3**

Laboratory work has been done by carried bead-on-plate using a voltage of 20 V, a current of 250 A, and a welding speed of 7 mm/s. An indication of the temperature of the deposited metal was obtained by measuring the temperature of the center of the weld pool by inserting a thermocouple into the weld pool behind the arc during depositing. Type K-chromel thermocouples, which are the most common sensor calibration type, are Ni based and exhibit good corrosion resistance. Their melting point is 1370$^{o}$C and they are reliable and accurate at temperatures up to 1260$^{o}$C. During the measurements, the thermocouple material was protected with a ceramic protection tube. Cooling curves obtained by thermocouple reading and temperature data acquisition during the welding processes are represented in Figure 3.4.

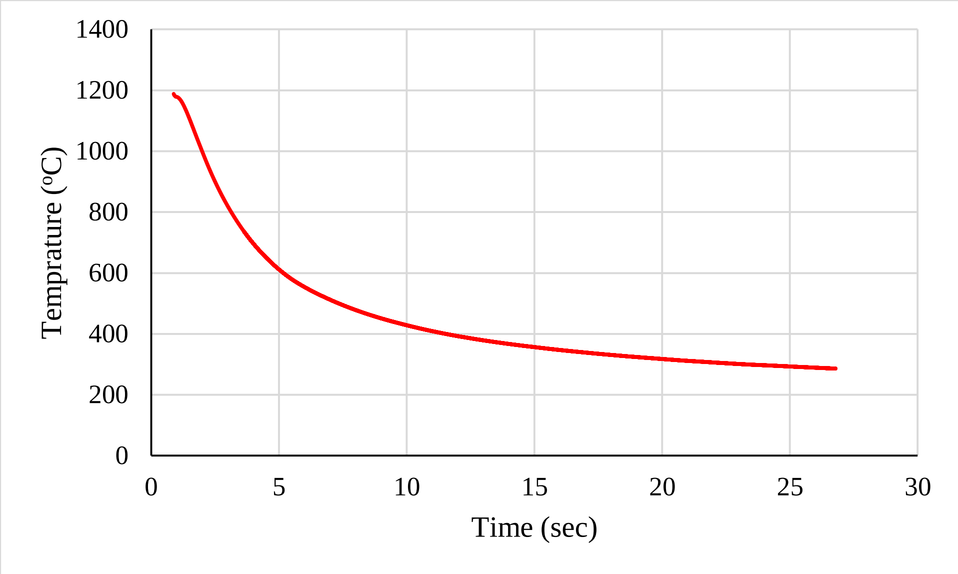


Figure 3.4 Cooling curves recorded in the middle of weld pools

The simulation was executed using the process parameters of case 1, case 2 and case 3 at point T3, 4 mm from the fusion line.

Figure 3.5, Figure 3.6 and Figure 3.7 illustrate the result of simulation for case 1, case 2 and case 3 respectively.

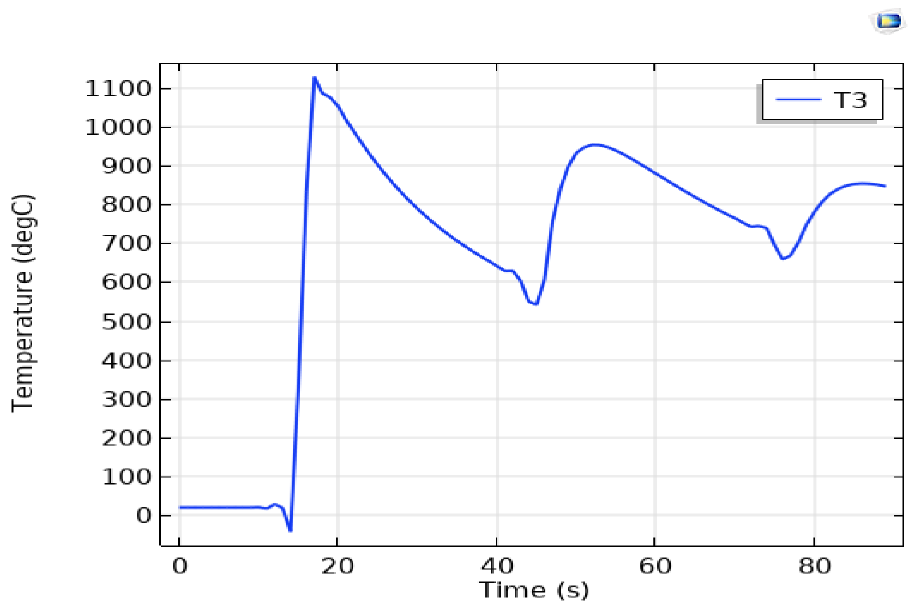


Figure 3.5 Heat distribution of case 1

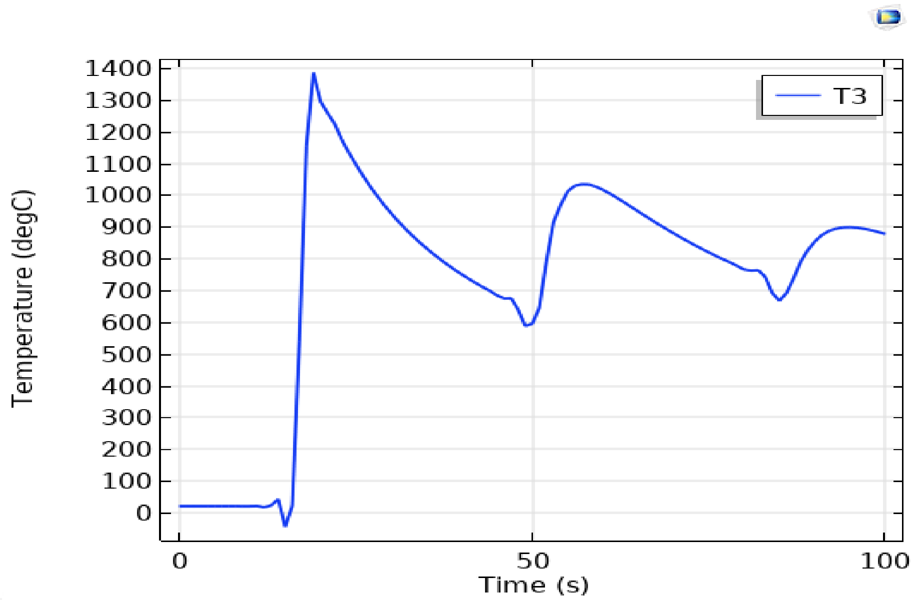


Figure 3.6 Heat distribution of case 2

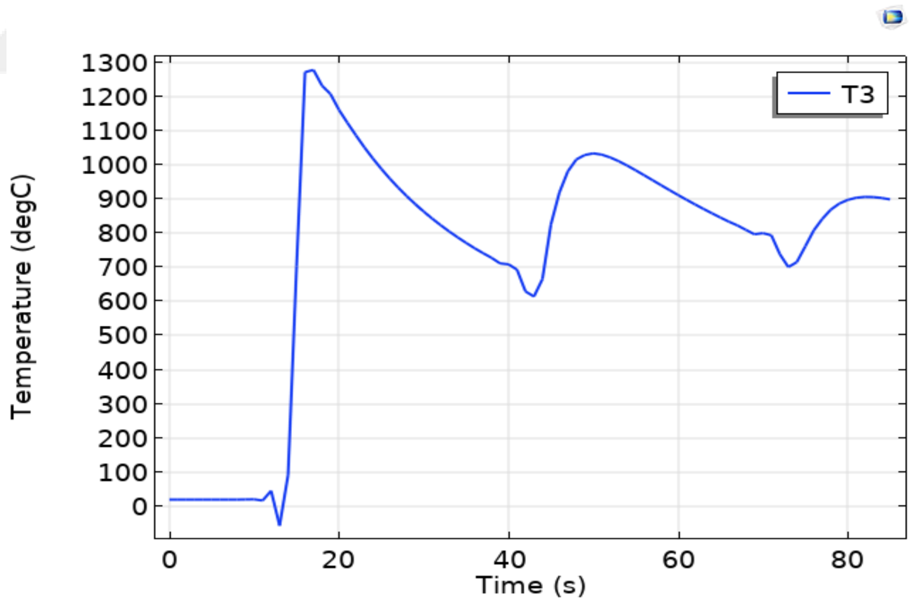


Figure 3.7 Heat distribution of case 3

The results obtained from simulation were recorded and compared with the actual results of experiments as shown in Table 3.5.

Table 3.5 Actual and simulation results of temperature

| Case No. | Temperature ($^oC$) | | Error |
|---|---|---|---|
| | Experiment | Simulation | |
| Case 1 | 1043 | 1128 | 8.2 % |
| Case 2 | 1250 | 1385 | 10.8 % |
| Case 3 | 1188 | 1277 | 7.5 % |

When the temperatures obtained from the simulations are compared to the results of actual experimental temperature measurements; the relative percentage errors are up to 8.2 % for case1, and 10.8 % for case 2, and finally 7.5% for case 3. Considering the heat transfer assumptions in the model, and considering the accuracy of thermocouple readings and the delay in thermocouple response times, these differences are small and expected so that it is concluded that the simulation of the model using COMSOL Multiphysics holds.

### 3.9 Simulation Results

The results obtained from simulation were recorded and surmised in figures from Figure 3.8 to Figure 3.22. Since the values of distortion and temperature were equal for the last 6 experiments only one of them is presented. The heat distributions were presented in part (a) of the figures while the displacements resulting from longitudinal and transversal distortion were shown in part (b) of the figures for the 15 experiments in design matrix, recorded in Table 3.3. The results displayed in (3D) for experiments were shown in part (c) of the figures.

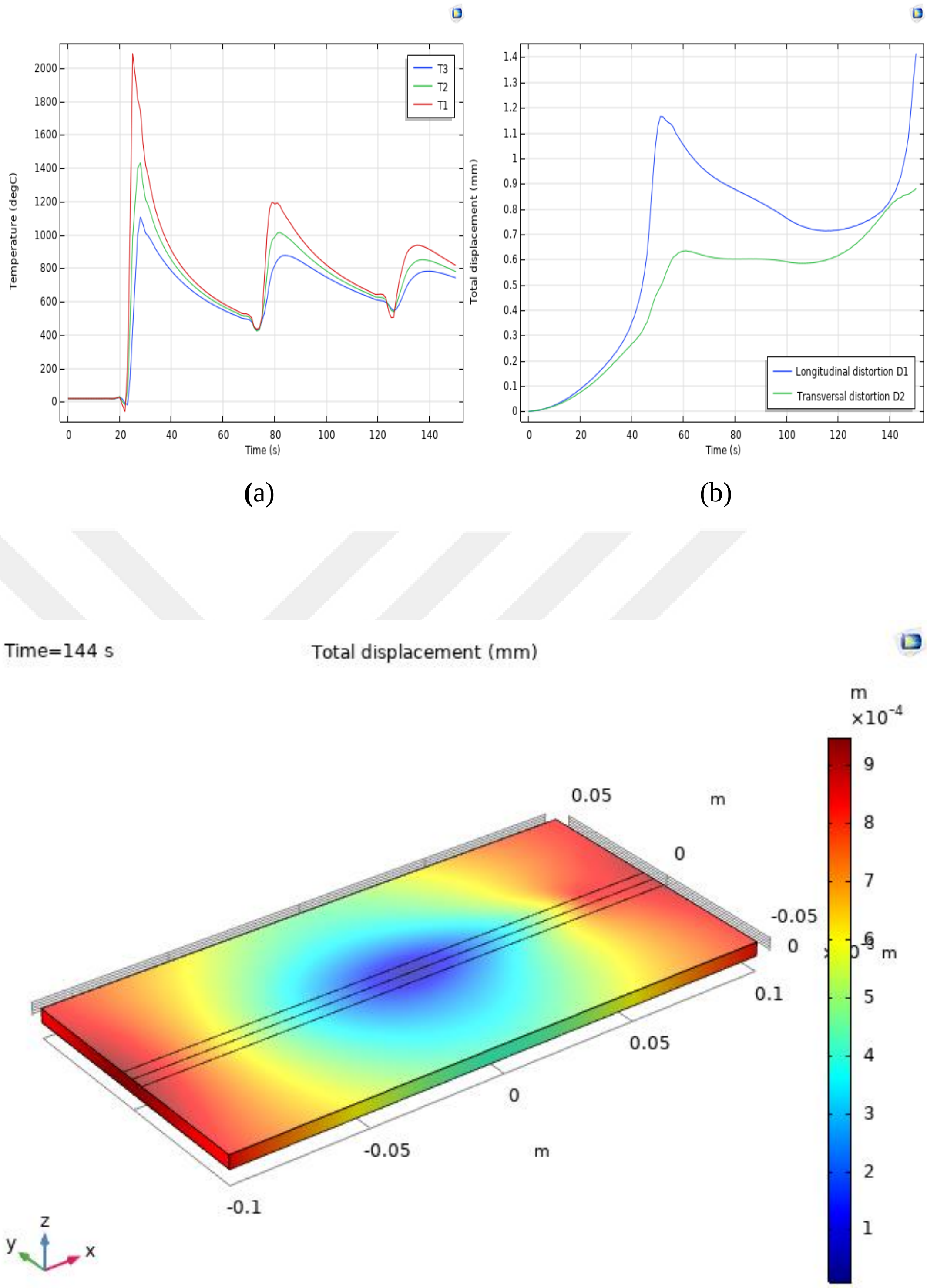


**(c)**

Figure 3.8 Simulation result of experiment (1). a) Thermal cycle, b) Displacements, c) Total displacement results displayed by FEM simulations

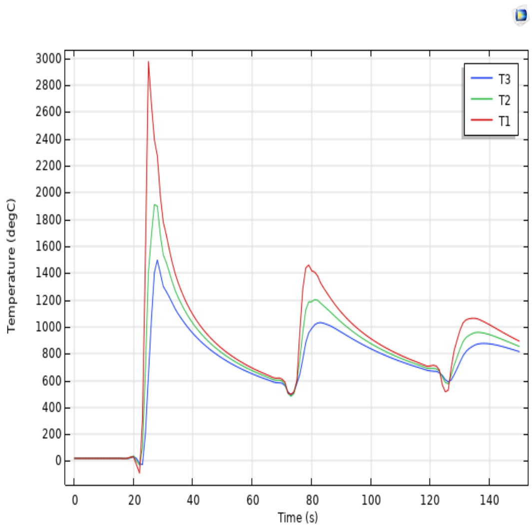


(a)

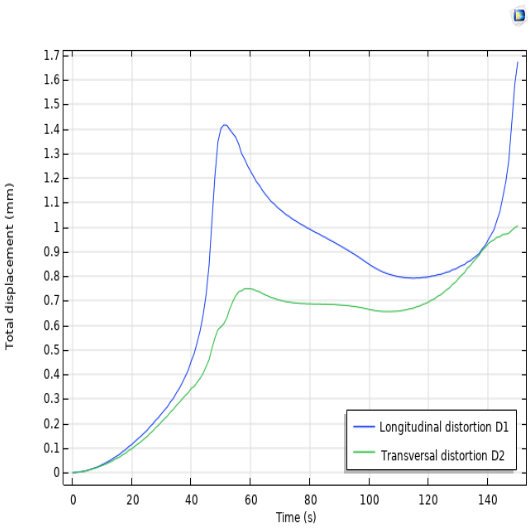


(b)

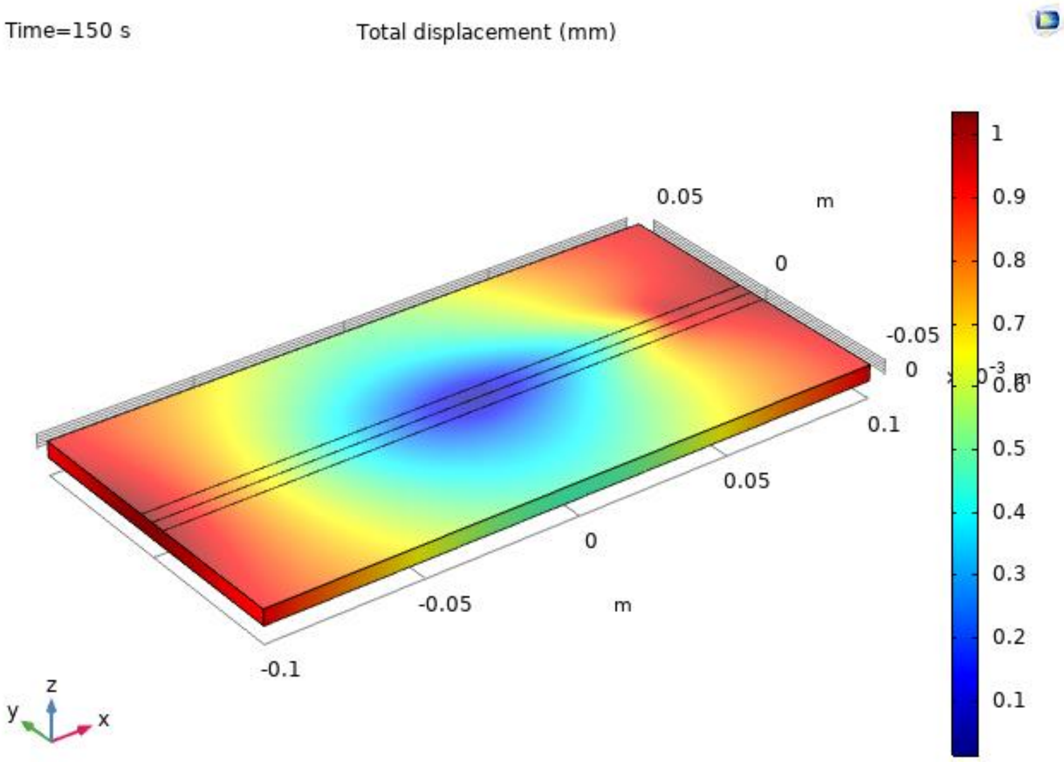


(c)

Figure 3.9 Simulation result of experiment (2). (a) Thermal cycle (b) Displacements (c) Total displacement results displayed by FEM simulations

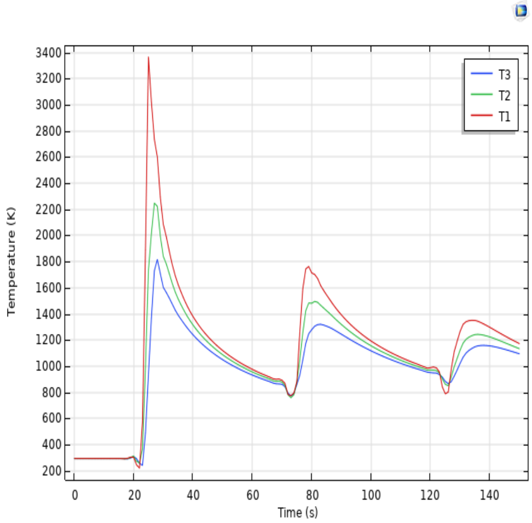


**(**a)

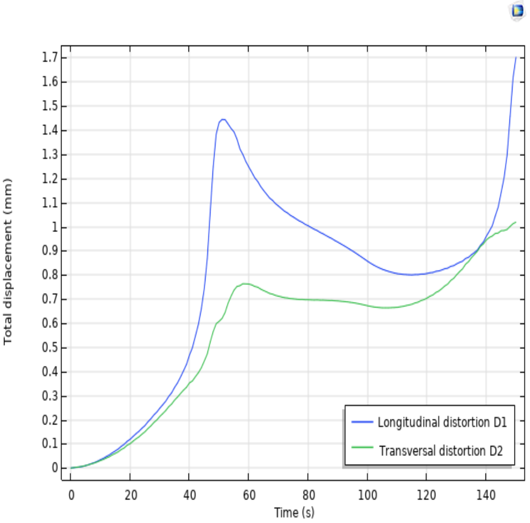


(b)

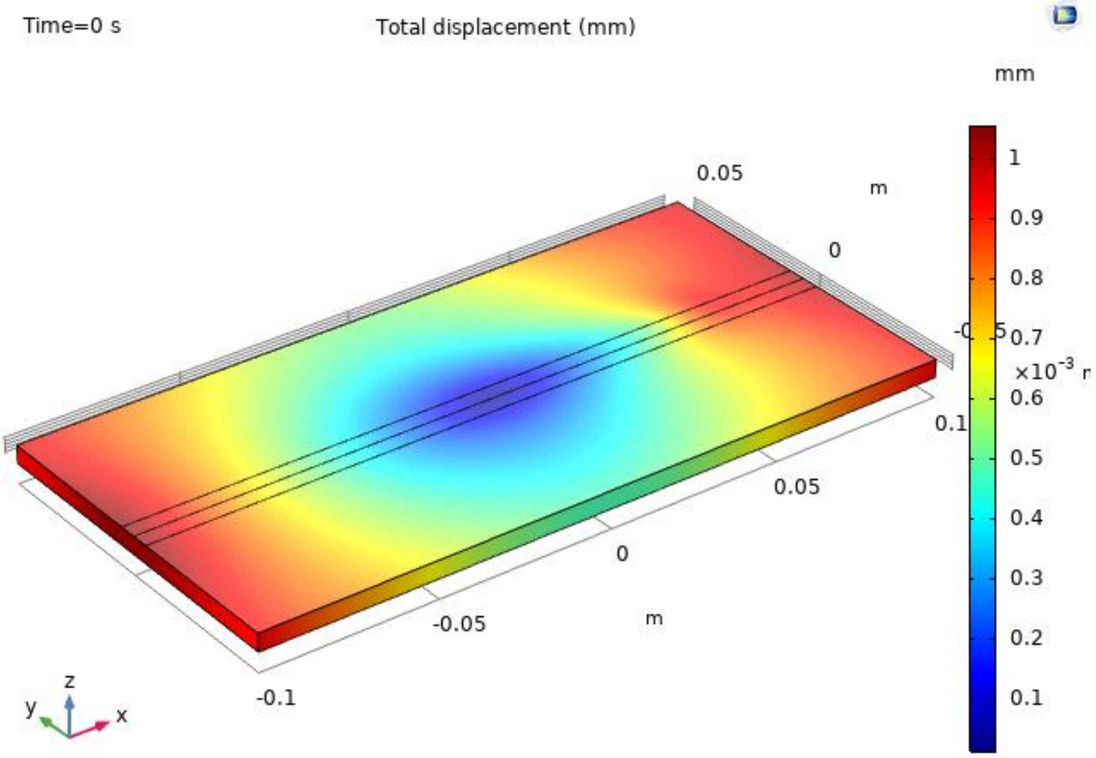


(c)

Figure 3.10 Simulation result of experiment (3). (a) Thermal cycle (b) Displacements (c) Total displacement results displayed by FEM simulations

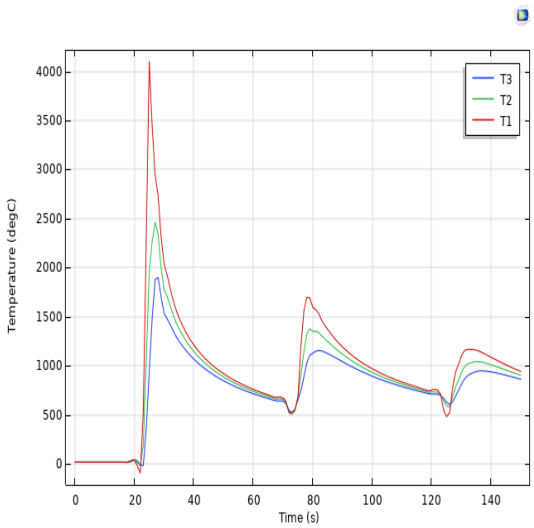


(a)

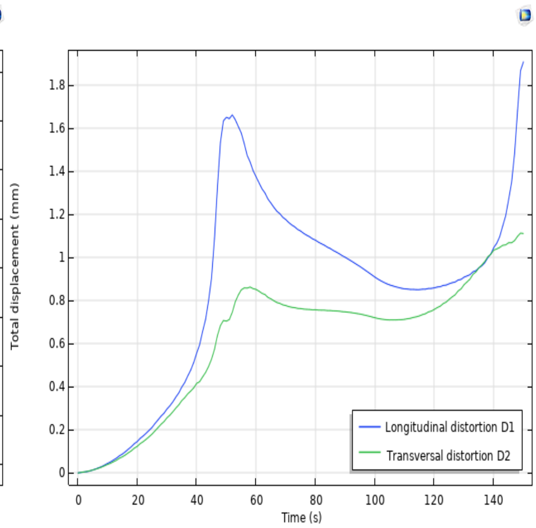


(b)

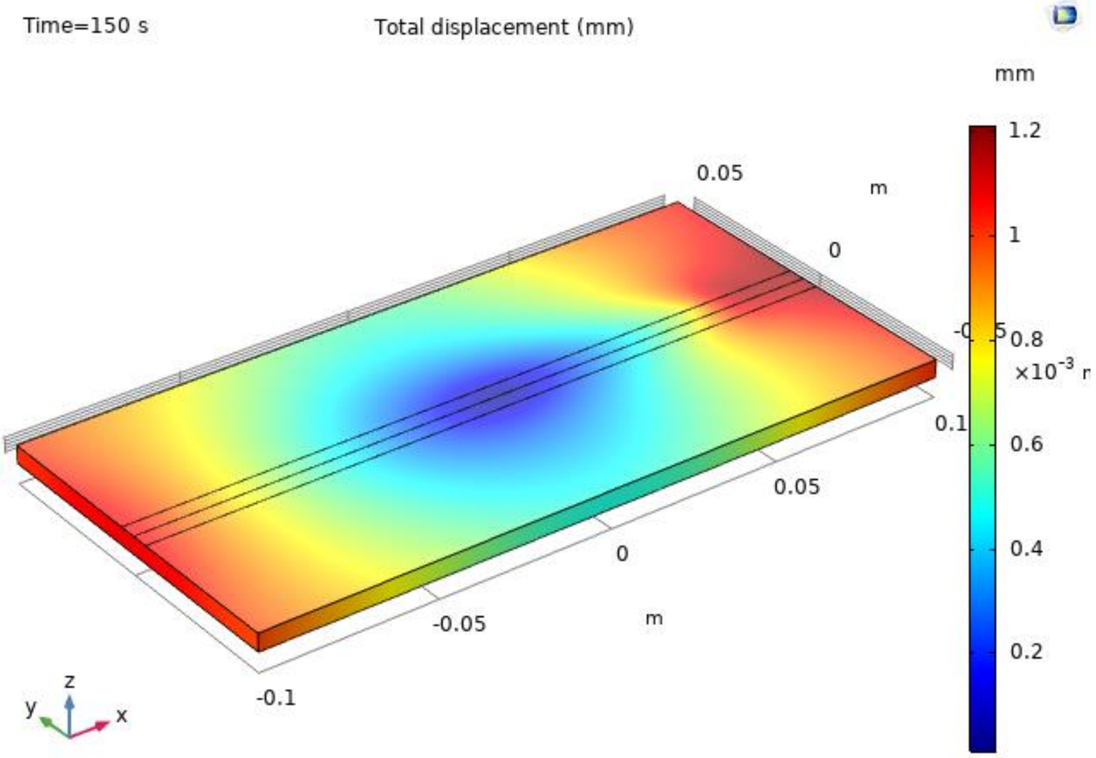


(c)

Figure 3.11 Simulation result of experiment (4). (a) Thermal cycle (b) Displacements (c) Total displacement results displayed by FEM simulations

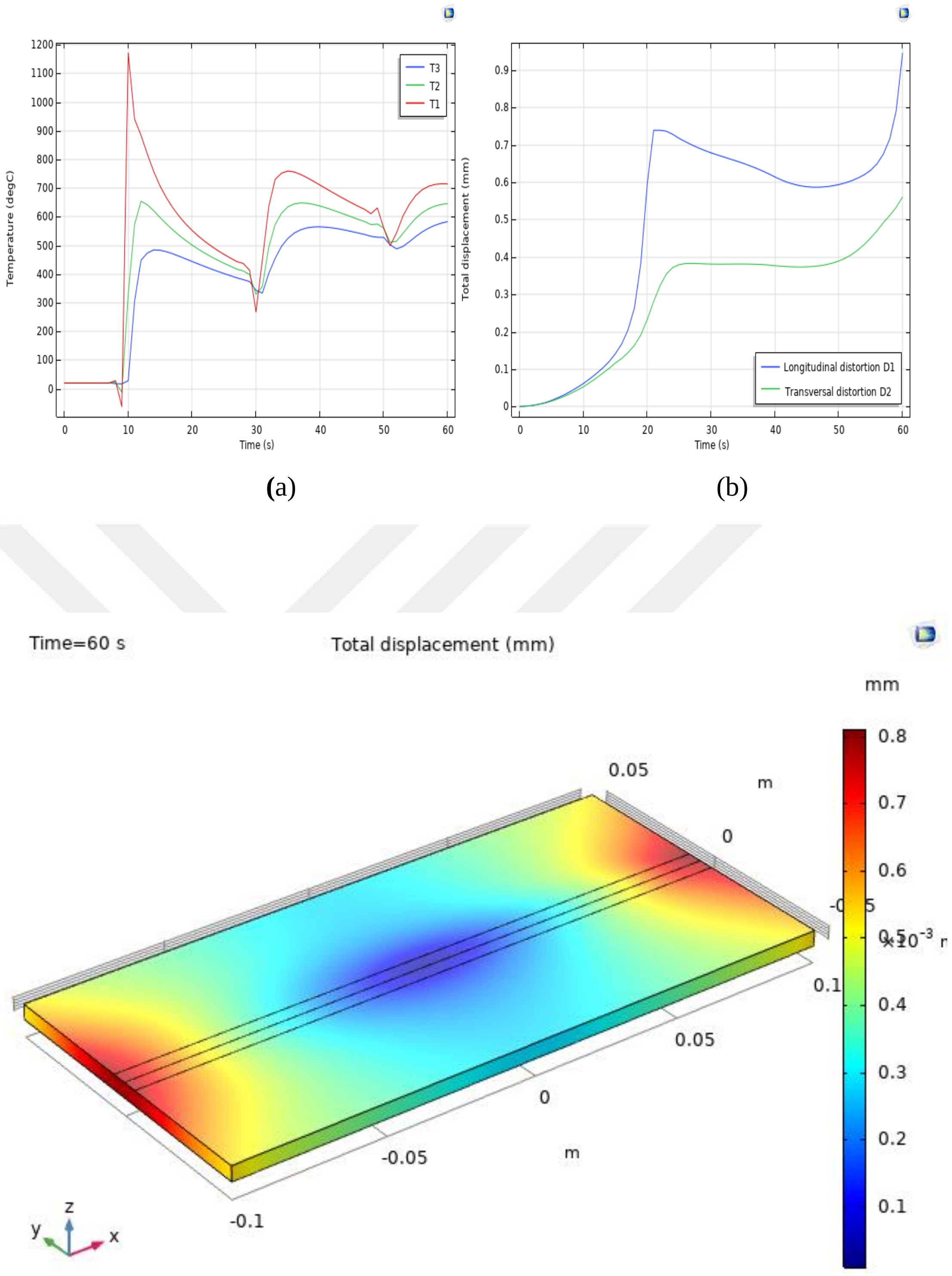


(c)

Figure 3.12 Simulation result of experiment (5). (a) Thermal cycle (b) Displacements (c) Total displacement results displayed by FEM simulations

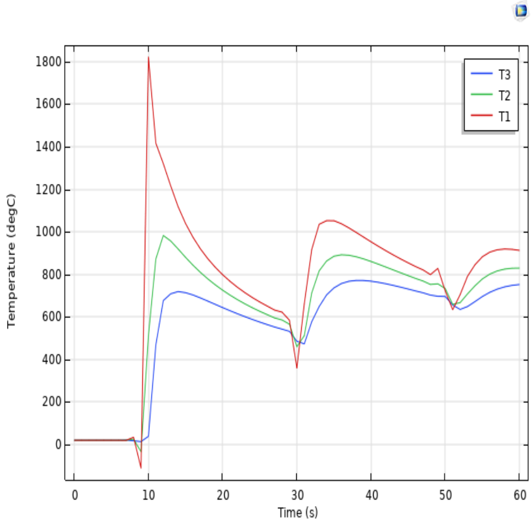


(a)

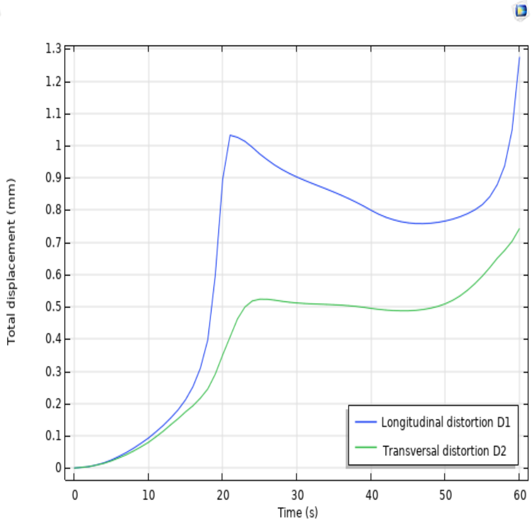


(b)

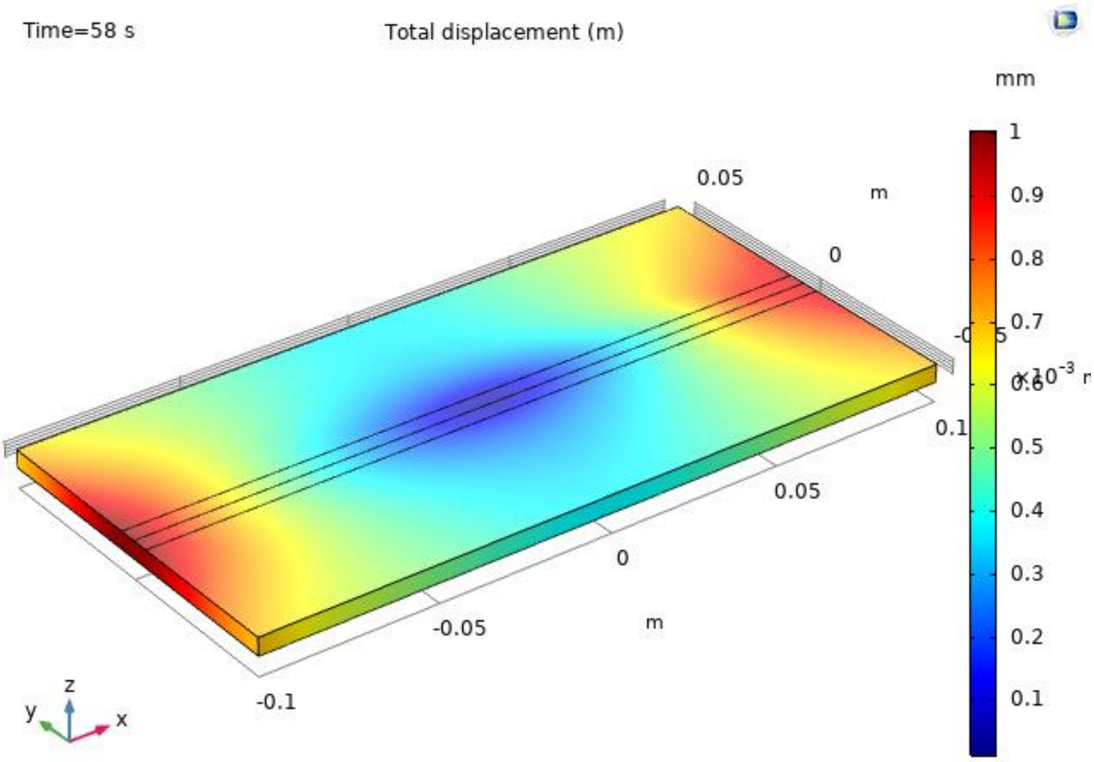


(c)

Figure 3.13 Simulation result of experiment (6). (a) Thermal cycle (b) Displacements (c) Total displacement results displayed by FEM simulations

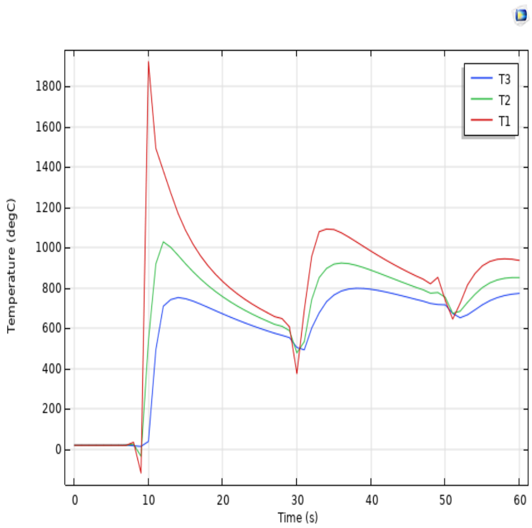


(a)

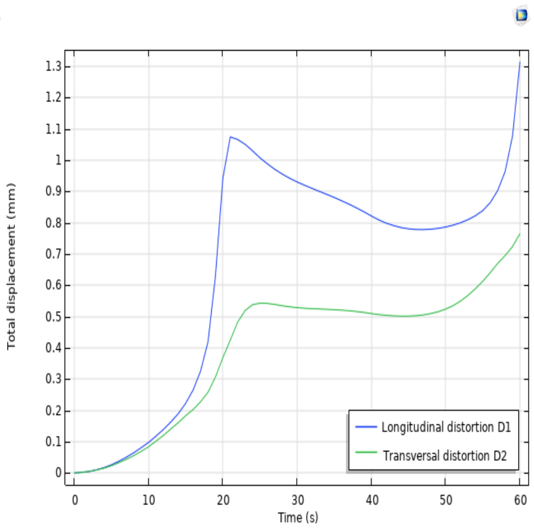


(b)

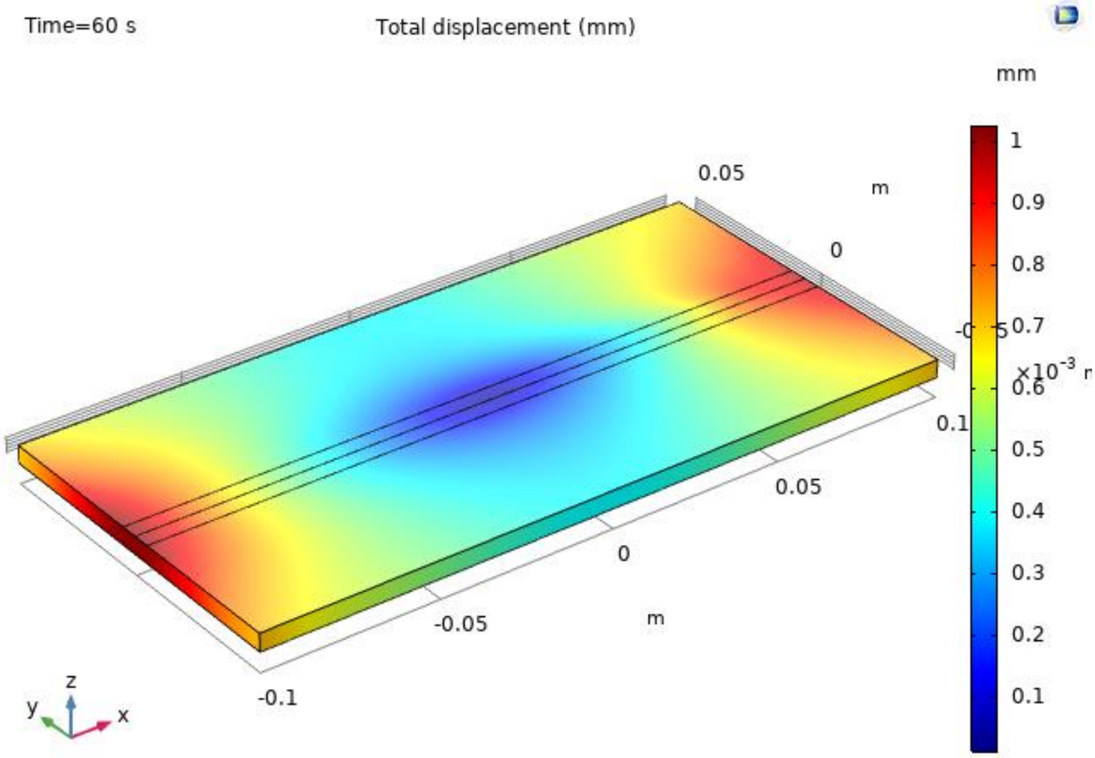


(c)

Figure 3.14 Simulation result of experiment (7). (a) Thermal cycle (b) Displacements (c) Total displacement results displayed by FEM simulations

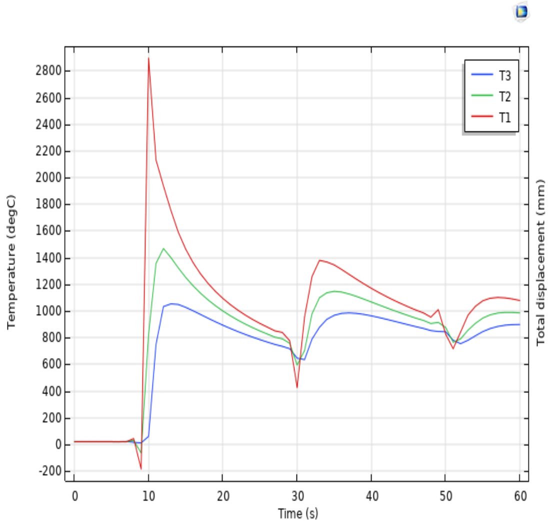


(a)

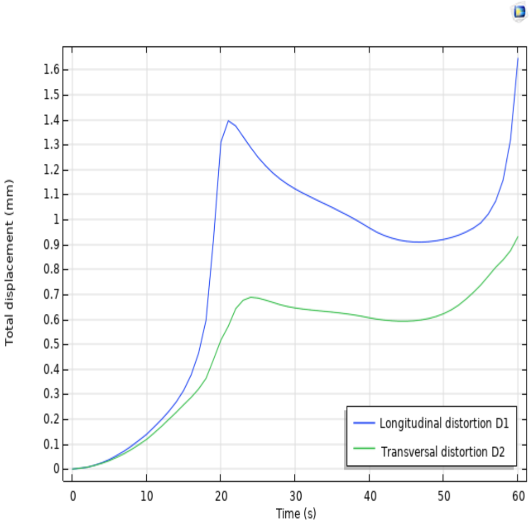


(b)

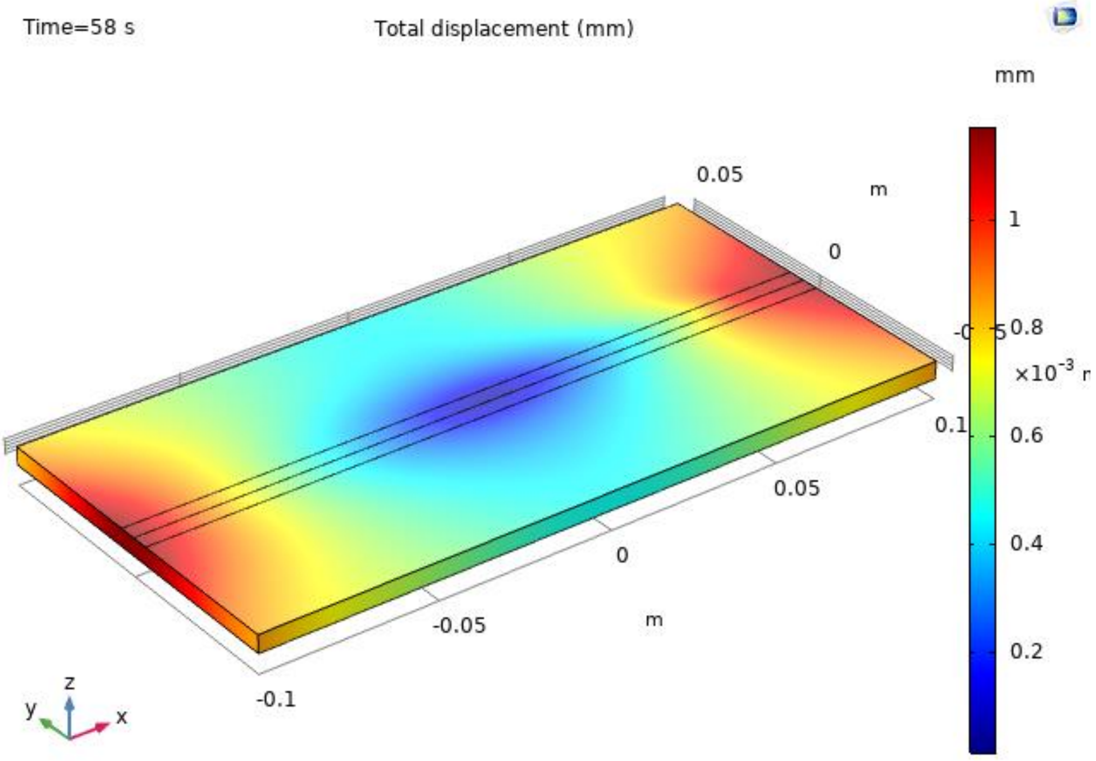


(c)

Figure 3.15 Simulation result of experiment (8). (a) Thermal cycle (b) Displacements (c) Total displacement results displayed by FEM simulations

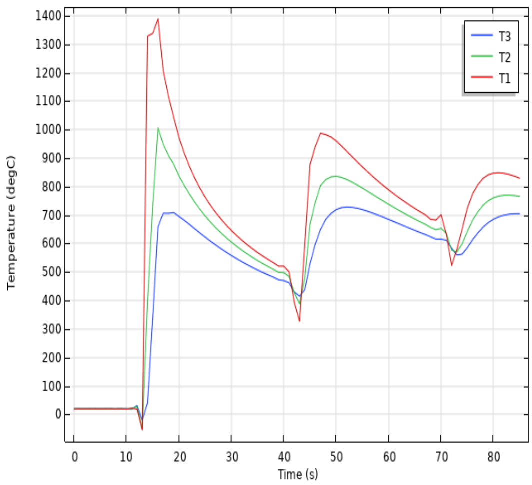


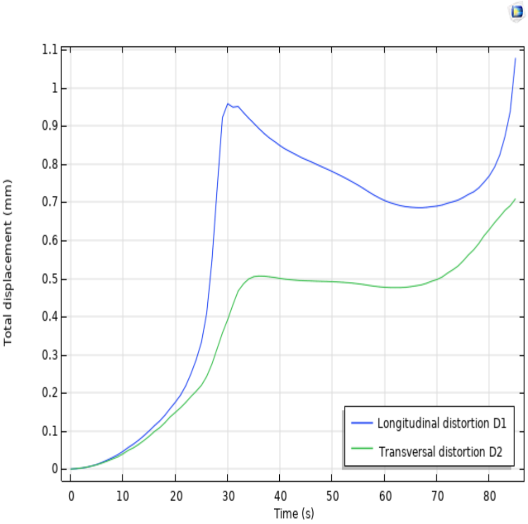


(a) (b)

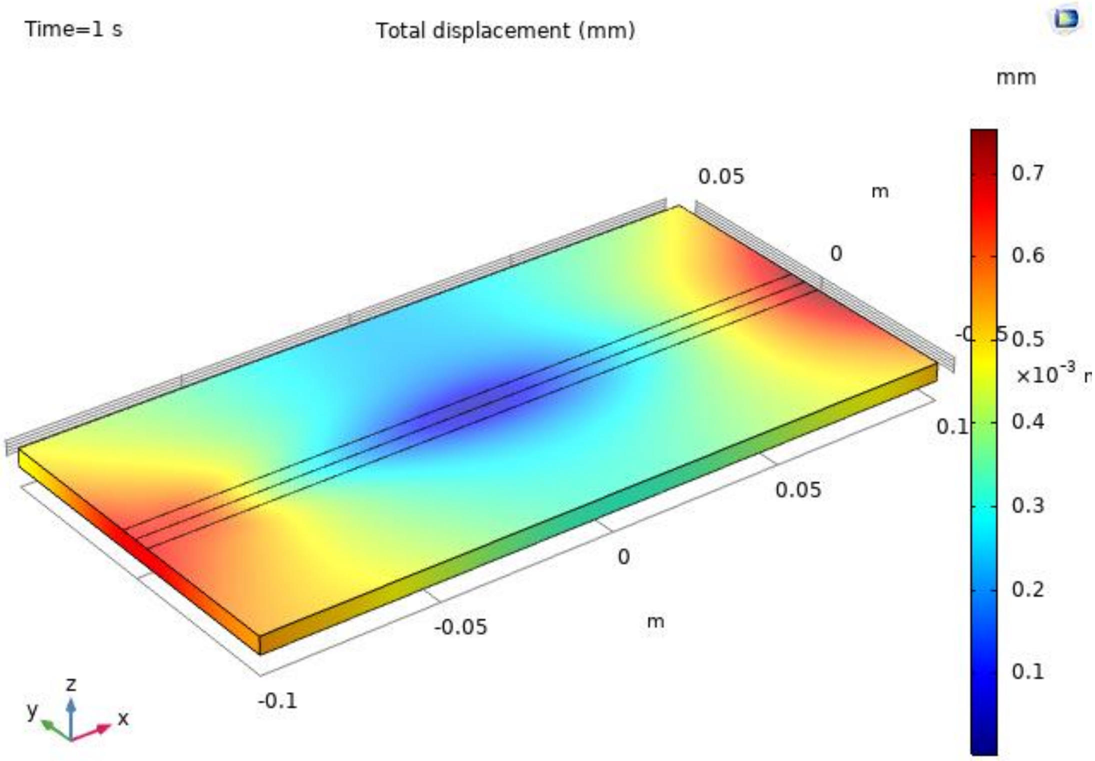


(c)

Figure 3.16 Simulation result of experiment (9). (a) Thermal cycle (b) Displacements (c) Total displacement results displayed by FEM simulations

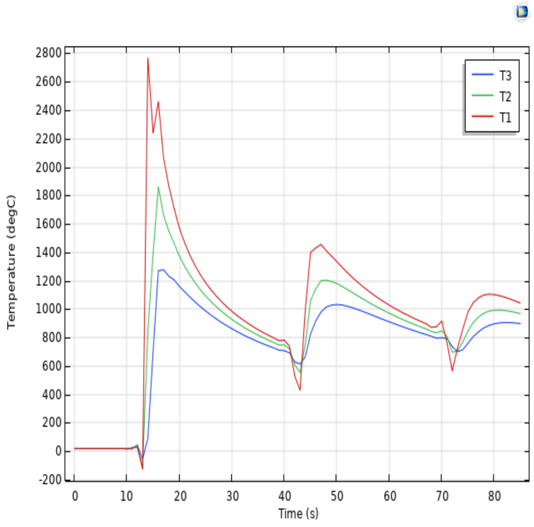


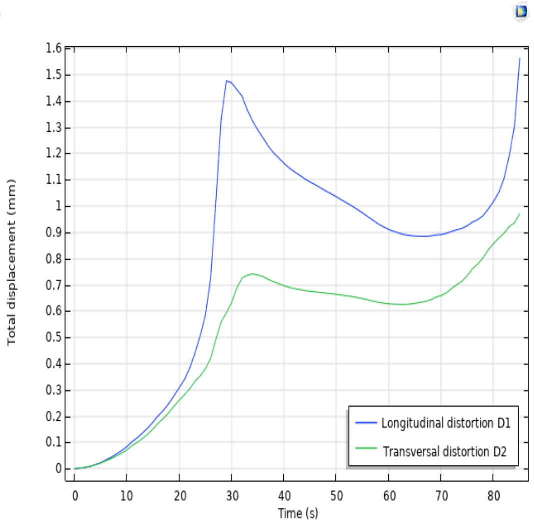


(a) (b)

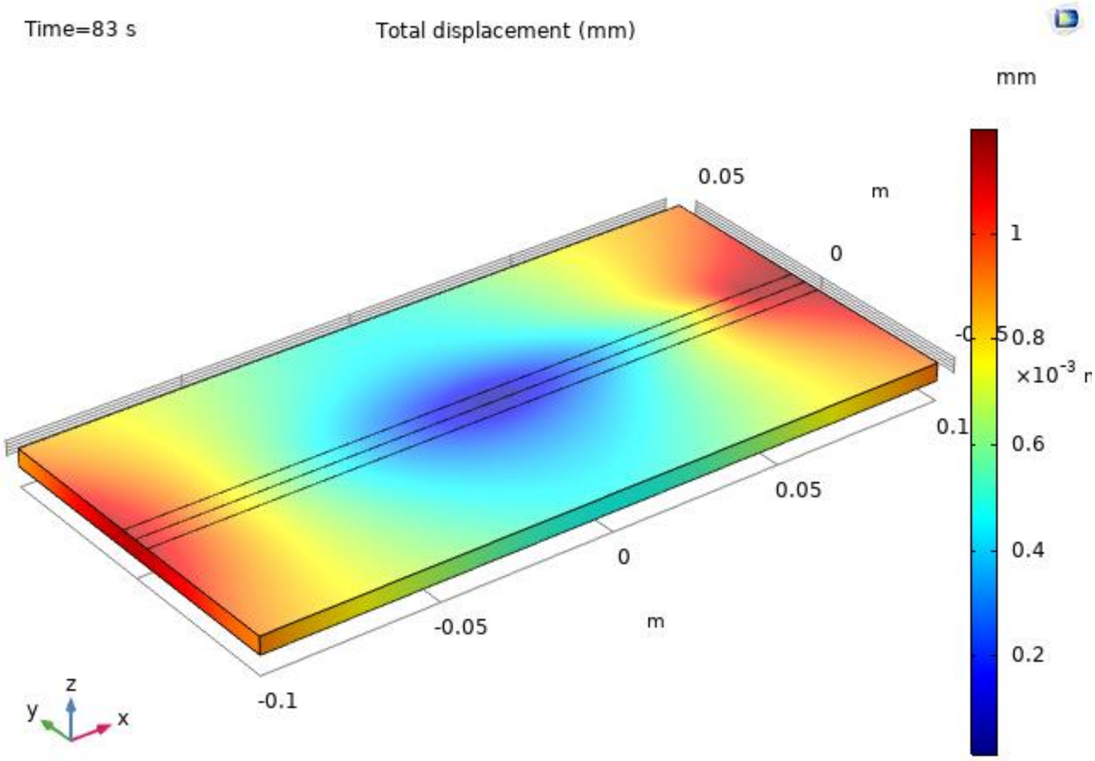


(c)

Figure 3.17 Simulation result of experiment (10). (a) Thermal cycle (b) Displacements (c) Total displacement results displayed by FEM simulations

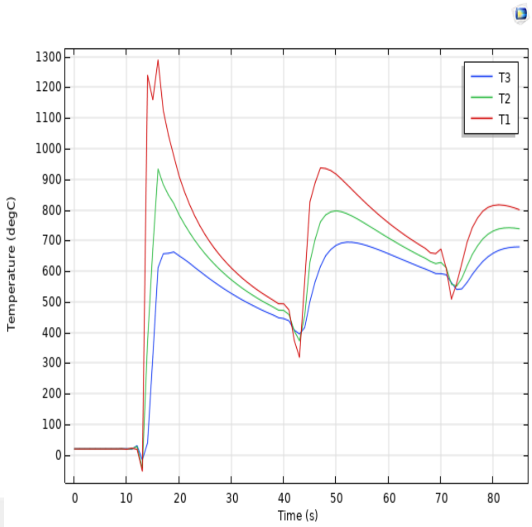


(a)

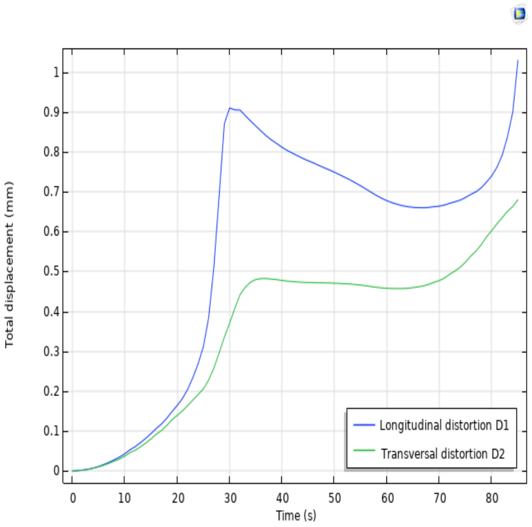


(b)

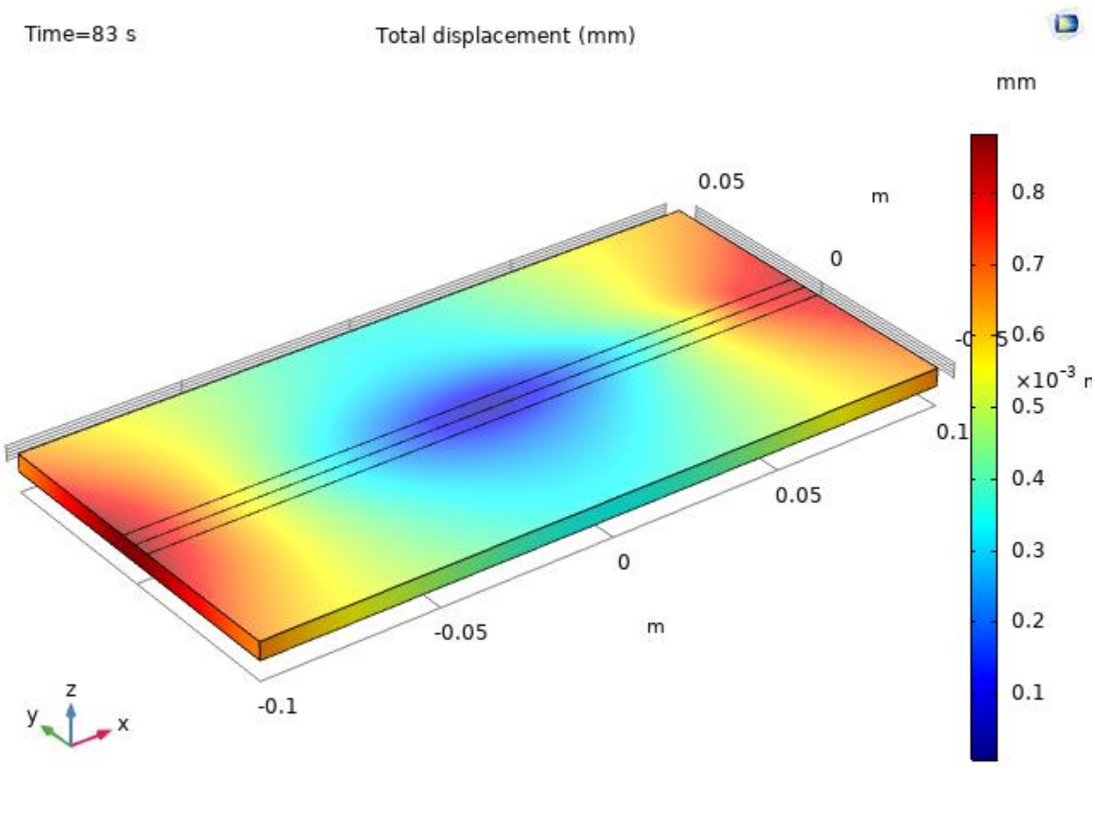


(c)

Figure 3.18 Simulation result of experiment (11). (a) Thermal cycle (b) Displacements (c) Total displacement results displayed by FEM simulations

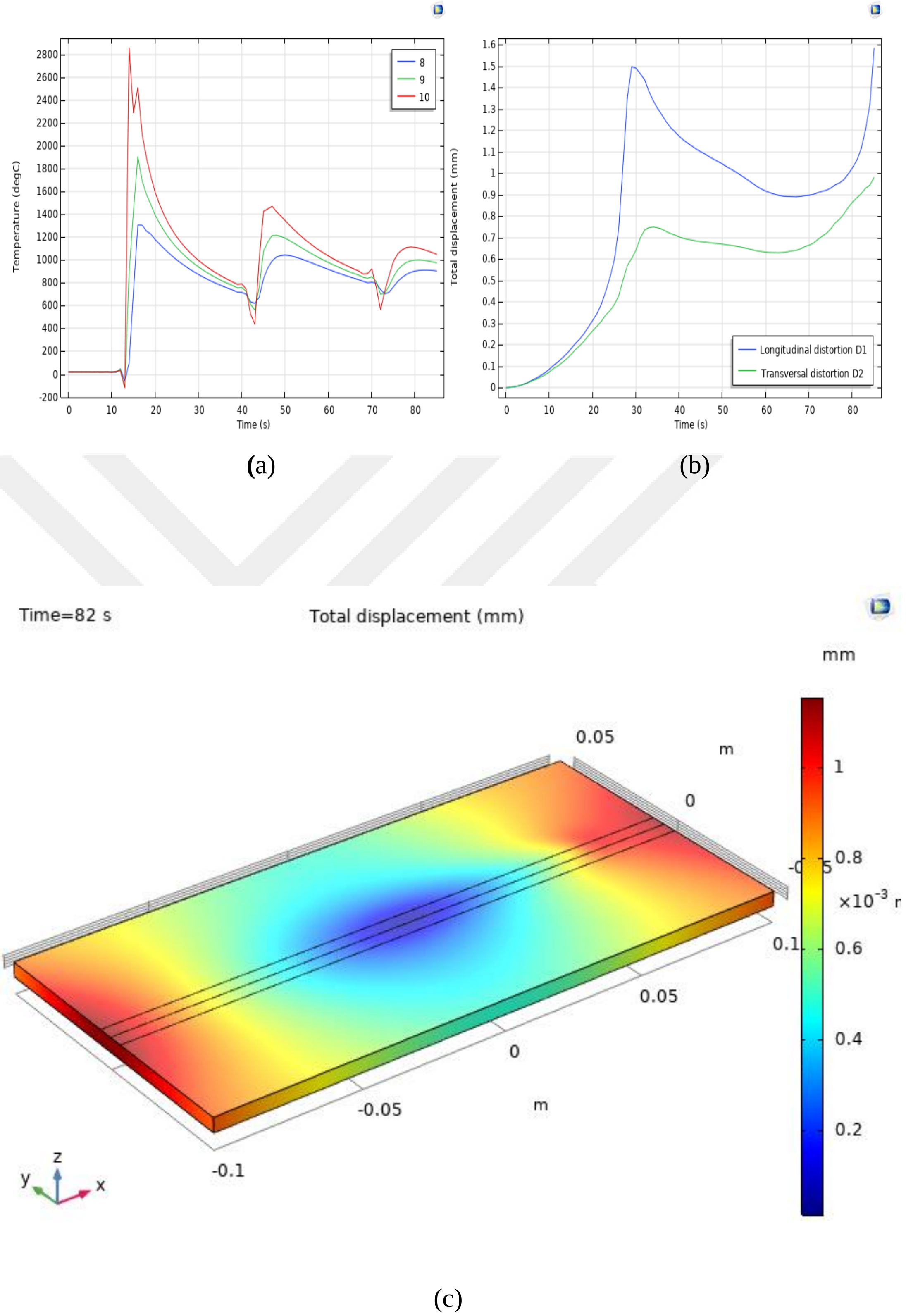


Figure 3.19 Simulation result of experiment (12). (a) Thermal cycle (b) Displacements (c) Total displacement results displayed by FEM simulations

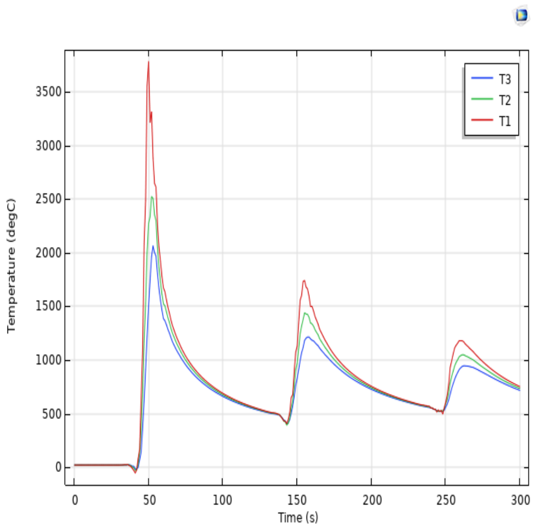


(a)

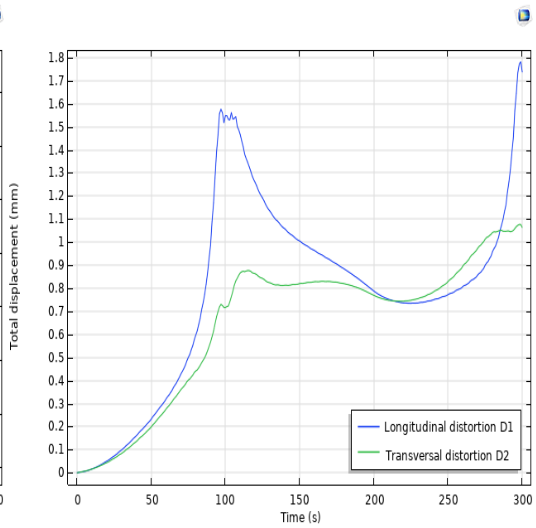


(b)

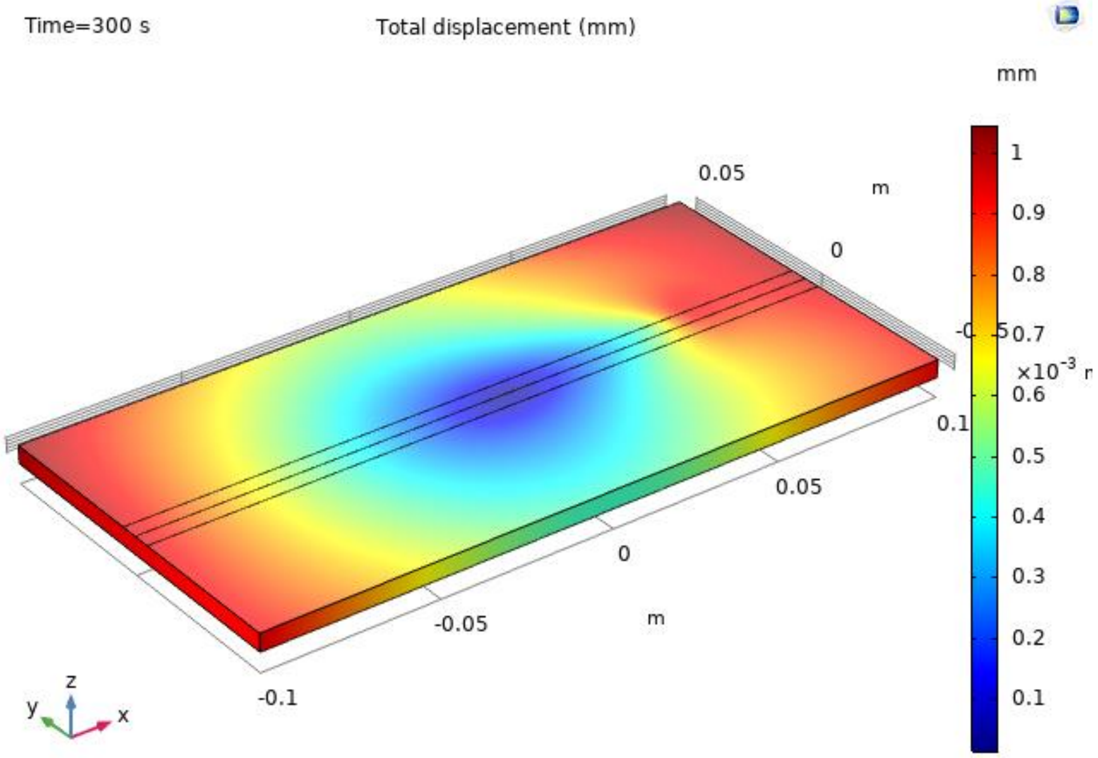


(c)

Figure 3.20 Simulation result of experiment (13). (a) Thermal cycle (b) Displacements (c) Total displacement results displayed by FEM simulations

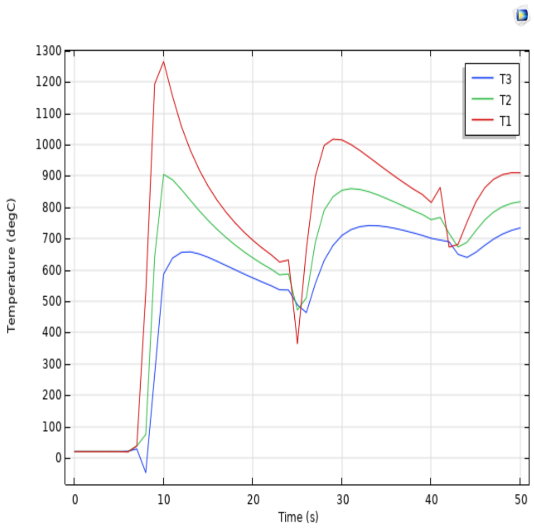


**(a)**

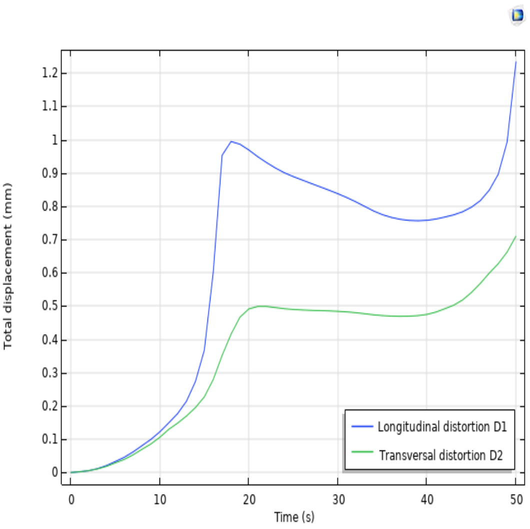


**(b)**

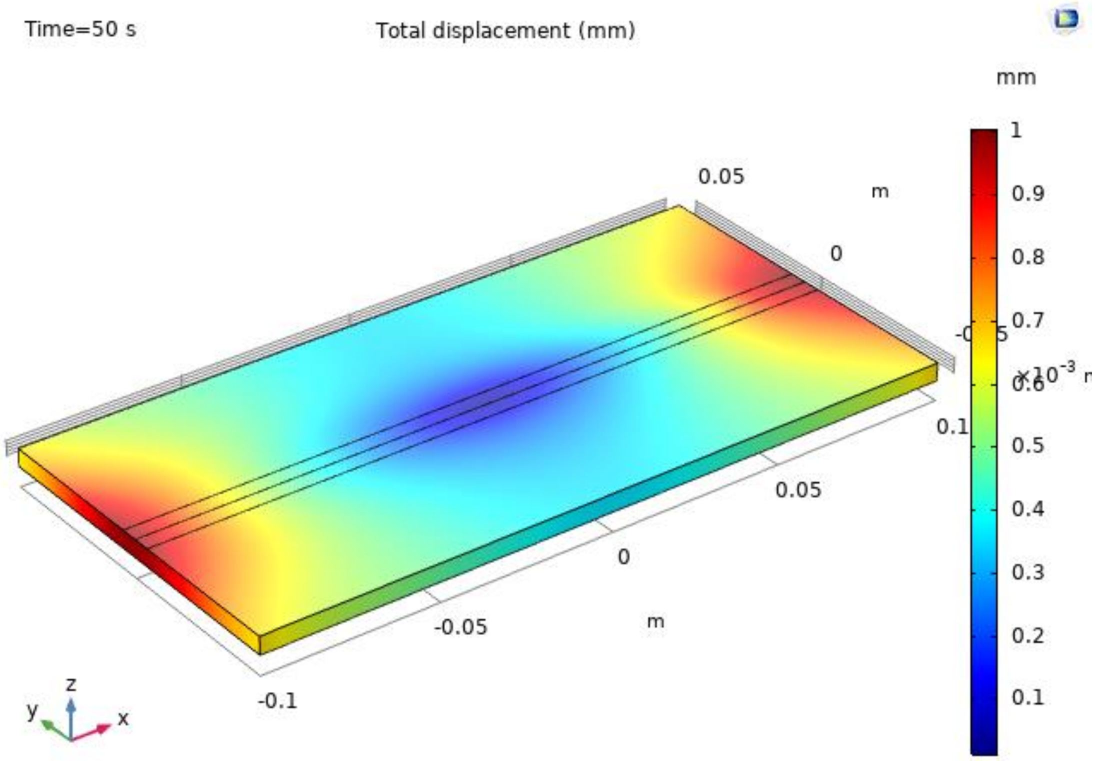


(c)

Figure 3.21 Simulation result of experiment (14). (a) Thermal cycle (b) Displacements (c) Total displacement results displayed by FEM simulations

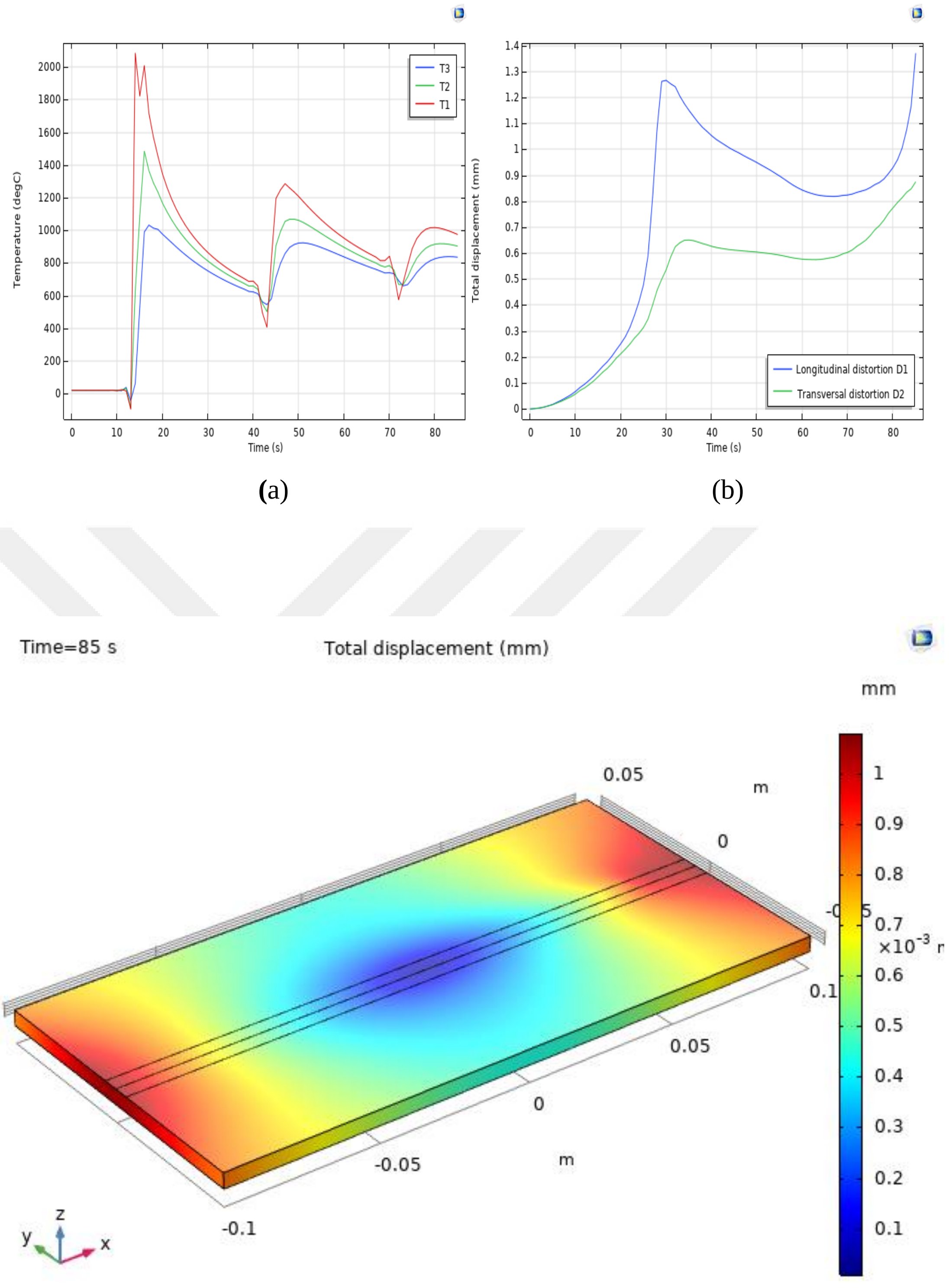


(c)

Figure 3.22 Simulation result of experiment (15). (a) Thermal cycle (b) Displacements (c) Total displacement results displayed by FEM simulations

The values of temperature (T) and displacements resulting from longitudinal and transversal distortions (D1 and D2) for each experiment in design matrix were listed in Table 3.6.

Table 3.6 Response values

| Exp. No | Current (A) | Voltage (V) | Speed (mm/s) | D1 (mm) | D2 (mm) | T (°C) |
|---|---|---|---|---|---|---|
| 1 | 140 | 15 | 4 | 1.41 | 0.88 | 2086 |
| 2 | 220 | 15 | 4 | 1.67 | 1 | 2975 |
| 3 | 140 | 25 | 4 | 1.7 | 1.02 | 3365 |
| 4 | 220 | 25 | 4 | 1.91 | 1.11 | 4100 |
| 5 | 140 | 15 | 10 | 0.95 | 0.56 | 1171 |
| 6 | 220 | 15 | 10 | 1.27 | 0.74 | 1821 |
| 7 | 140 | 25 | 10 | 1.32 | 0.77 | 1922 |
| 8 | 220 | 25 | 10 | 1.65 | 0.93 | 2897 |
| 9 | 112.72 | 20 | 7 | 1.08 | 0.71 | 1389 |
| 10 | 247.28 | 20 | 7 | 1.56 | 0.97 | 2766 |
| 11 | 180 | 11.6 | 7 | 1.03 | 0.68 | 1289 |
| 12 | 180 | 28.41 | 7 | 1.58 | 0.98 | 2854 |
| 13 | 180 | 20 | 2 | 1.74 | 1.06 | 3786 |
| 14 | 180 | 20 | 12 | 1.23 | 0.71 | 1265 |
| 15 | 180 | 20 | 7 | 1.37 | 0.87 | 2085 |
| 16 | 180 | 20 | 7 | 1.37 | 0.87 | 2085 |
| 17 | 180 | 20 | 7 | 1.37 | 0.87 | 2085 |
| 18 | 180 | 20 | 7 | 1.37 | 0.87 | 2085 |
| 19 | 180 | 20 | 7 | 1.37 | 0.87 | 2085 |
| 20 | 180 | 20 | 7 | 1.37 | 0.87 | 2085 |

### 3.10 Creation of Statistical Models

The second-degree response surface function representing the longitudinal and transversal distortion (D1 and D2) dimensions and temperature can be expressed as follows [68]:

$$Y = b_0 + b_1I + b_2U + b_3S + b_{11}I^2 + b_{22}U^2 + b_{33}S^2 + b_{12}IU + b_{13}IS + b_{23}US \quad (3.8)$$

The coefficients values of statistical models were calculated by using Design-Expert software [66] and the results are presented in Table 3.7.

Table 3.7 Coefficient values of models

| Parameter | Coefficient | D1 | D2 | T |
|---|---|---|---|---|
| constant | $b_0$ | 1.37 | 0.87 | 2075.03 |
| I | $b_1$ | 0.14 | 0.072 | 407.48 |
| U | $b_2$ | 0.16 | 0.085 | 502.53 |
| S | $b_3$ | -0.17 | -0.12 | -655.7 |
| $I^2$ | $b_{11}$ | 0.007 | -0.005 | 62.51 |
| $U^2$ | $b_{22}$ | 0.001 | -0.009 | 60.39 |
| $S^2$ | $b_{33}$ | 0.065 | 0.011 | 220.91 |
| IU | $b_{12}$ | -0.005 | -0.006 | 21.37 |
| IS | $b_{13}$ | .023 | 0.016 | 0.12 |
| US | $b_{23}$ | .028 | 0.019 | -72.13 |

The statistical models developed are given below. The WAAM process control variables are in their coded form:

$$D1 = 1.37 + 0.14I + 0.16U - 0.17S + 0.007I^2 + 0.001U^2 + 0.065S^2 - 0.005IU + 0.023IS + 0.028US \quad (3.9)$$

$$D2 = 0.87 + 0.072I + 0.085U - 0.12S - 0.005I^2 - 0.009U^2 + 0.011S^2 - 0.006IU + 0.016IS + 0.019US \quad (3.10)$$

$$T = 2075.03 + 407.48I + 502.53U - 655.7S + 62.51I^2 + 60.39U^2 + 220.91S^2 + 21.37IU + 0.12IS - 72.13US \quad (3.11)$$

The statistical models furnished above can be employed to predict the longitudinal and transversal distortions and temperature for the range of parameters used in the investigation by substituting their respective values in coded form. Based on these models, the interaction effects of the process parameters on the distortion were computed and plotted as response surface and contour surface and depicted in figures from Figure 3.23 to Figure 3.28.

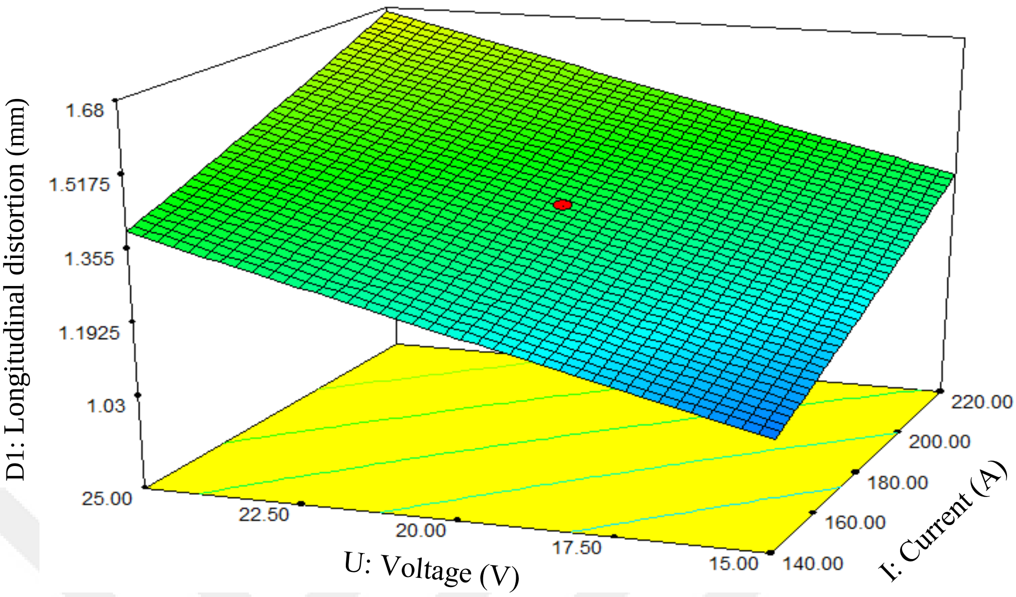


(a)

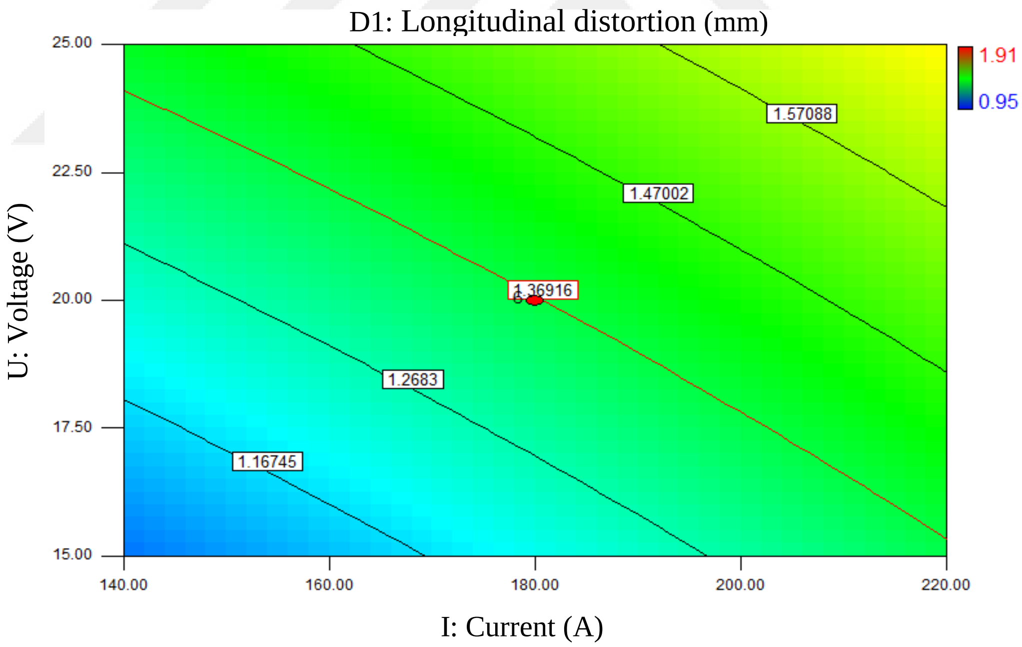


(b)

Figure 3.23 (a) Response surface and (b) contour surface of the interaction effect of current and voltage on longitudinal distortion

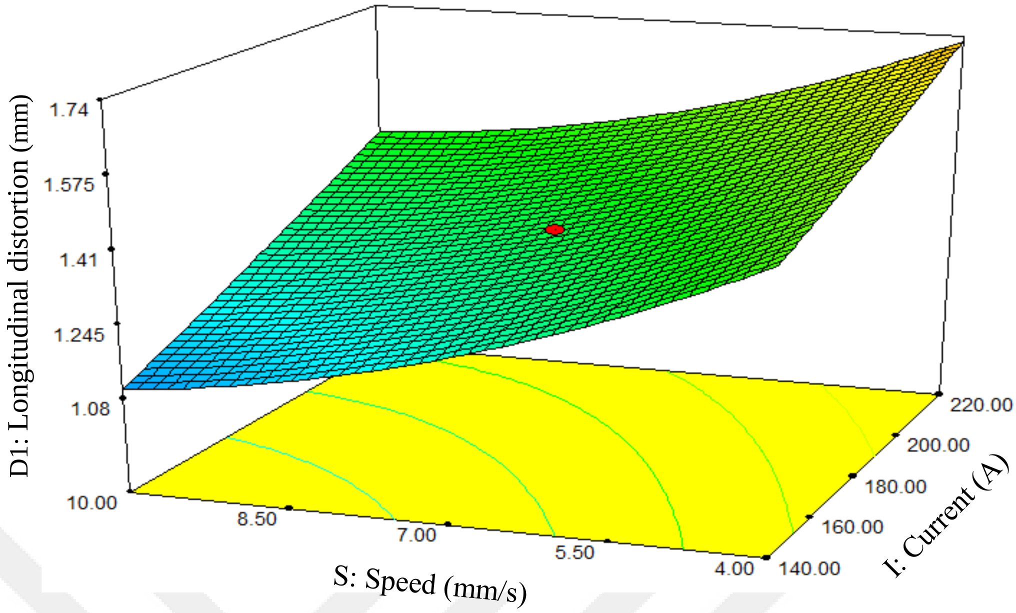


(a)

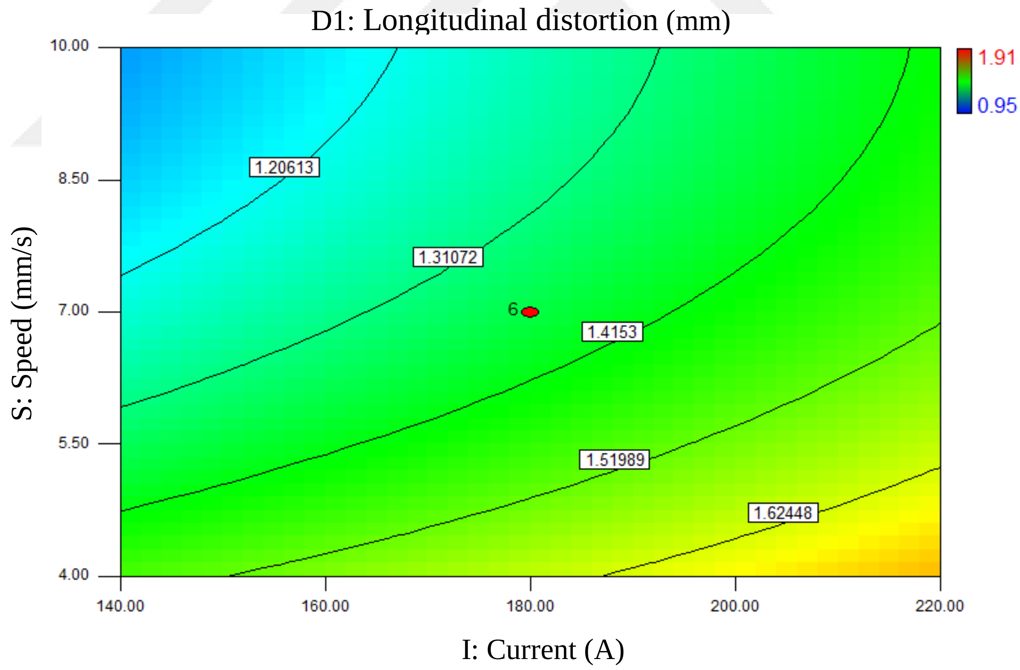


(b)

Figure 3.24 (a) Response surface and (b) contour surface of the interaction effect of current and speed on longitudinal distortion

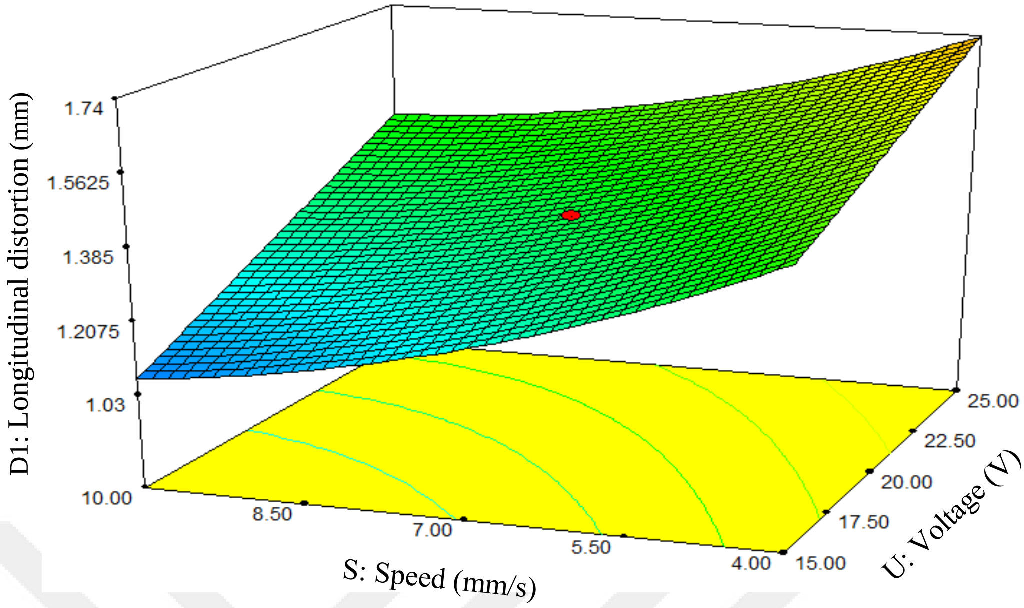


(a)

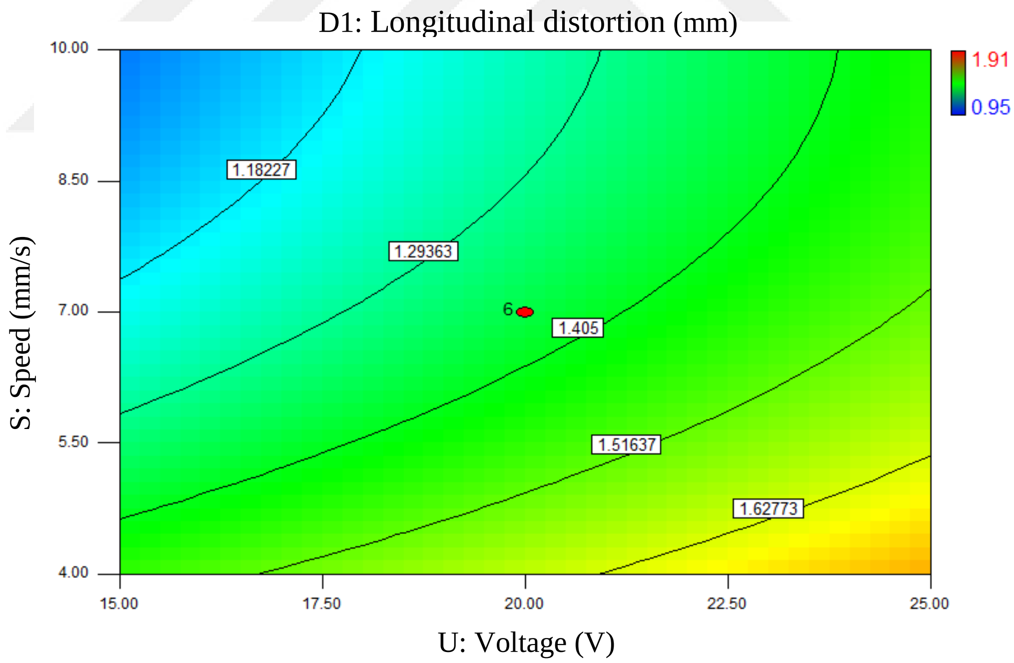


(b)

Figure 3.25 (a) Response surface and (b) contour surface of the interaction effect of voltage and speed on longitudinal distortion

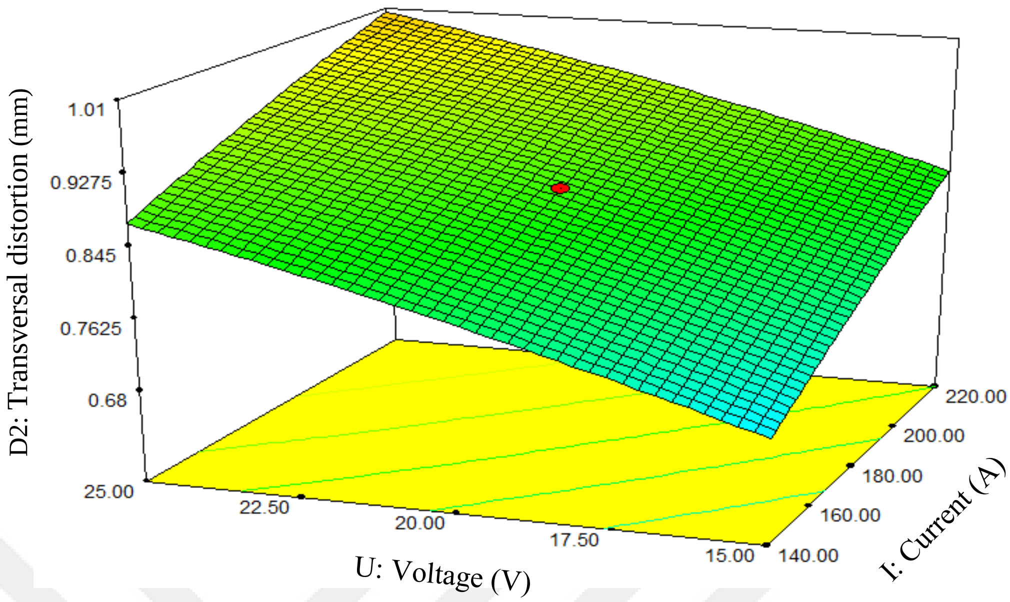


(a)

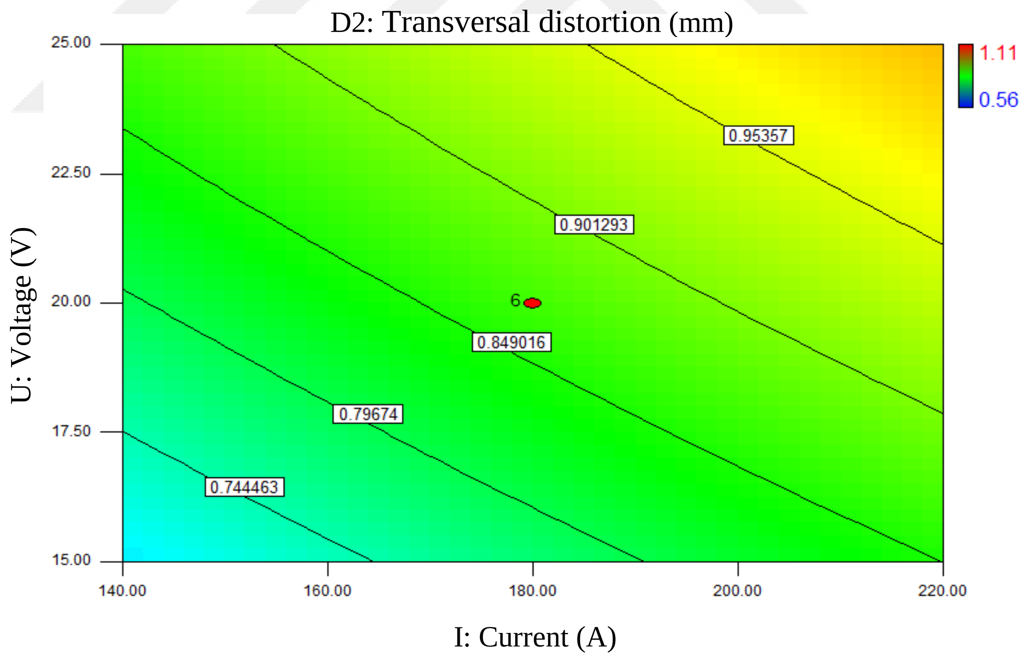


(b)

Figure 3.26 (a) Response surface and (b) contour surface of the interaction effect of current and voltage on transversal distortion

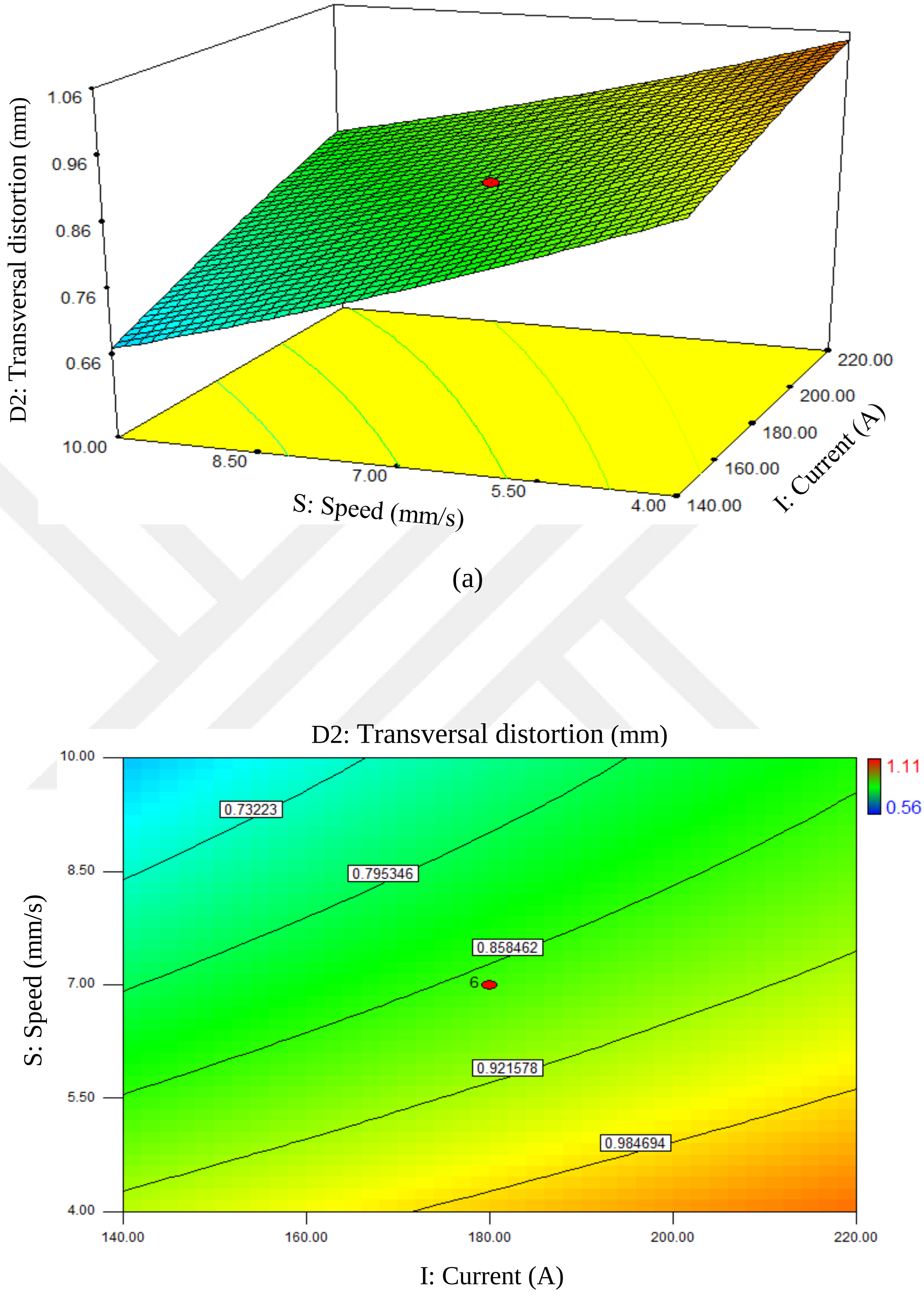


(b)

Figure 3.27 (a) Response surface and (b) contour surface of the interaction effect of current and speed on transversal distortion

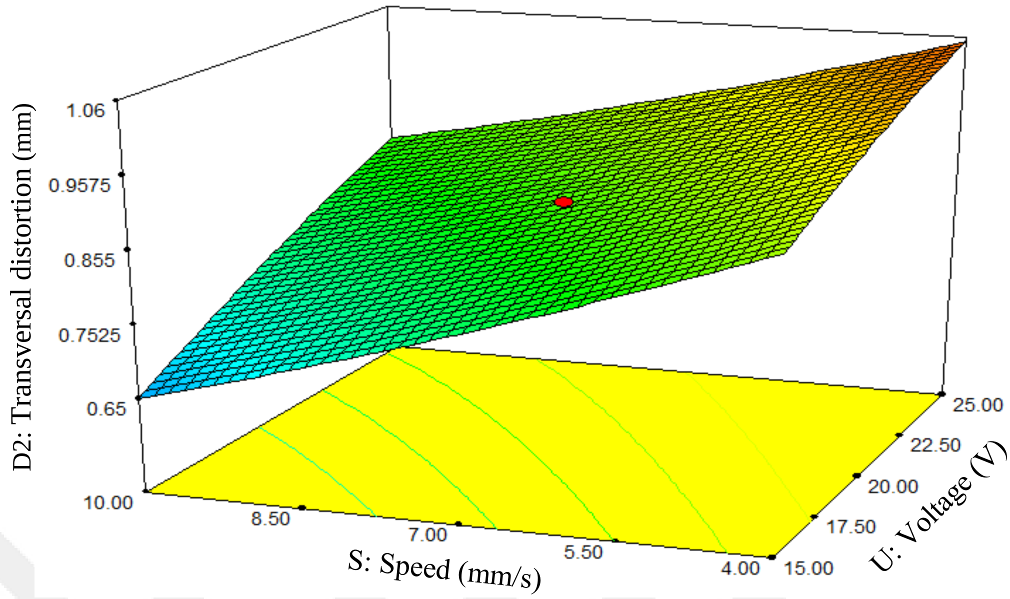


(a)

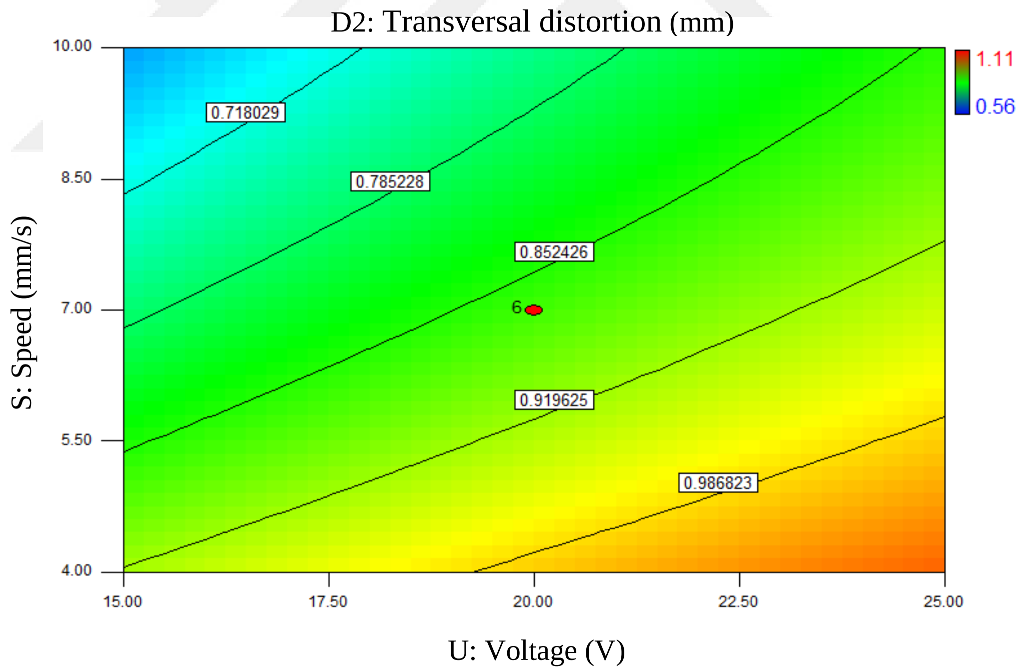


(b)

Figure 3.28 (a) Response surface and (b) contour surface of the interaction effect of voltage and speed on transversal distortion

## 3.11 Checking the Adequacy of the Models

The validity of the models can be judged from the scatter plots shown in Figure 3.29, which indicate that the predicted values of the longitudinal and transversal distortion (D1 and D2) are in good agreement with the results obtained from the simulation.

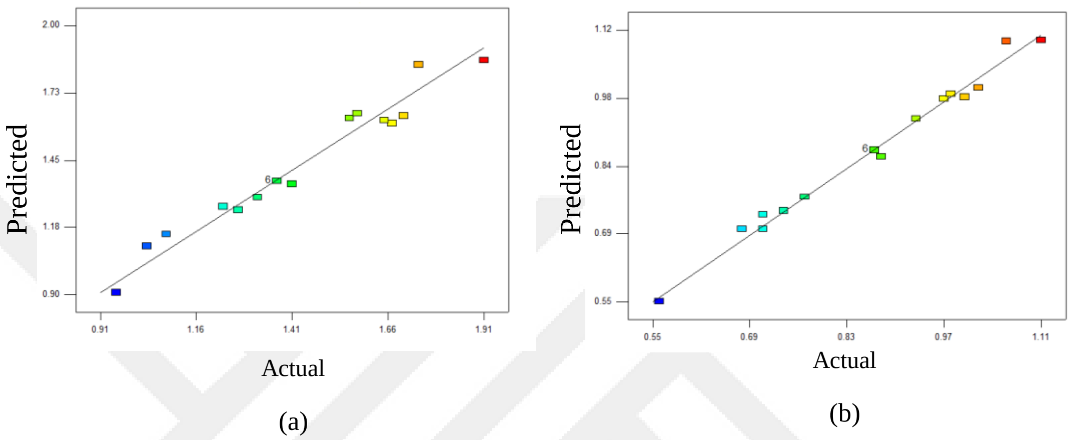


Figure 3.29 Scatter plot of the actual and predicted values for (a) longitudinal and (b) transversal distortion

## 3.12 Optimization

Optimization is searching for combination of factor levels that fulfill the requirements imposed on each of the responses and factors simultaneously. The simultaneous optimization of multiple responses in this work can be performed with help of Design-Expert software by selecting the desired target for each process variable and response. The possible targets are maximization or minimization of the responses. The "importance" of each target can be changed in relation to the other targets from 1 to 5. In this study, importance was chosen to be constant. Table 3.8 shows the suggested criterion for numerical optimization and Table 3.9 shows the most desirable solution selected by the Design-Expert software.

Table 3.8 Criterion of numerical optimization

| Name | Goal | Lower limit | Upper limit | Importance |
|---|---|---|---|---|
| Current (I) A | In range | 140 | 220 | 3 |
| Voltage (U) Volt | In range | 15 | 25 | 3 |
| Speed (S) mm/s | In range | 4 | 10 | 3 |
| Temperature (T) °C | In range | 1500 | 2500 | 3 |
| Longitudinal distortion (D1) mm | Minimize | 0.95 | 1.91 | 3 |
| Transversal distortion (D2) mm | Minimize | 0.56 | 1.11 | 3 |

Table 3.9 Desirable solution selected

| Name | Desirable value |
|---|---|
| Current (I) A | 200 |
| Voltage (U) volt | 15 |
| Speed (S) mm/s | 10 |
| Temperature (T) °C | 1500 |
| Longitudinal distortion (D1) mm | 1.17 |
| Transversal distortion (D2) mm | 0.70 |

## 3.13 Discussion

### 3.13.1 Interaction effects of welding current and voltage on distortion

As can be seen in Figure 3.23 and Figure 3.26, the longitudinal and transversal distortions increase with increasing voltage and current because both have a positive relationship with distortion. The longitudinal and transversal distortions are at their maximum values of 1.68 mm and 1.01 mm, respectively when the welding current and voltage are at their maximum values.

### 3.13.2 Interaction effects of welding current and welding speed on distortion

The interaction effect of current and welding speed on distortion is shown in Figure 3.24 and Figure 3.27, the current has a positive relationship with distortion, while speed has a negative relationship. As result, the value of distortion increases with the increase in current for all values of speed. However, the rate of increase for distortion gradually decreases as speed increases from its lower limit to upper limit. The longitudinal and transversal distortions are at their maximum values of 1.74 mm and 1.06 mm, respectively when the welding current is at its maximum value and speed is at its minimum value.

### 3.13.3 Interaction effects of welding voltage and welding speed on distortion

The distortion increases as voltage increases for all values of speed. However, the rate of increase for distortion gradually decreases as the speed increases as shown in Figure 3.25 and Figure 3.28. The longitudinal and transversal distortions are at their maximum values of 1.74 mm and 1.06 mm, respectively when the welding voltage is at its maximum value and speed is at its minimum value.

# CHAPTER 4

# EXPERIMENTAL STUDIES

## 4.1 General

This chapter is devoted to the experimental studies and divided into six sections. In section 4.2, the delivery conditions and chemical compositions of substrate and additive filler metals are introduced. Section 4.3 deals with build-up of the wire arc additive manufactured layers. Inspection procedures for integrity assessment of additively manufactured beads were addressed in section 4.4. This section is followed by sections 4.5 and 4.6, which give the descriptions of mechanical and metallurgical characterization techniques, respectively. The last section 4.7 forms the main focal issue of the thesis, as it concerns fracture toughness testing using single edge notched tension (SENT) specimens.

## 4.2 Materials

Three different steels have been employed in this experimental work:

1- Super duplex stainless steel rolled plates grade 2507 with a thickness of 12 mm were subjected to the investigation and conformed to ASTM A240 S32750 and EN 10088-2 X2CrNiMoN 25-7-4 (1.4410) [73, 74].

2- Austenitic stainless steel grade ASTM A240 316L plates with the dimensions of 400 mm × 200 mm × 10 mm were used as substrates to carry out the experiments. This work was focused only on the AM layers and did not include the interface layer; hence it was not mandatory to use SDSS plates as substrate.

3- Grade 2209 duplex stainless steel filler wire which was standardized as per SFA/AWS 5.9 ER2209 and ISO 14343-A G 22 9 3 N L was used as the feedstock material in the first experiments [75].

4- Grade 2509 super duplex stainless steel filler wire which was standardized as per SFA/AWS 5.9 ER2594 and ISO 14343-A G 25 9 4 N L was used as the feedstock material in the second experiments [75].

The chemical compositions of steels used are shown in Table 4.1.

Table 4.1 Chemical compositions of the steels used (wt%). [73, 75]

| Material | C | Cr | Ni | Mo | Mn | Si | N |
|---|---|---|---|---|---|---|---|
| Grade 2507 as received Plate | 0.02 | 24.7 | 6.6 | 3.6 | 0.8 | 0.32 | 0.28 |
| Grade 2209 filler wire for WAAM | 0.01 | 22.7 | 8.5 | 3.2 | 1.5 | 0.5 | 0.17 |
| Grade 2509 filler wire for WAAM | 0.01 | 25.2 | 9.4 | 3.9 | 0.4 | 0.4 | 0.24 |
| Grade 316L Plate ( substrate for WAAM ) | 0.03 | 16.8 | 10.7 | 2.1 | 2.0 | 0.75 | 0.1 |

## 4.3 Wire Arc Additive Manufacturing Procedure

### 4.3.1 Equipment

The system used to perform additive manufacturing deposition is composed by the integration of two different systems:

- Welding system. In this work, the semi-automatic Fronius TPS 4000 CMT power source was used as the WAAM process. This WAAM method provides relatively low-heat input with high deposition rate.
- Three-axis movement system, the motion of the system should be easily controlled.

The power source used for the described experimental work in this section is shown in the Figure 4.1.

### 4.3.2 Sample Build-up

Cold metal transfer welding technique was used to deposit all beads. A reversed polarity (electrode positive) direct current (DCEP) between the wire electrode and the substrate was used in all runs. Two blocks with the size of 400 mm × 200 mm × 30 mm were deposited using Grade 2209 duplex stainless steel filler metal and Grade 2509 super duplex stainless steel filler metal severally. The substrate was Grade 316L austenitic stainless steel plate. The plate was cleaned to remove dirt, located at flat position, aligned on the platform manually and clamped by the help of pneumatic cylinders. After clamping, the beads are built in a zigzag direction until 13 layers of material have been deposited using mechanized torch. Schematic WAAM setup could be seen in Figure 4.2. The employed welding parameters which were obtained from simulation studies in Chapter 3, were kept constant for all deposited layers as given in the Table 4.2. To protect the weld pool from atmospheric contamination a mixture of Ar + 2% $O_2$ was used as shielding gas. The real sample which was welded for investigation is shown in Figure 4.3.


Figure 4.1 Fronius TPS 4000 CMT power source

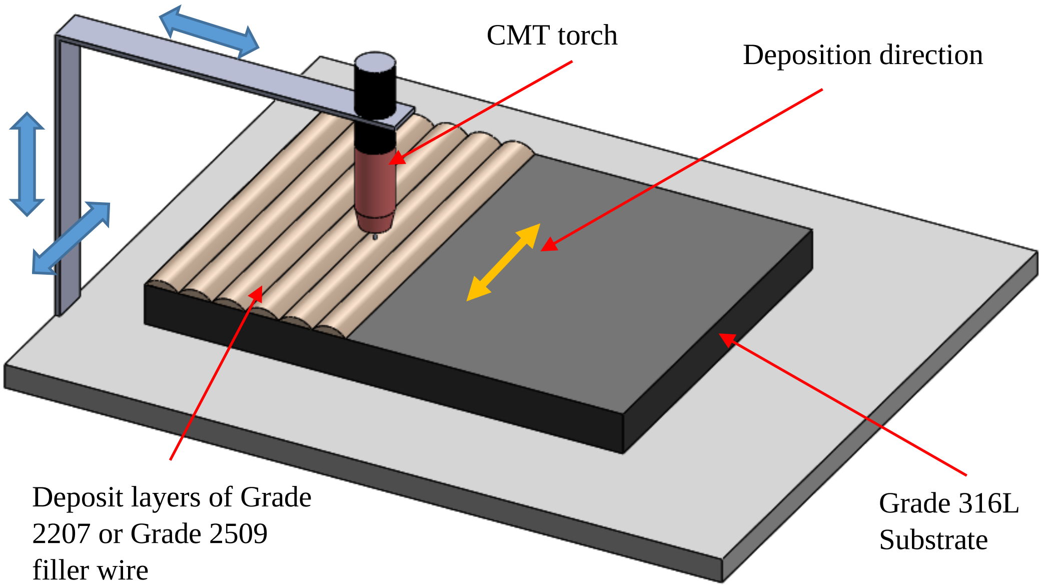


Figure 4.2 Schematic of WAAM setup

Table 4.2 Constant process parameters.

| Parameter | Setting |
|---|---|
| Welding process | CMT |
| Welding position | PA (1G) |
| Average current | 200 A |
| Average voltage | 15 V |
| Welding speed | 10 mm/s |
| Shielding gas flow rate | 18 L/min |
| Contact tube distance | 12 mm |

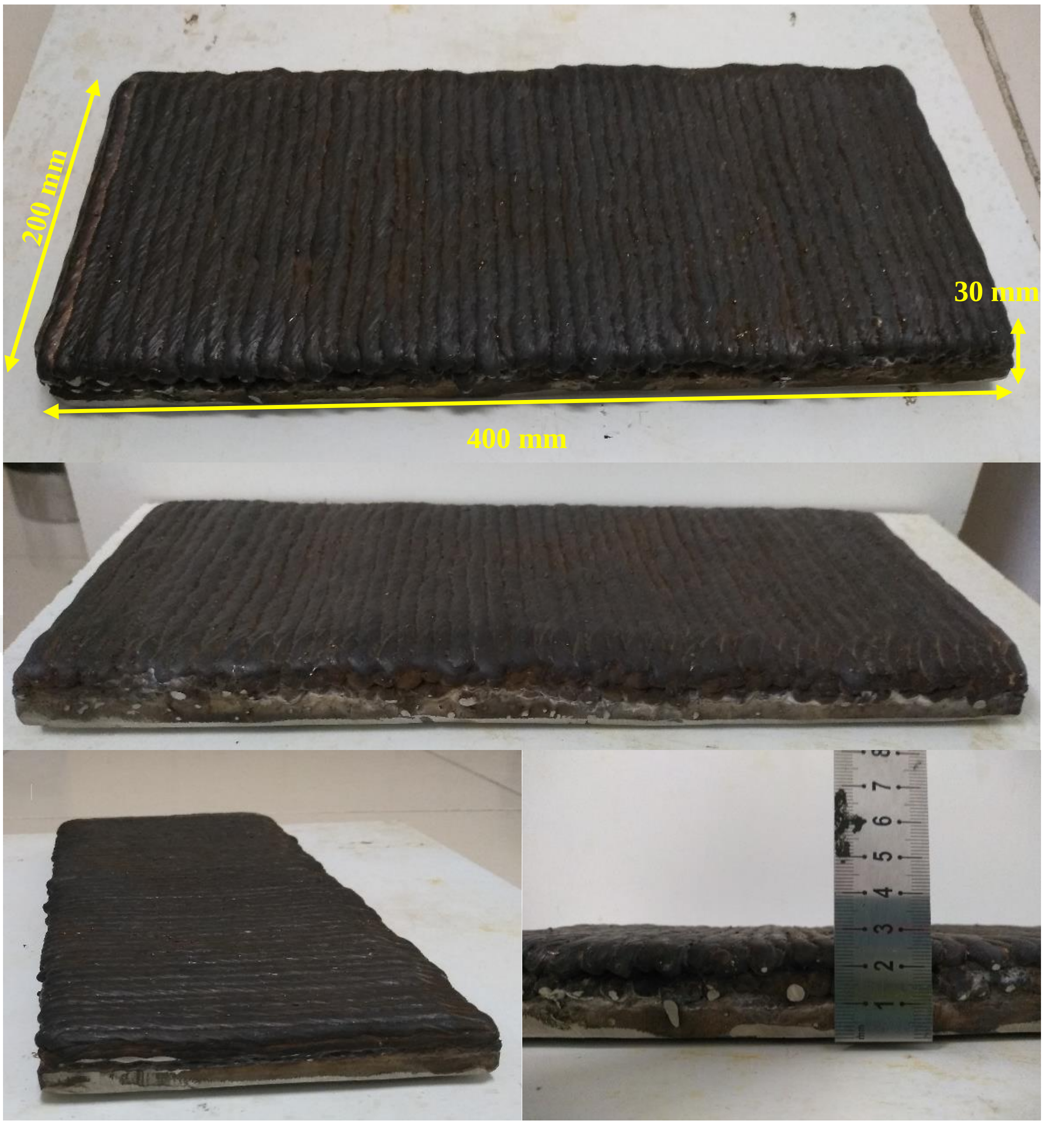


Figure 4.3 Real WAAM’d sample for Grade 2509

## 4.4 Integrity Assessment of the Additively Manufactured Beads

Deposited beads performed by WAAM were visually inspected to check surface imperfections. To examine possible volumetric discontinuities, X-ray radiographic examination was applied according to ASTM E1742 [76] and films were evaluated as per the requirements and definitions in ASME BPV Code Section IX [77]. The quality level employed for radiography was 2 % (2-2T using hole type IQI).

## 4.5 Mechanical Characterization

### 4.5.1 Tensile Test

In order to determine mechanical properties (strength and ductility) of the super duplex stainless steel, tensile tests were carried out with a universal tensile testing machine (BESMAK BMT-E series) using round shape tensile samples which were prepared according to ASTM E8 standard [78]. Figure 4.4-a shows the dimensions of the samples. Five samples were cut from the received plate of SDSS Grade 2507 as shown in Figure 4.4-b. Moreover, as depicted in Figure 4.4-c, two samples were sectioned from the additively manufactured plate of SDSS Grade 2509.

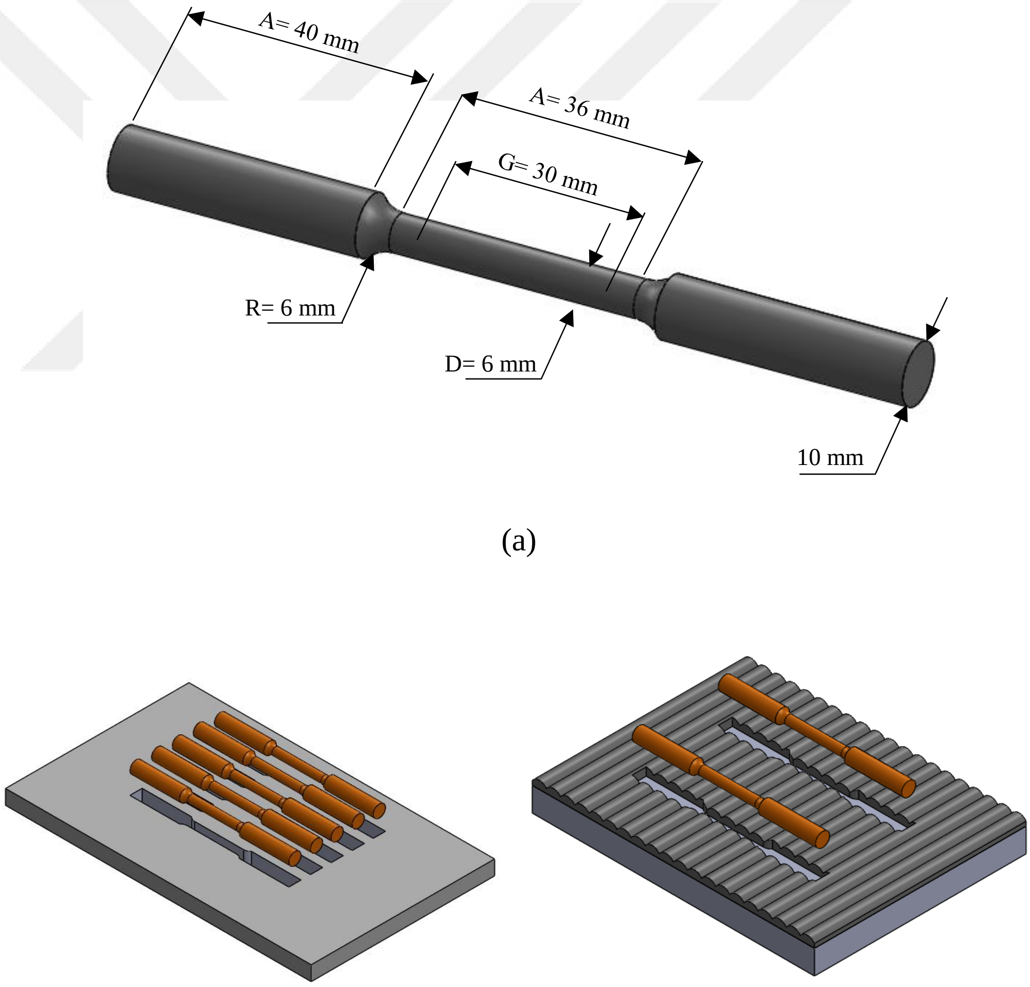


(a)

(b) (c)

Figure 4.4 Tensile test samples

### 4.5.2 Hardness Test

In order to investigate the effects of the thermal cycles on the hardness, Vickers micro hardness measurements were taken along the deposited material of Grade 2509. The indentations were made under the load of 0.5 kg over 10 s with a distance of 0.3 mm between the indentations. Sections perpendicular to the deposition direction were cut, prepared and examined in the etched condition. The specimens were prepared and tested according to ISO 6507 standard [79].

## 4.6 Microstructural Examination

Because of critical effect of microstructure upon the fracture behavior of a material, thorough analysis of the microstructure was required for the rolled plate grade 2507 and additively manufactured layers of Grade 2509 SDSS . Samples were extracted from rolled plate as well as additively manufactured layers and subjected to metallographic examination. Samples were hot-mounted in conductive bakelite and grinded for macro-etch inspection with different grades of SiC papers which is helpful in making sure whether imperfections are present or not. For microstructural examinations, specimens were further grinded and polished using 6, 1 and ¼ µm colloidal alumina suspension. The samples were etched using the etchant that contains 20 ml HCl+20 ml ethyl alcohol+1 g $CuCl_2$. The samples were examined using optical microscope (OM) to measure the size of grains as per ASTM E112 [80] and volume fraction of phases by manual point count as per ASTM E562 [81] and by an image analysis software as per ASTM E1245 [82].

## 4.7 Fracture Toughness Testing using SENT According to BS 8571

As specified in the BS 8571 standard SENT specimens were machined with a square cross-section [62]. The specimen dimensions, including initial crack length, are shown in Figure 4.5. For the base material characterization, the six specimens were taken out from the SDSS as-received plate, for the WAAM characterization, the other six specimens were taken out from the deposited SDSS.

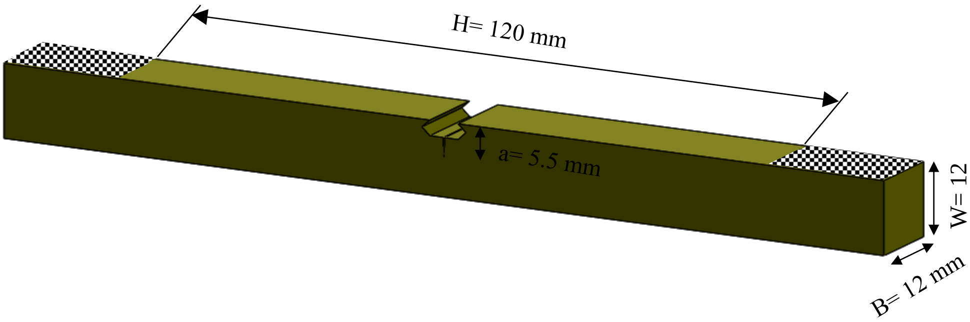


Figure 4.5 SENT specimens

All the specimens were notched using electro-discharge machining, with a Ø300µm wire to reach an initial crack length of 4 mm. As depicted in Figure 4.6, the notch orientation of the rolled plate specimens was parallel to the rolling direction and for the WAAM'd plate specimens the notch orientation was perpendicular to the deposition direction.

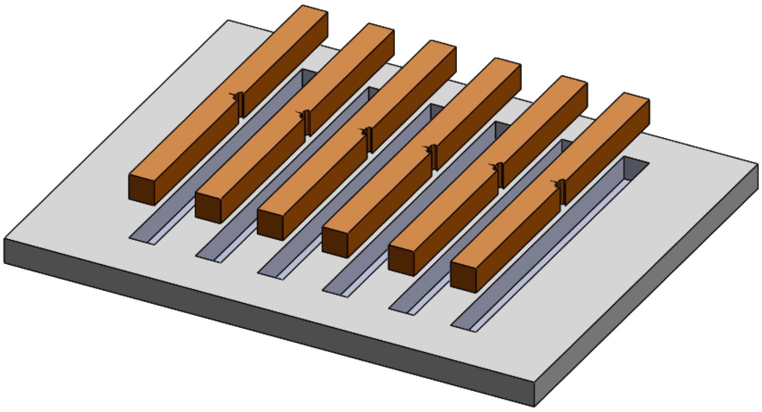

(a)

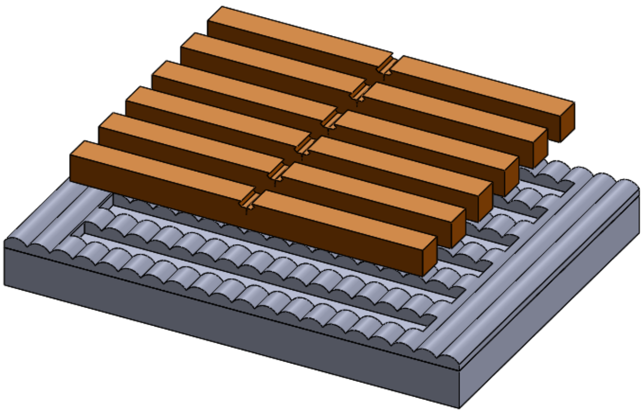

(b)

Figure 4.6 Orientations of the SENT samples: (a) As-received plate, (b) Additively manufactured sample, Grade 2207

For the deposited 2509 Grade SDSS characterization, the other six specimens were taken out from the additively manufactured part, here the study was focused on the overlapped heat affected zone (OHAZ) as depicted in Figure 4.7. The (OHAZ) phrase here is defined as the critical zone that is affected by heat more than once. So that, the location of pre-crack was chosen carefully.

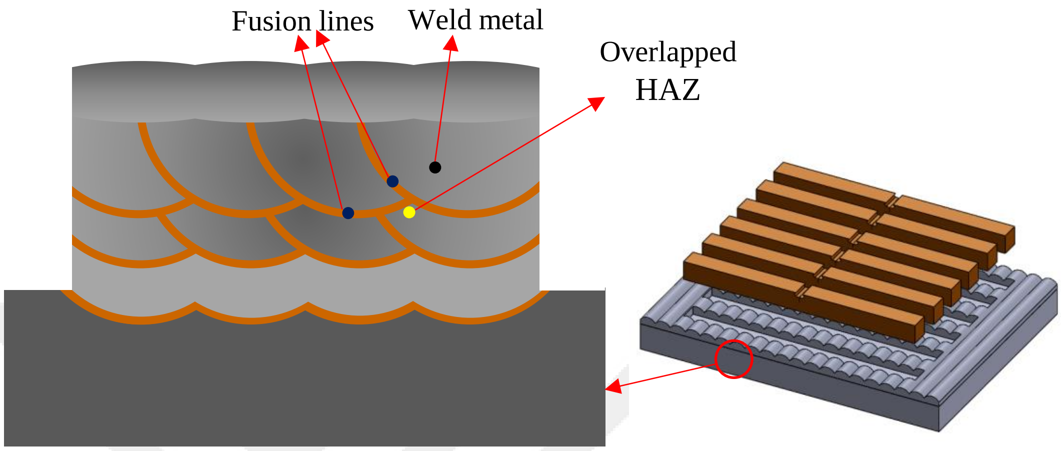


Figure 4.7 SENT specimens place and orientation in HAZ for Grade 2509

The notched specimens were fatigue pre-cracked in three-point bending (see Figure 4.8) at room temperature within the limits of ISO 12135 standard [61]. The pre-crack length was chosen to be 1.5 mm. Universal tensile testing unit was used to conduct the fracture toughness tests at a temperature of -10°C, which is the expected service temperature for the offshore equipment to be manufactured out of SDSS. Localized cooling was applied to cool down the specimens using a flow of liquid nitrogen vapor as illustrated in Figure 4.9.

Tests were performed at a range of crack extensions between 0.45 mm and 0.90 mm for the specimens from as-received rolled plate and between 0.3 mm and 1.08 mm for the WAAM specimens which satisfied standard criteria (0.2 mm to 20% of the specimen ligament ($W-a_0$)) [62]. The results for each specimen (load vs. CMOD) were used to provide one point on the J R-curve.

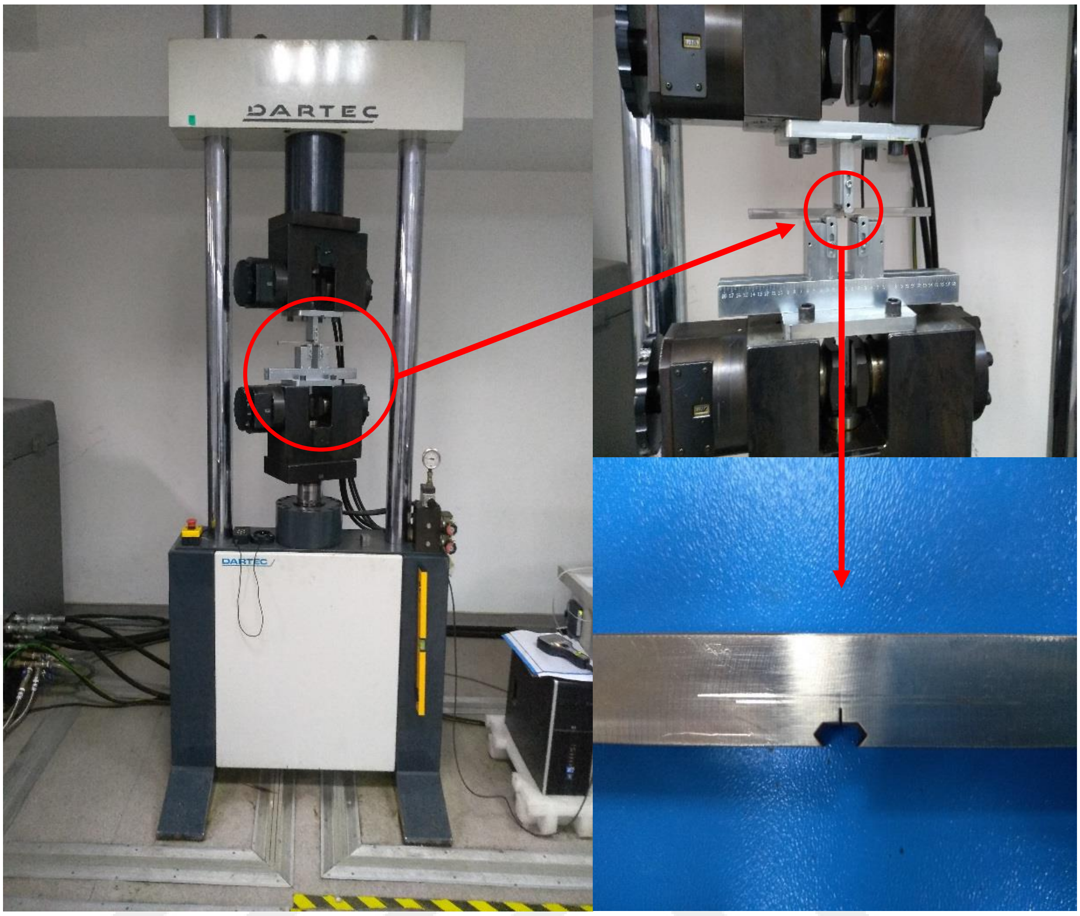


Figure 4.8 Fatigue pre-crack

Figure 4.9 Fracture toughness test setup

### 4.7.1 Post-Test Measurements

After executing the SENT tests, measurements of the samples were taken, and data analysis is carried out to determine a value for the fracture toughness. First, heat tinting was performed on the specimens by heating them up to 300°C. Then they were quenched in a bath of liquid nitrogen (-196°C) before they were broken. Due to the brittle behavior of the quenched samples they were broken without any further plastic fracture behavior.

High resolution images of broken samples were taken. As prescribed by the ISO 12135 standard, nine reference measurements points were plotted on each image as indicated in Figure 4.10 [61]. The outer two positions of measurement are taken at 0.01 times the total sample width, and the remaining 7 measurements are spaced evenly with each other. Image analysis software ImageJ [83] was used to perform the measurements. The value of $a_o$ is obtained by equation 4.1.

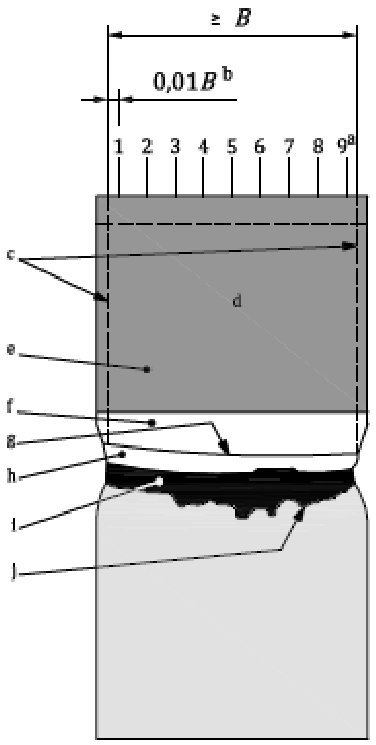


a Measure initial and final crack lengths at positions 1 to 9.
b Not to scale.
c Reference lines.
d Crack plane.
e Machined notch.
f Fatigue precrack.
g Initial crack front.
h Stretch zone.
i Crack extension.
j Final crack front.
k Side groove.

Figure 4.10 Measurement of crack length [59].

$$a_0 = \frac{1}{8}\left[\left(\frac{a_1 + a_9}{2}\right) + \sum_{j=2}^{j=8} a_j\right] \quad (4.1)$$

### 4.7.2 Calculating J

J shall be calculated at the assessment point using equation (4.2):

$$J = J_{el} + J_{pl} = \frac{K^2}{E'} + \frac{\eta_p U_p}{B b_0} \tag{4.2}$$

$$E' = E/(1-\upsilon^2) \tag{4.3}$$

where

$J_{el}$ = elastic part of the J-integral which directly linked to the Stress Intensity Factor K.

$J_{pl}$ = plastic part of the J-integral.

E’ = E for plane stress (E is Young’s modulus).

ν is Poisson’s ratio.

$b_0$ = (W-$a_0$) is the remaining ligament.

$a_0$ is the initial crack length.

ηp is a dimensionless function of the geometry.

Up is the area under the plastic part of the load versus crack mouth opening displacement (CMOD) curve, in (N·mm) (see Figure 4.11).

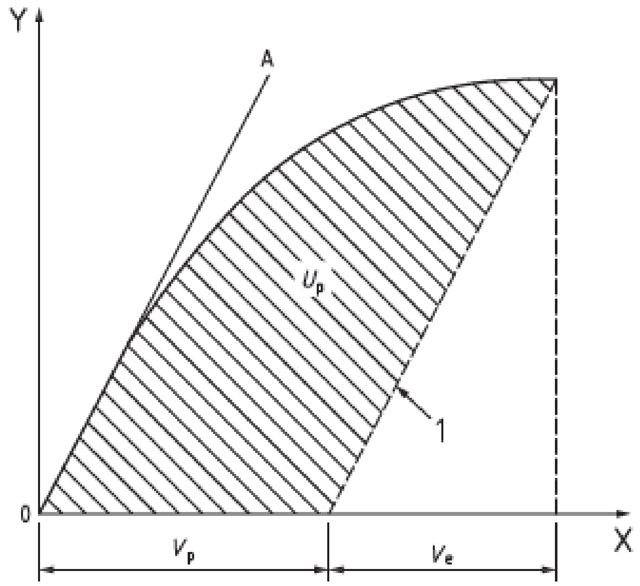


**Key**

X Crack mouth opening displacement

Y Applied force

1 Line parallel to the elastic part of the load-displacement trace (line 0A), offset to intersect at the point of assessment

Figure 4.11 Load versus CMOD curve

Stress Intensity Factor K for clamped specimens shall be calculated using equation 4.4

$$K = \left[\frac{P\sqrt{\pi a_0}}{(B.B_N)^{0.5}W}\right] G\left(\frac{a_0}{W}\right) \tag{4.4}$$

where:

$$G\left(\frac{a_0}{W}\right) = \sum_{i=1}^{12} t_i \left(\frac{a_0}{W}\right)^{i-1} \tag{4.5}$$

where $t_i$ for H/W = 10 are as follows and valid for $0.05 \leq a0/W \leq 0.95$:

| **i** | **$t_i$** | | **i** | **$t_i$** |
|---|---|---|---|---|
| 1 | 1.197 | | 7 | −36.137 |
| 2 | −2.133 | | 8 | 51.215 |
| 3 | 23.886 | | 9 | −6.607 |
| 4 | −69.051 | | 10 | −52.322 |
| 5 | 100.462 | | 11 | 18.574 |
| 6 | −41.397 | | 12 | 19.465 |

J is calculated using equation 4.2 and equation 4.6:

$$\eta_p = \sum_{i=0}^{10} \varphi_i \left(\frac{a_0}{W}\right)^{i} \tag{4.6}$$

Where $\varphi_i$ for H/W = 10 are as follows and are valid for $0.05 \leq a_0/W \leq 0.7$:

| i | $\varphi_i$ | | i | $\varphi_i$ |
|---|---|---|---|---|
| 0 | 1.000 | | 6 | −77.984 |
| 1 | −1.089 | | 7 | 38.487 |
| 2 | 9.519 | | 8 | 101.401 |
| 3 | −48.572 | | 9 | 43.306 |
| 4 | 109.225 | | 10 | −110.770 |
| 5 | −73.116 | | | |

### 4.7.3 Definition of the R-curve

The data were plotted as fracture toughness J against the stable crack extension, Δa. The J–R curve line was fitted to the test data as a lower-bound to crack extensions between 0.2 mm and the maximum crack extension from the test data, as shown in Figure 4.12.

The R-curve equation form was:

$$J = m + l(\Delta a)^X \tag{4.7}$$

where m, l and x are constants.

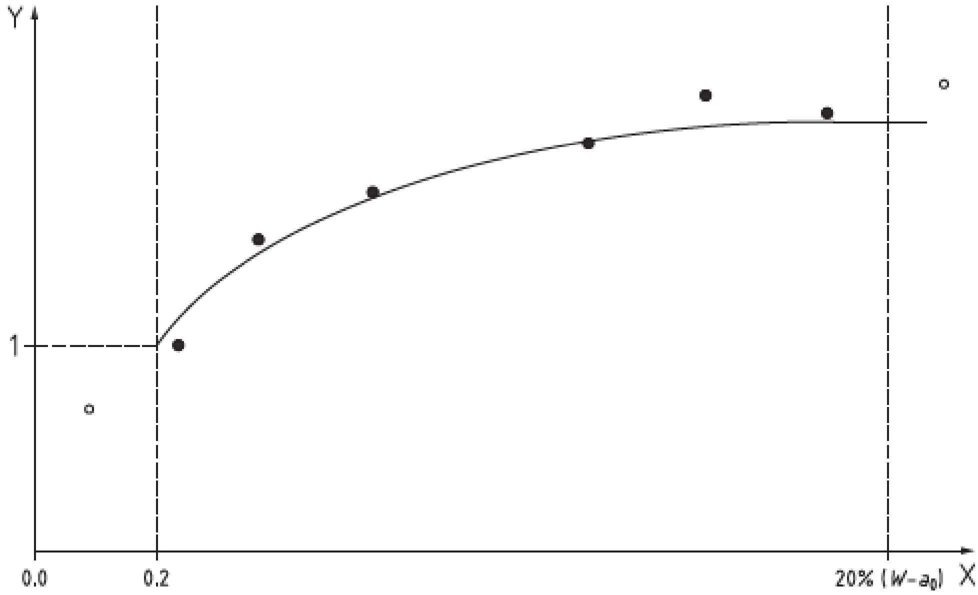


**Key**

______ Fitted R-curve, extrapolated to 0.2 mm crack extension to determine $J$0.2 or $\delta$ 0.2

1 Initiation value of fracture toughness, $J$0.2 or $\delta$ 0.2

○ Data with $\Delta a$ < 0.2 mm or $\Delta a$ > 0.2 × ($W$ - $a$0) mm: excluded from curve fit but plotted

● Data used in fitting the R-curve

X $\Delta a$ (mm)

Y CTOD, $J$

Figure 4.12 Fitting the R-curve to the SENT crack extension data

# CHAPTER 5

# RESULTS AND DISCUSSION

## 5.1 Background

This chapter presents the experimental results, including mechanical characterization and microstructural analysis of specimens. Fracture toughness results of as-received rolled plate and additively manufactured plates are also presented.

## 5.2 Integrity Assessment of the Additively Manufactured Beads

### 5.2.1 Appearance and parts characterization

Top, side, and front views of the wire arc additively manufactured sample with plates of Grade 2509 SDSS is shown in Figure 5.1, displaying the added beads direction and the final height which was approximately 30 mm.

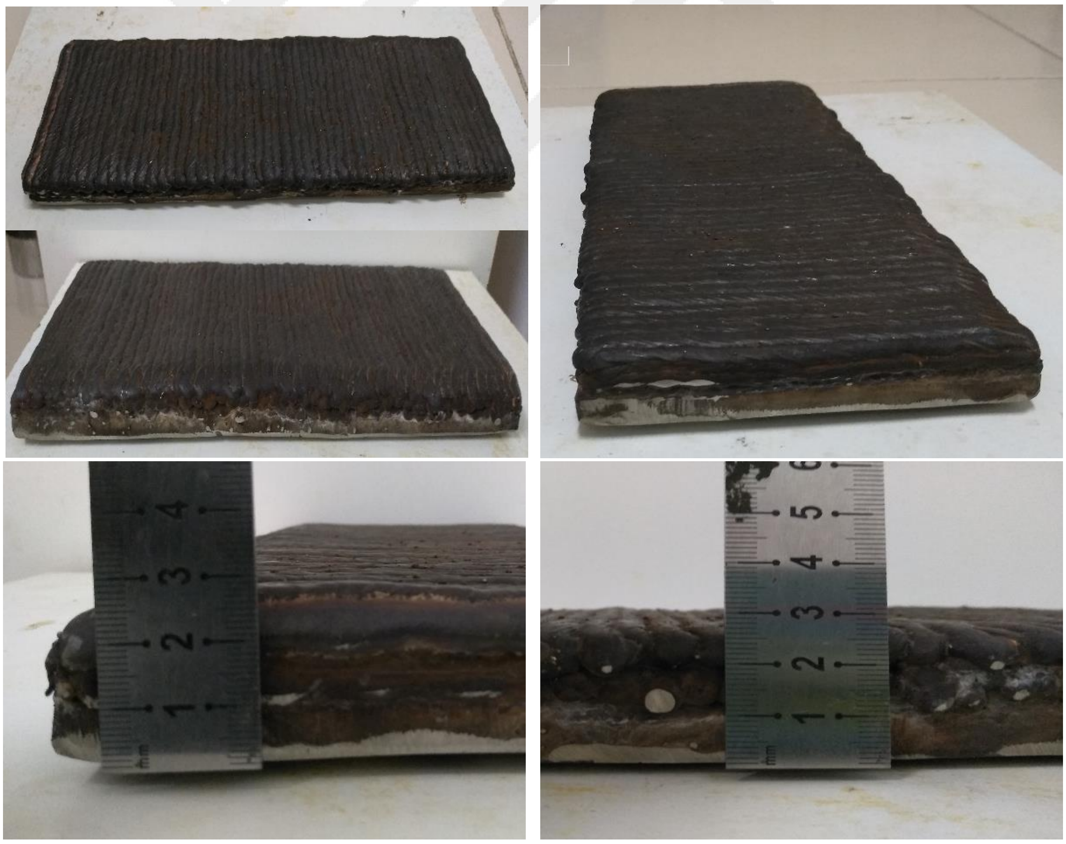

Figure 5.1 Additively manufactured plates of Grade 2509

### 5.2.2 Macroscopic characterization

A sample from transverse side of WAAM’d plate Grade 2509 , as shown in Figure 5.2, was taken for macroscopic examination. The macro-image of the sample shows the layers of manufactured part. The layer bands are in a concave shape and the thickness of the layers varies between 2 mm to 3 mm.

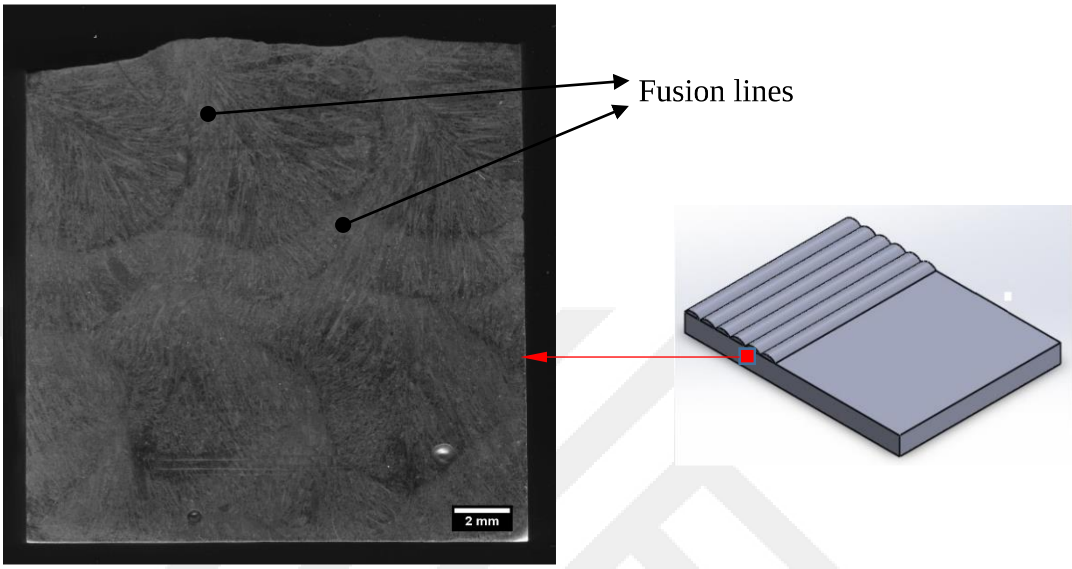


Figure 5.2 Macro-image of the cross-section of the additively manufactured sample of Grade 2509

### 5.2.3 Radiographic Examination

After visual inspection, the top and side surface of additively manufactured part was machined as shown in Figure 5.3-a, and X-ray radiographic examination was done aaccording to ASTM E1742 [76], and radiographs of Figure 5.3-b were evaluated as per the requirements and definitions in ASME BPV Code Section IX [77]. The quality level employed for radiography was 2 % (2-2T using hole type IQI).

The additively manufactured part was free of cracks and no lack of fusion or volumetric discontinuities were detected.

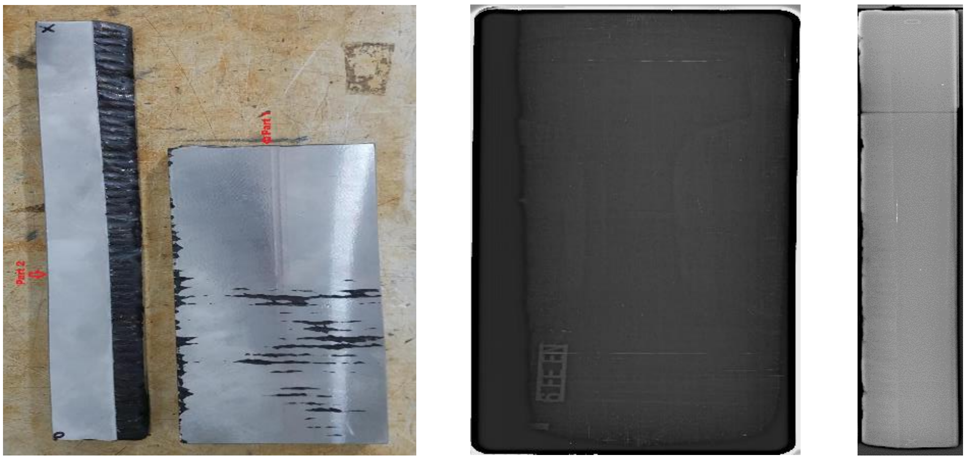

(a) (b)

Figure 5.3 X-ray films

## 5.3 Microstructure Characterization

### 5.3.1 As-Received Product Forms

As-received (Grade 2507) super duplex stainless steel rolled plate has elongated ferrite and austenite grains in the rolling direction. An optical micrograph of this material is shown in Figure 5.4. The dark phase is ferrite and the bright phase is austenite in the wrought microstructure.

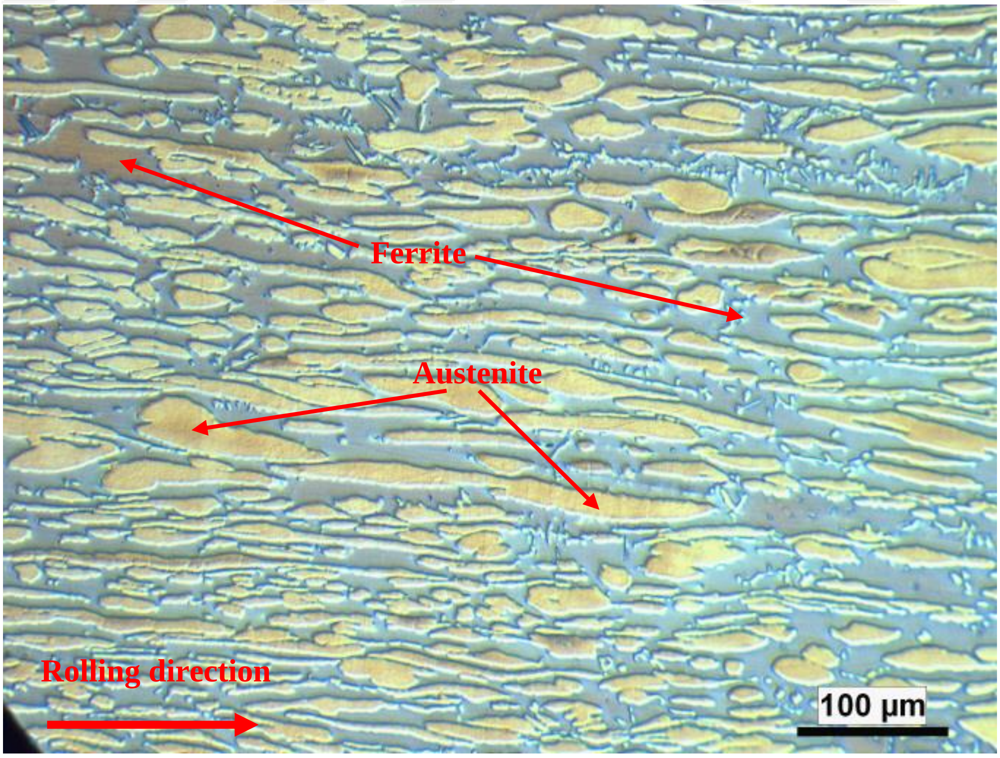


Figure 5.4 Microstructure of As-received SDSS Grade 2507 (100X)

### 5.3.2 WAAM deposited beads

For microstructural examination, four samples were taken from the side surface of deposited beads of Grade 2509 SDSS plates, two from fusion line between beads, one above the fusion line (weld metal) and one below the fusion line (overlapped heat affected zone (OHAZ)) as shown in Figure 5.5.

The revealed microstructures of various positions in the additively manufactured beads are shown in Figure 5.6 to Figure 5.9. The fusion line1 and 2 microstructures are illustrated in Figure 5.6 and Figure 5.7 respectively. The microstructure contains a mixture of primary and secondary austenite.

Figure 5.8 shows the microstructure of the lower fusion line where Widmanstätten austenite formed because of the reheating of the underlying layer. The secondary austenite ($\gamma_2$) is formed from the metastable ferrite at a lower temperature. Widmanstätten and intergranular austenite become finer at the top layer, upper fusion line, due to a higher cooling rate, as shown in Figure 5.9. The high cooling rate of the top layer is caused by convection and radiation without any further heat accumulation.

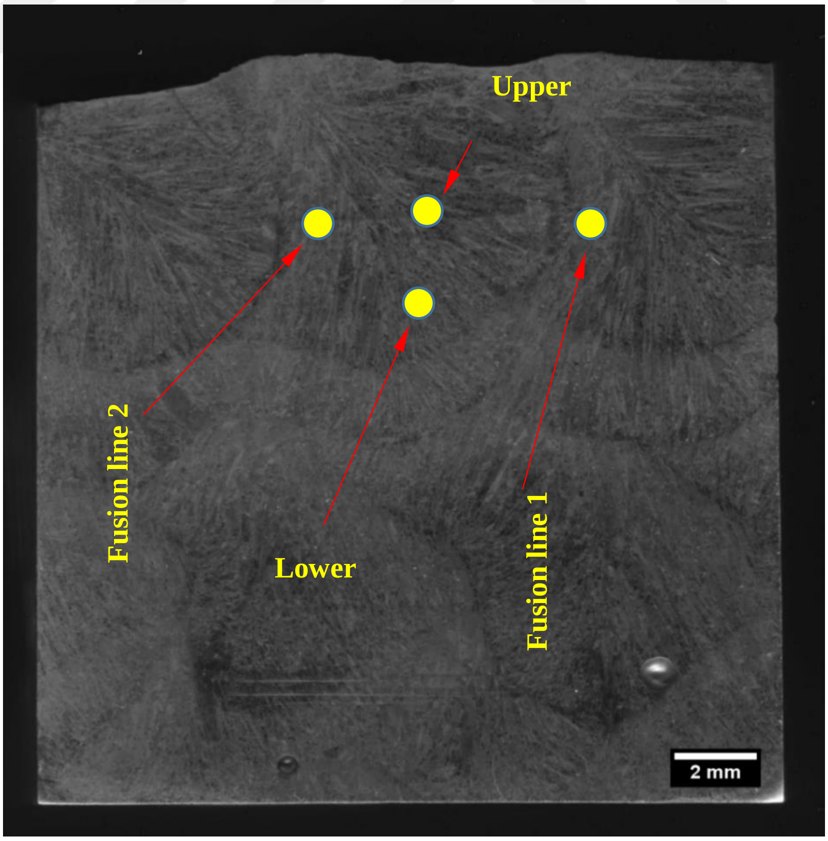


Figure 5.5 Microstructural examination points

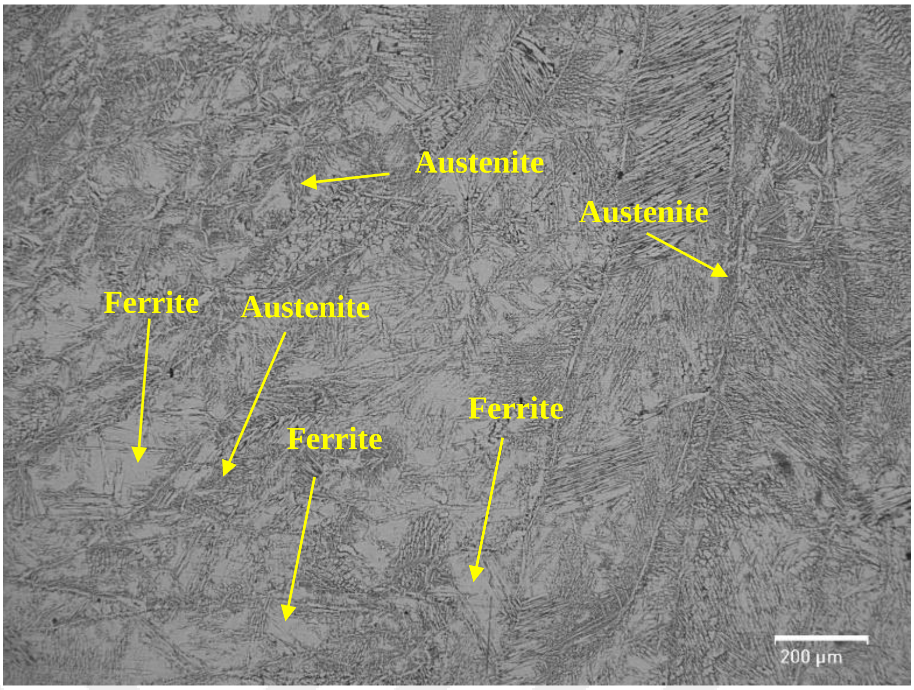


(a)

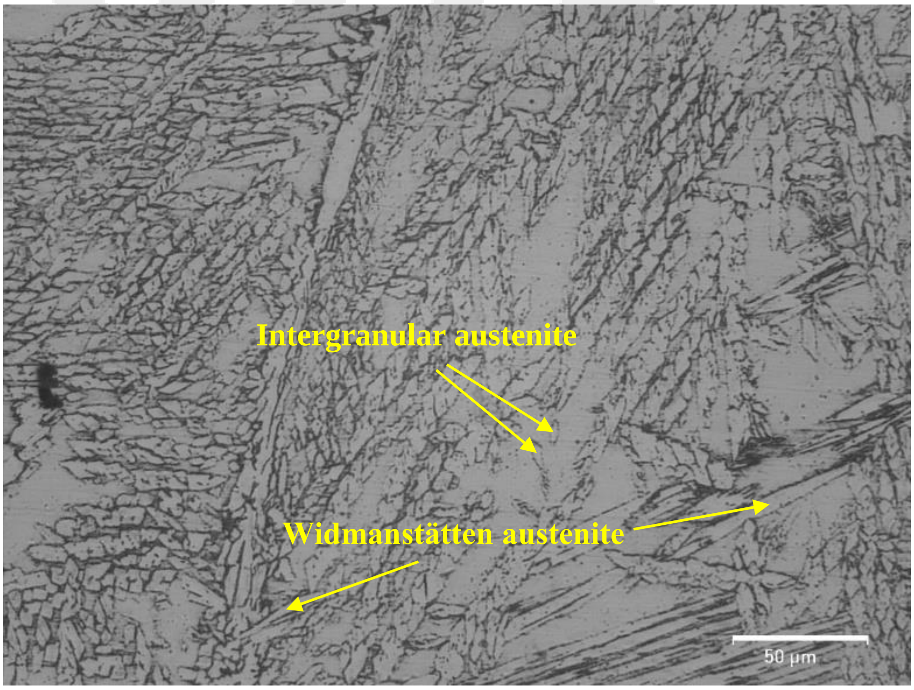


(b)

Figure 5.6 Microstructures of fusion line 1, (a) 290X magnification and (b) 1160X magnification

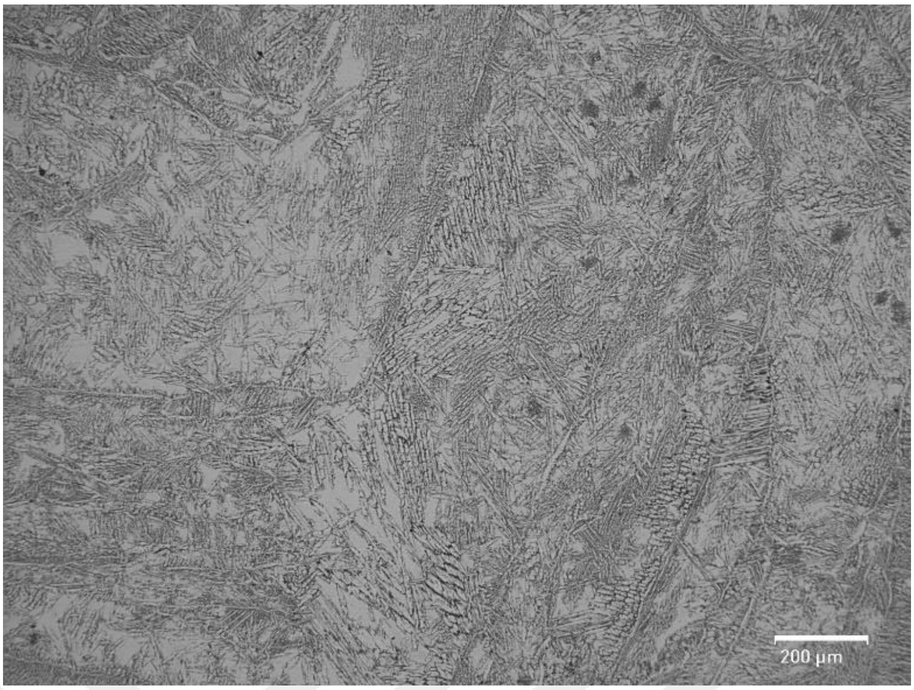


(a)

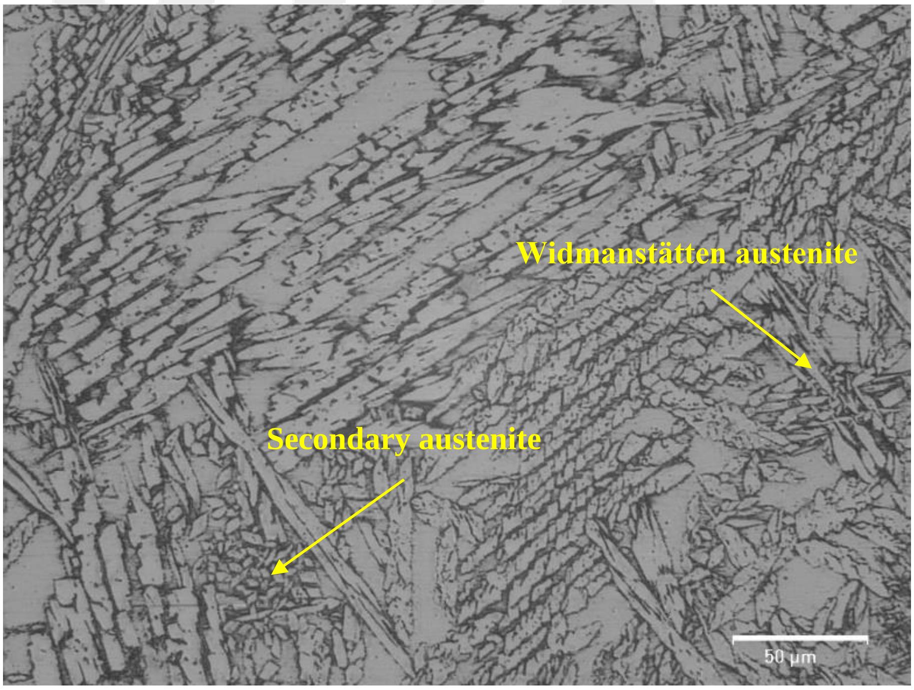


(b)

Figure 5.7 Microstructures of fusion line 2, (a) 290X magnification and (b) 1160X magnification

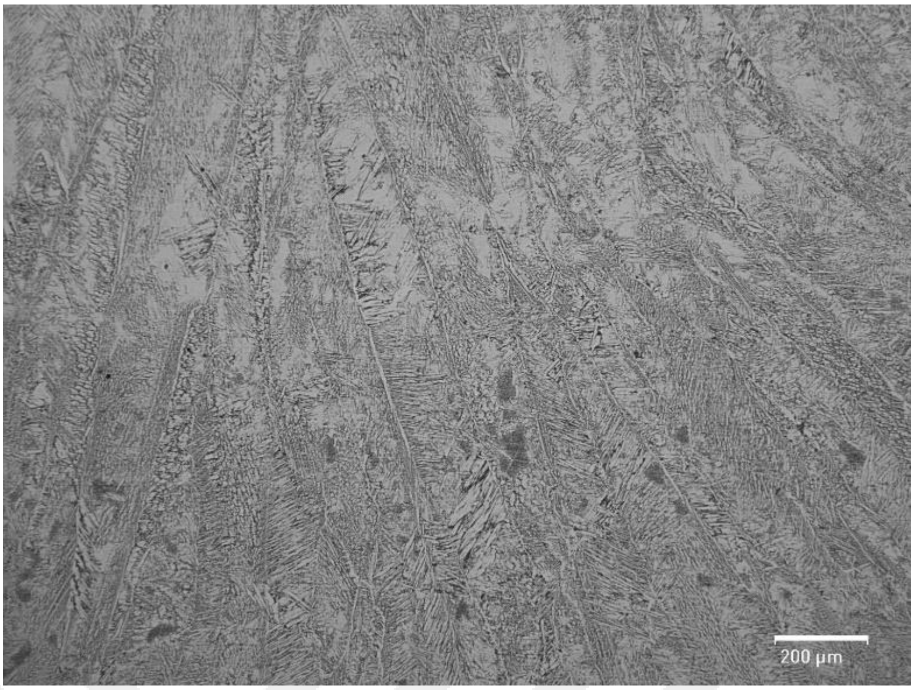


(a)

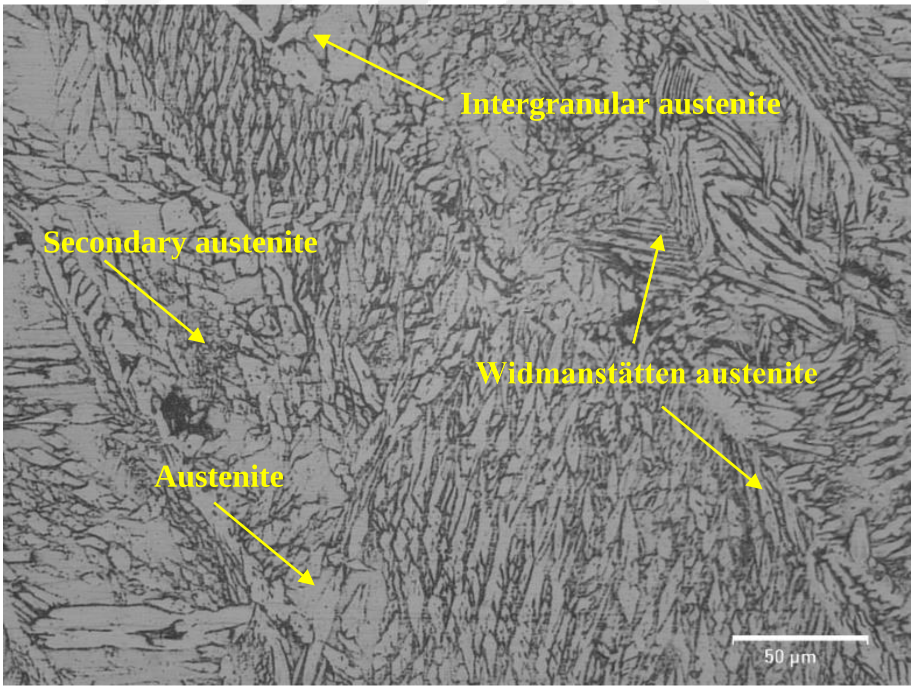


(b)

Figure 5.8 Microstructures of (OHAZ) lower fusion line, (a) 290X magnification and (b) 1160X magnification

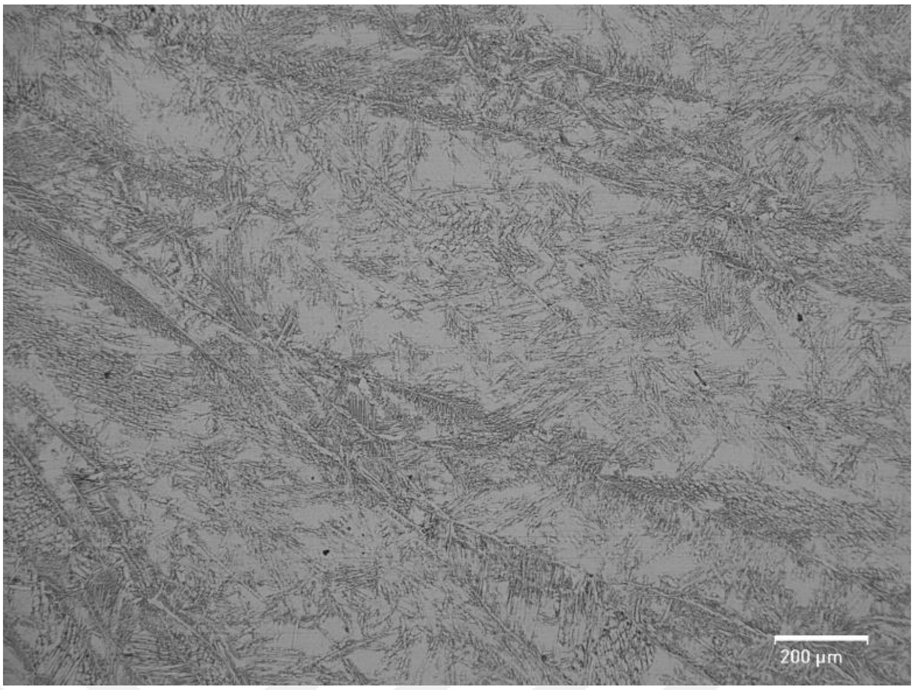


(a)

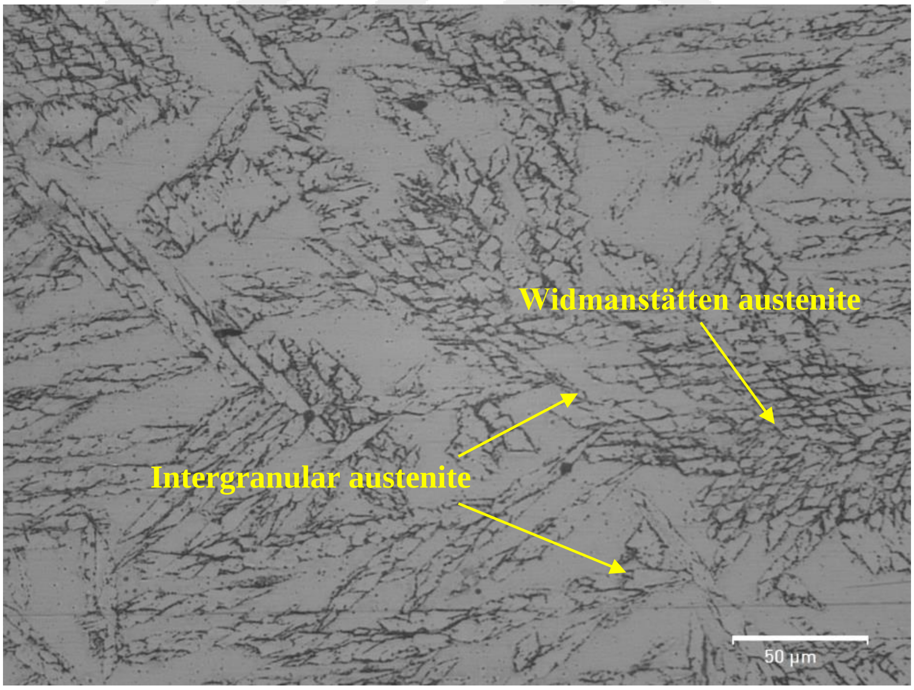


(b)

Figure 5.9 Microstructures of weld metal upper fusion line, (a) 290X magnification and (b) 1160X magnification

The ferrite/austenite ratio is an important microstructural parameter affecting the mechanical properties and corrosion resistance of SDSS. While the SDSS raw material consists of approximately equal proportions of ferrite and austenite, the additively manufactured SDSS can show a significantly wider range. When using wire arc additive manufacturing, the solidification is normally fully ferritic and austenite forms during cooling [84]. Unbalanced ferrite/austenite ratio influences mechanical and corrosion properties, and therefore, investigations are required. Different industry standards set the limit for the ferrite fraction in base metal, heat affected zone, and weld metal of DSS welds. For instance, API TR 938-C stated that ferrite content should be 30–65% for base metal, 40–65% for HAZ, and 25–60% for the weld zone [46], whereas NACE MR0175/ISO 15156-1 states that ferrite content in the weld metal should be in the range of 30% to 70% volume fraction [85]. Different approaches such as point counting (PC) and image analysis (IA) can be used to measure ferrite/austenite ratio. IA is a quick method but demands high quality microstructural images and computer software packages [84, 86, 87]. The microstructural images of the samples, which were taken from places shown in Figure 5.5, were chosen to determine the ferrite/austenite ratio of the WAAM using image analysis approach. The ferrite/austenite ratio was calculated using ImageJ 1.5j8 image analysis software [83] and the results are shown in Figure 5.10, Figure 5.11, Figure 5.12 and Figure 5.13.

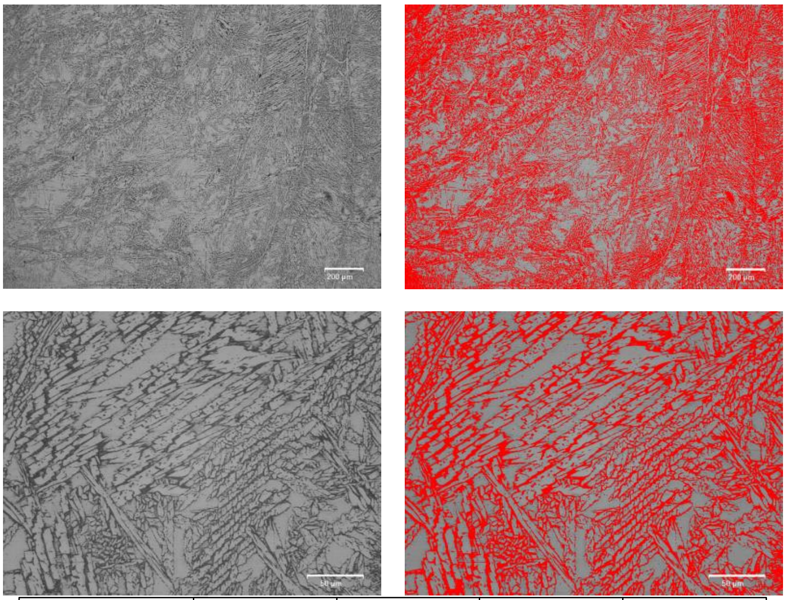

| Measurement | Austenite 290X | Austenite 1160X | Austenite Average | Ferrite |
|---|---|---|---|---|
| Area % | 40.71 % | 33.46 % | 37.09 % | 62.91 % |

Figure 5.10 Ferrite/austenite ratio at fusion line 1

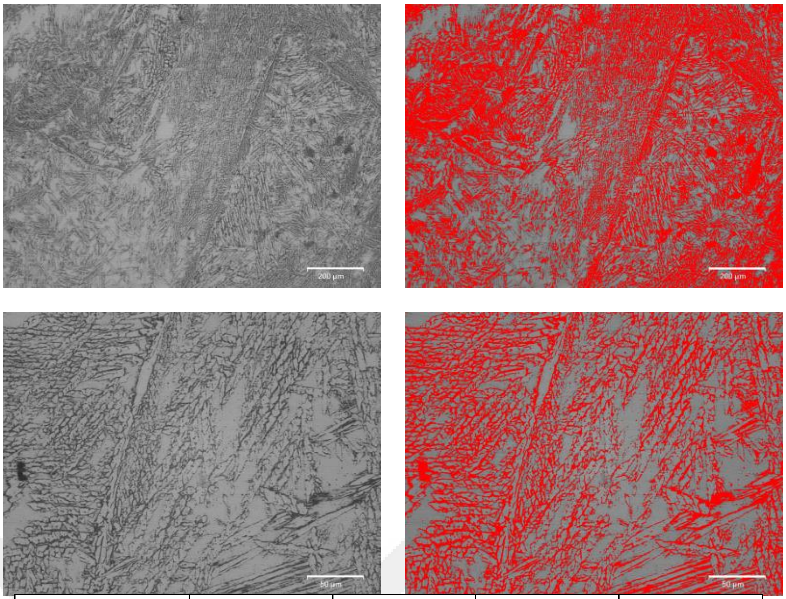

| Measurement | Austenite 290X | Austenite 1160X | Austenite Average | Ferrite |
|---|---|---|---|---|
| Area % | 43.19 % | 29.68 % | 36.44 % | 63.56 % |

Figure 5.11 Ferrite/austenite ratio at fusion line 2

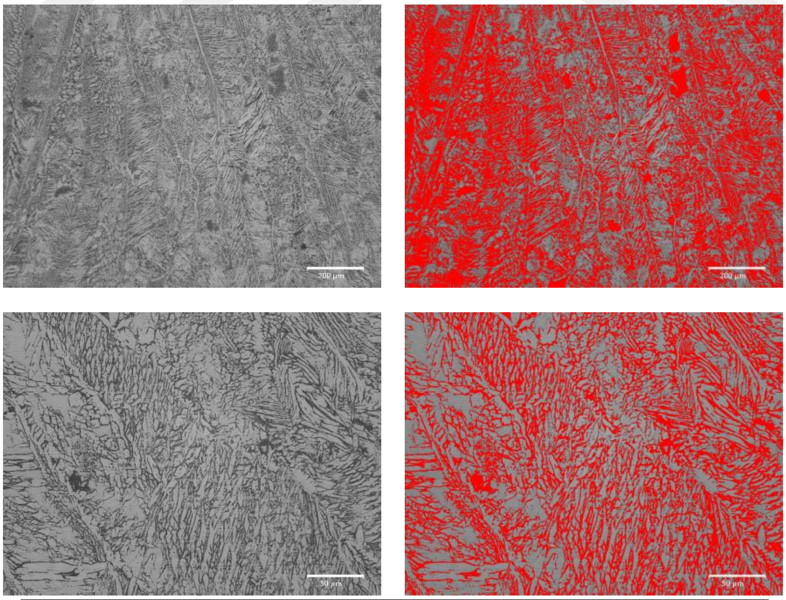

| Measurement | Austenite 290X | Austenite 1160X | Austenite Average | Ferrite |
|---|---|---|---|---|
| Area % | 46.05 % | 34.69 % | 40.37 % | 59.63 % |

Figure 5.12 Ferrite/austenite at OHAZ.

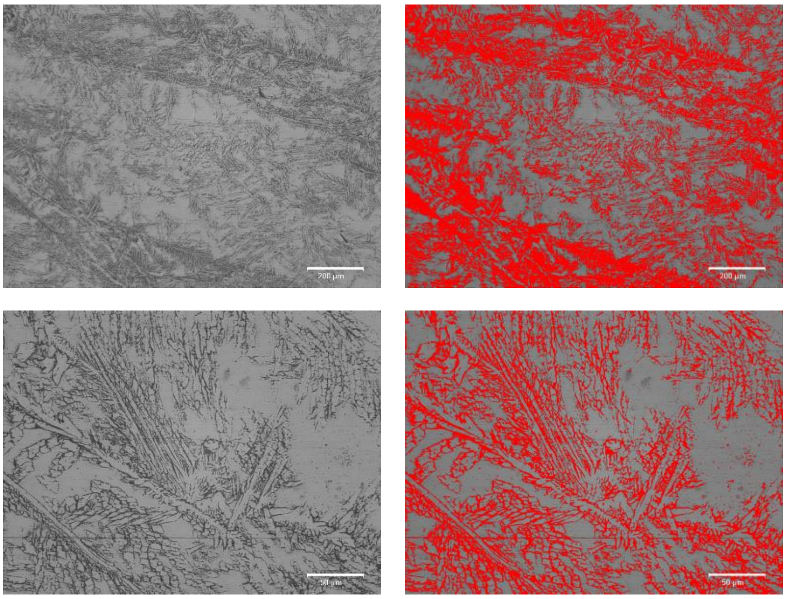

| Measurement | Austenite 290X | Austenite 1160X | Austenite Average | Ferrite |
|---|---|---|---|---|
| Area % | 37.49 % | 25.54 % | 31.52 % | 68.48 % |

Figure 5.13 Ferrite/austenite weld metal.

As stated previously, during additive manufacturing, the increase in temperature causes a significant change in the microstructure of the duplex stainless steel in terms of the volume fraction and the morphology of the ferrite and austenite phases. These microstructural changes, expectedly, changes the mechanical properties. As shown in Figure 5.10 and Figure 5.11, the ferrite fraction in two different fusion lines was 62.91% and 63.56% with an average of 63.2%, whereas Figure 5.12 and Figure 5.13 show that the ferrite percentage in the upper and lower fusion lines were 68.48% and 59.63%. The average ferrite percentage around the fusion line is 63.65%. Although the average result is acceptable according to NACE MR0175/ISO 15156-1 [85], the ferrite percentage still remains high and will probably affect the mechanical properties negatively. Maintaining a proper ferrite / austenite phase balance is necessary to maintain the acceptable toughness and corrosion resistance of the beads.

## 5.4 Mechanical Characterization

### 5.4.1 Tensile Test

Five specimens were extracted from the received plate of SDSS grade 2507 and one sample was sectioned from the additively manufactured block of SDSS grade 2509. Table 5.1 contains the tensile properties of examined samples and tensile properties from 2507 SDSS data sheet [88]. Although the present microstructure of WAAM'd specimens is different from the wrought material, the mechanical properties such as UTS and elongations are comparable, and similar to the results of others in the literature [75, 88]. Figure 5.14 shows the stress-strain curves of as-received super duplex stainless steel plate Grade 2507 and WAAM'd plate made with Grade 2509 super duplex stainless steel filler wire. Figure 5.15 shows fractured samples after tension tests.

Table 5.1 Mechanical properties of Grade 2507 and Grade 2509 super duplex stainless steel.

| Sample | Ultimate Tensile Strength (MPa) | Yield Strength (MPa) | Modulus of Elasticity (GPa) | Elongation (%) |
|---|---|---|---|---|
| Grade 2507 as received rolled Plate | 836 ± 7 | 570 ± 10 | 193 ± 5 | 39.16 ± 3 |
| WAAM'd plate made with Grade 2509 | 845 | 565 | 196 | 45.36 |
| Grade 2507 plate Data sheet [88] | 800-1000 | >550 | | |
| Grade 2509 filler wire Data sheet [75] | 832 | 659 | | 30.00 |

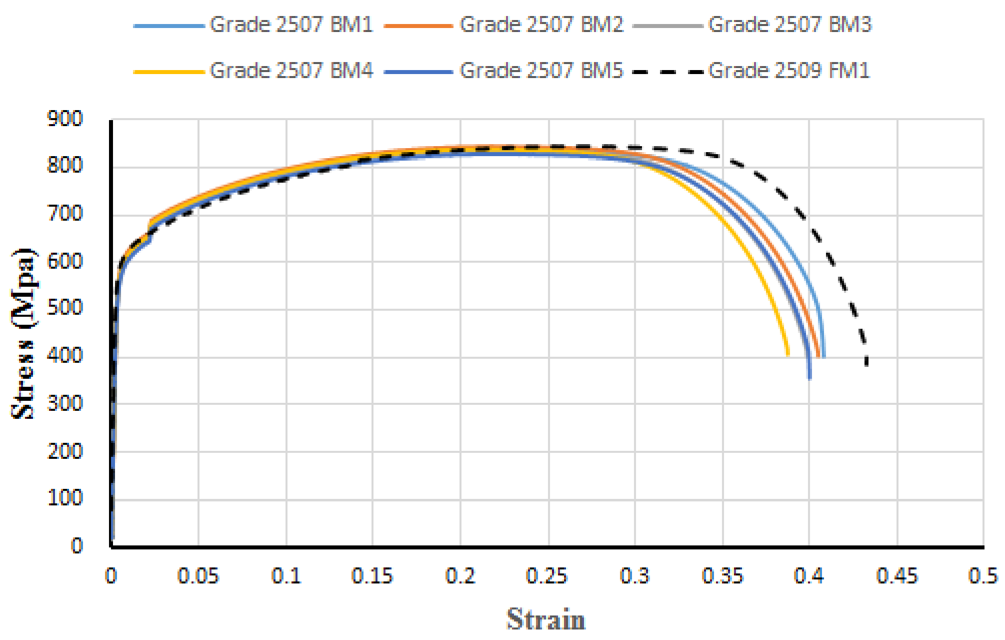


Figure 5.14 Stress-Strain curves of Grade 2507 and Grade 2509 SDSS samples

(a) (b)

Figure 5.15 Specimens (a) before and (b) after the tensile tests.

### 5.4.2 Hardness Test

Vickers hardness indentations were made around the fusion line as shown in Figure 5.16. Maximum hardness value was 325 HV for the WAAM part of Grade 2509 at the fusion lines. A microhardness map is also shown in Figure 5.17. According to SANDVIK data sheet, the hardness of SDSS Grade 2507 is less than 300 HV [88]. The hardness of additively manufactured duplex stainless steel is often higher than base material due to the strain induced by the thermal cycle. The increase in hardness is clear in fusion line between beads.

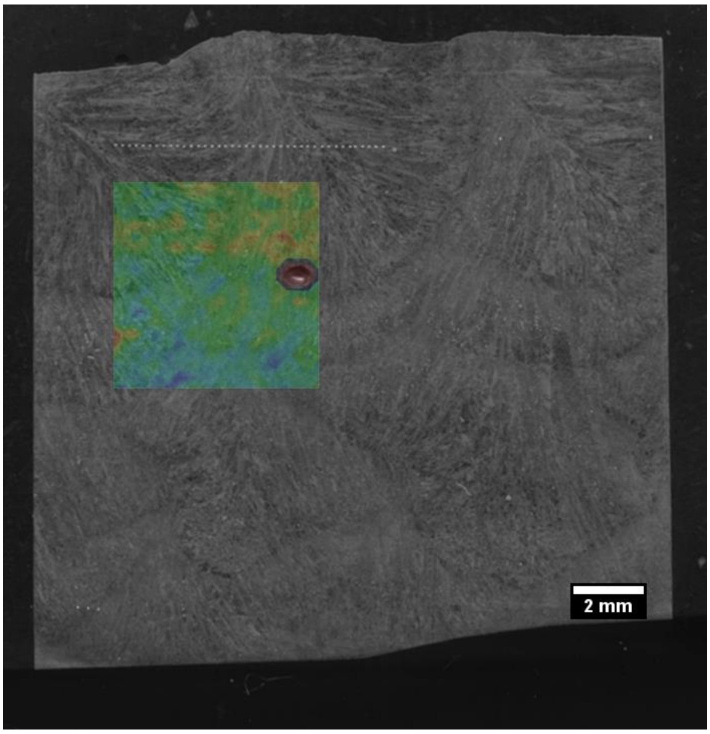


Figure 5.16 Hardness investigation area, WAAM'd Grade 2509

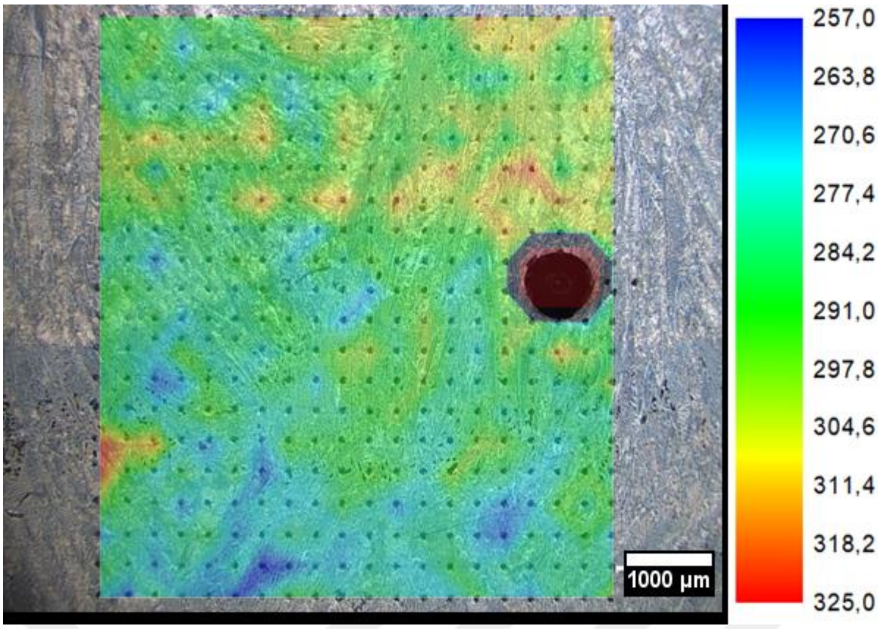


Figure 5.17 Micro-hardness map.

### 5.5 Fracture Toughness Testing

The fracture toughness tests were conducted on eighteen specimens, six specimens for the as-received SDSS plate Grade 2507 characterization and six specimens for the WAAM'd DSS Grade 2209 characterization and six specimens for the WAAM'd SDSS Grade 2509 characterization. The tests were conducted at a temperature of -10°C. Figure 5.18 shows the images of some samples before and after test. The specimens were fatigue pre-cracked at room temperature within the limits of ISO 12135 standard [61]. The pre-crack length was chosen to be 1.5 mm.

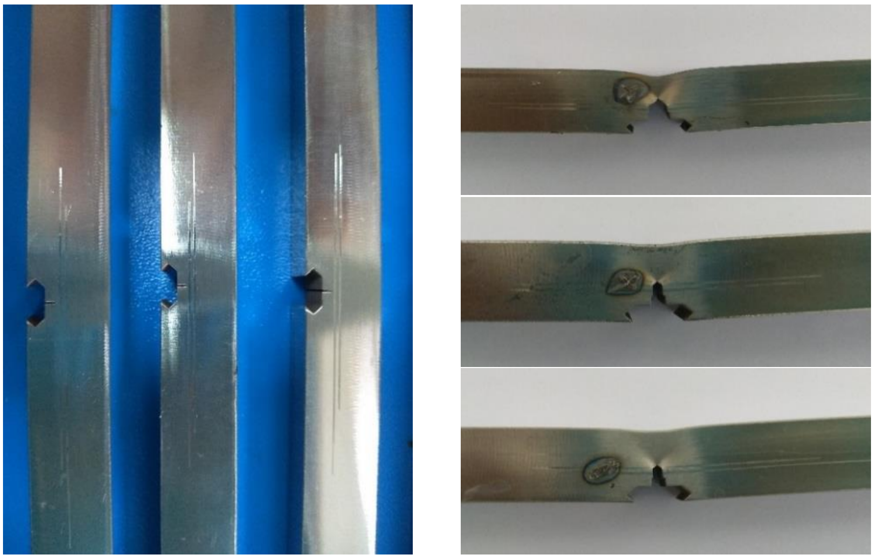

(a) (b)

Figure 5.18 Fracture toughness samples (a) before and (b) after the tests.

For identification and measurement of crack length, heat tinting was performed on the specimens by heating them up to 300°C. Then they were quenched in a bath of liquid nitrogen (-196°C) before they were broken. Due to the brittle behavior of the quenched samples they were broken without any further plastic fracture behavior. After that, high-resolution images of each sample were taken. Then, nine reference measurements points were plotted on each image as indicated in Figure 5.19.

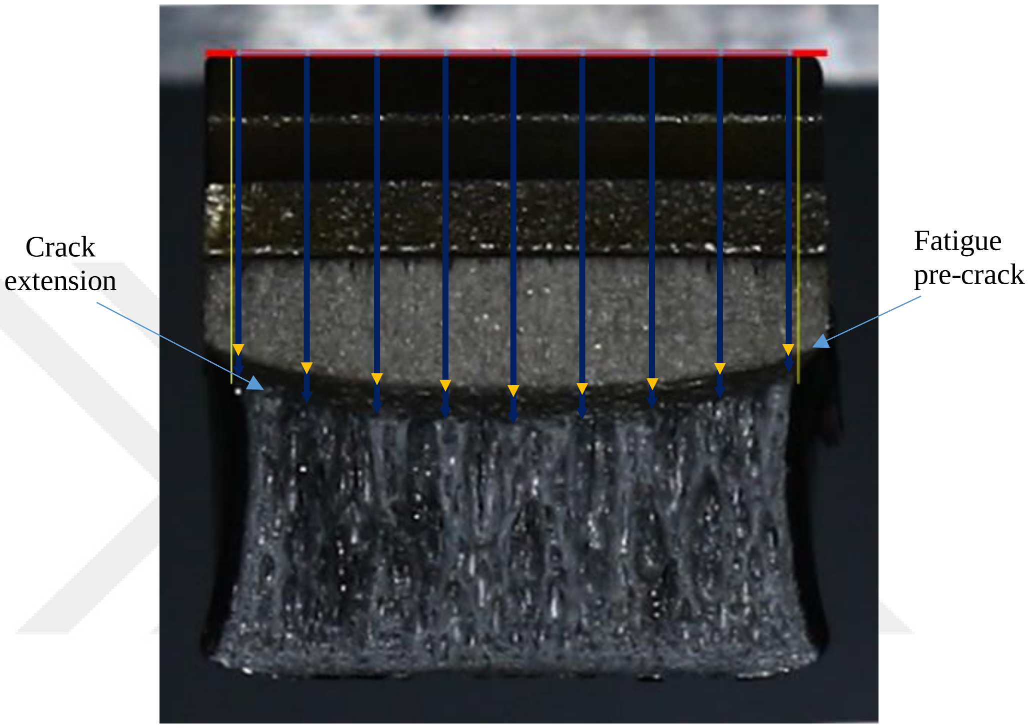


Figure 5.19 Measurements points

Fracture toughness determination using J-integral vs. crack growth resistance (J-R) curve is a useful tool for the evaluation of the structural integrity of a material when defects are present [54]. A typical J-R curve is shown in Figure 5.20. From it, the material fracture toughness at the initiation of stable crack growth (Ji) and at maximum crack extension (Jc) can be derived. According to the BS 8571 standard [62], the data located in the red zone in Figure 5.20 is the qualified data. The dashed lines parallel to the Y-axis (J-integral) are the boundaries of the qualified data region which intersects the x-axis (Δa) at 0.2 and 0.2 ($W$-$a_0$) mm, respectively.

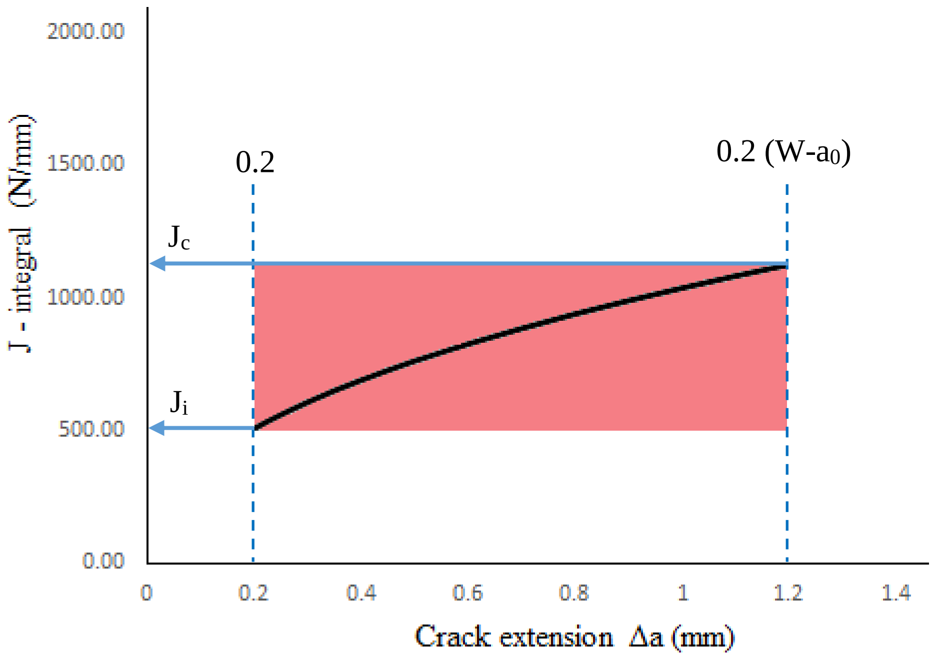


Figure 5.20 Typical J-R curve

To perform the analysis of all samples a Matlab© [89] script is written to automatically determine the relevant values from the graph and calculate the crack extension and J value. The Matlab© script was included in Appendice A.

### 5.5.1 Fracture Toughness of As-received SDSS Rolled Plate Grade 2507

Typical load-displacement curves and fracture surfaces as obtained from fracture test of as-received SDSS plate Grade 2507 can be seen in Figure 5.21. All fracture surfaces suggest that a stable crack occurred without prior pop-ins. Table 5.2 summarize the crack length measurements ($a_0$, $a_f$ and $\Delta a$). The load-displacement curves, fracture surface and crack length measurements of other samples were included in Appendices B and C.

Table 5.2 Crack length of as-received SDSS plate Grade 2507 sample 1

| Specimen | SDSS Grade 2507 (1) | |
|---|---|---|
| Width (mm) | 12.05 (mm) | |
| Thickness (mm) | 12.06 (mm) | |
| position | $a_0$ | $a_f$ |
| 0.813 | 5.531 | 6.077 |
| 2.124 | 5.760 | 6.535 |
| 3.394 | 5.883 | 6.694 |
| 4.664 | 5.901 | 6.861 |
| 5.934 | 5.927 | 6.974 |
| 7.225 | 5.830 | 6.782 |
| 8.515 | 5.751 | 6.658 |
| 9.765 | 5.663 | 6.685 |
| 11.055 | 5.399 | 5.945 |
| $\mathbf{a_0}$ (mm) | 5.773 | |
| $\mathbf{a_f}$ (mm) | 6.650 | |
| **Δa** (mm) | 0.878 | |

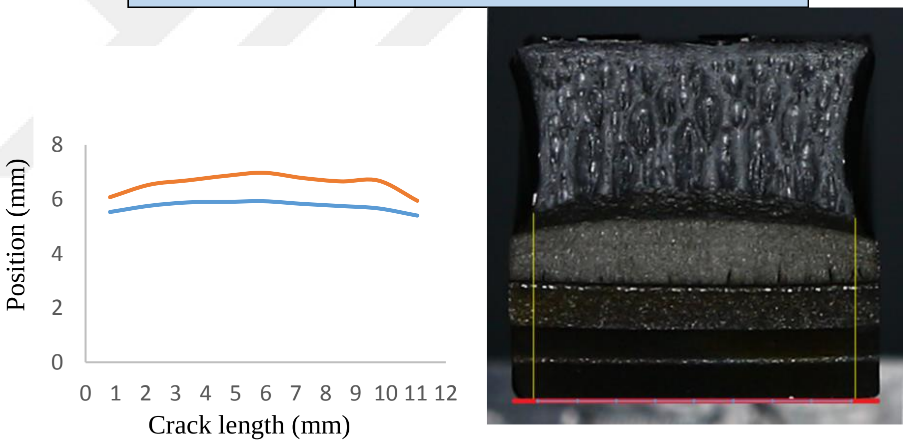


(a)

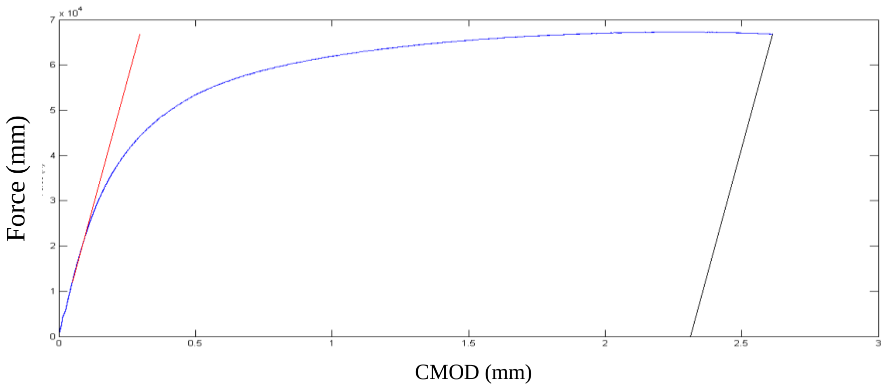


(b)

Figure 5.21. (a) Fracture surface, (b) Load-CMOD of Grade 2507 sample 1

The J-integral values against the crack extension, Δa for as-received SDSS plate Grade 2507 are summarized in Table 5.3 and shown in Figure 5.22

Table 5.3 J-integral values of the as-received SDSS plate Grade 2507

| **Specimen No.** | **J (N/mm)** | **Δa (mm)** |
|---|---|---|
| **Specimen 1** | 1558.00 | 0.8775 |
| **Specimen 2** | 1271.00 | 0.5631 |
| **Specimen 3** | 1190.60 | 0.5064 |
| **Specimen 4** | 1114.60 | 0.5023 |
| **Specimen 5** | 1058.30 | 0.4577 |
| **Specimen 6** | 940.03 | 0.4463 |

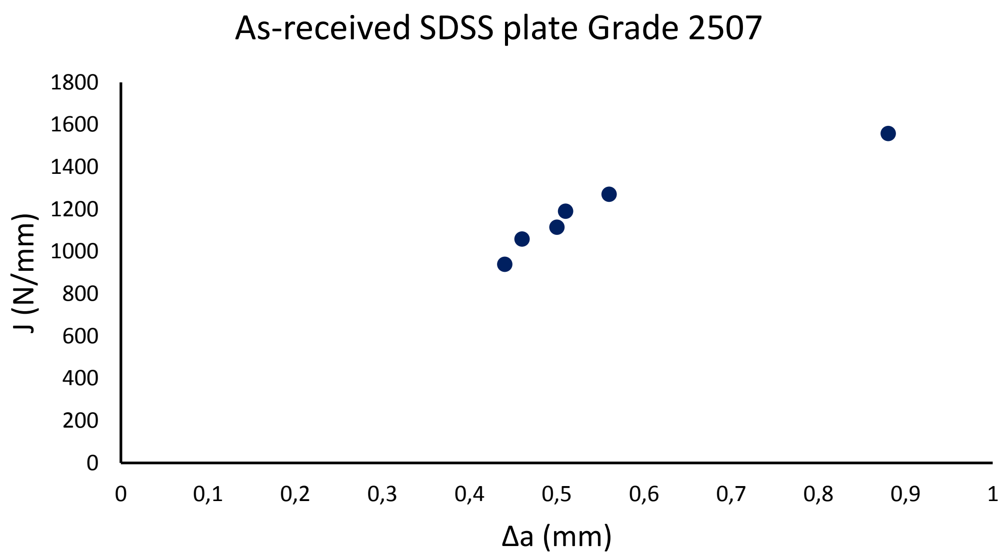


Figure 5.22 J-integral vs crack extension curve for as-received SDSS plate Grade 2507

### 5.5.2 Fracture Toughness of WAAM'd DSS Grade 2209 Plate

Typical load-displacement curves and fracture surfaces as obtained from fracture test of WAAM'd DSS Grade 2209 plate can be seen in Figure 5.23. All fracture surfaces suggest that a stable crack occurred without prior pop-ins. Table 5.4 summarize the crack length measurements ($a_0$, $a_f$ and $\Delta a$). The load-displacement curves, fracture surface and crack length measurements of other samples were included in Appendices B and C.

Table 5.4 Crack length of WAAM'd DSS Grade 2209 plate sample 1

| Specimen | DSS Grade 2209 (1) | |
|---|---|---|
| Width (mm) | 12.03 (mm) | |
| Thickness (mm) | 12.08 (mm) | |
| position | $a_0$ | $a_f$ |
| 0.697 | 5.600 | 6.346 |
| 2.006 | 5.875 | 6.993 |
| 3.296 | 6.032 | 7.307 |
| 4.606 | 6.149 | 7.444 |
| 5.935 | 6.208 | 7.483 |
| 7.224 | 6.169 | 7.326 |
| 8.553 | 6.110 | 7.228 |
| 9.843 | 6.032 | 6.875 |
| 11.133 | 5.777 | 6.542 |
| **$a_0$** (mm) | 6.033 | |
| **$a_f$** (mm) | 7.138 | |
| **$\Delta$a** (mm) | 1.105 | |

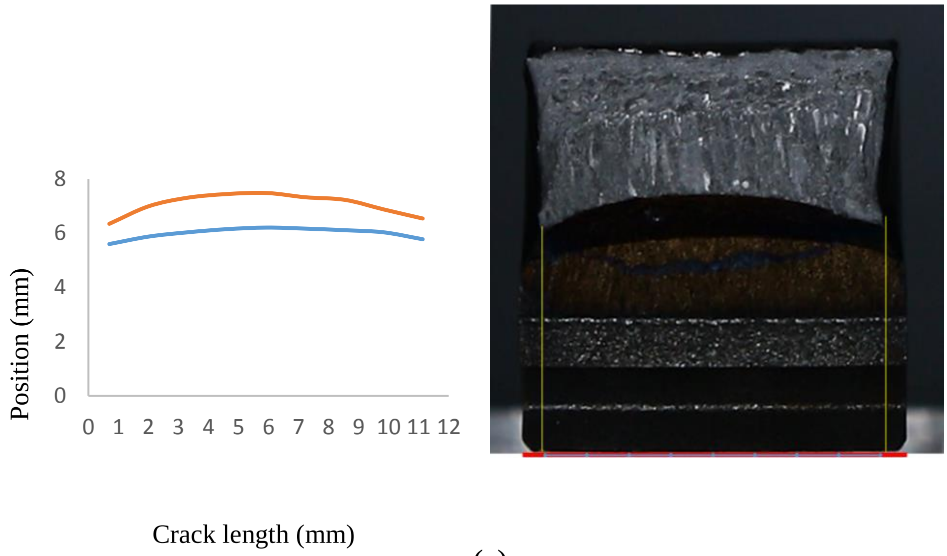


(a)

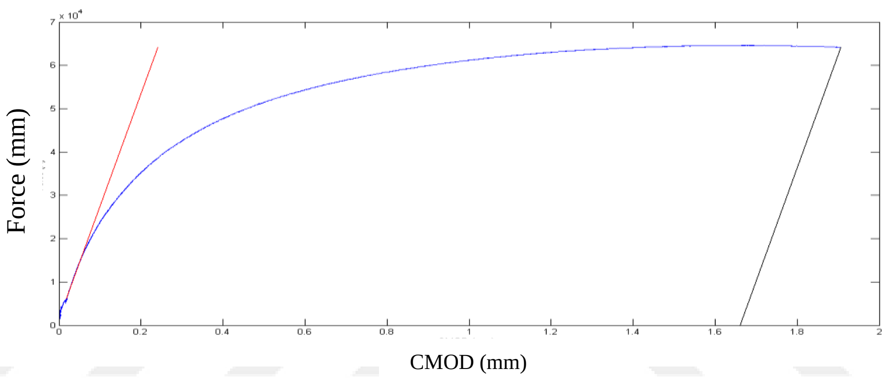


(b)

Figure 5.23. (a) Fracture surface, (b) Load-CMOD of Grade 2209 sample 1

The J-integral values against the crack extension, Δa for WAAM'd DSS Grade 2209 plate are summarized in Table 5.5Table 5.3 and shown in Figure 5.24.

Table 5.5 J-integral values of the WAAM'd DSS Grade 2209 plate

| Specimen No. | J (N/mm) | Δa (mm) |
|---|---|---|
| **Specimen 1** | 1091.00 | 1.1046 |
| **Specimen 2** | 879.63 | 0.5917 |
| **Specimen 3** | 803.45 | 0.5879 |
| **Specimen 4** | 694.44 | 0.4619 |
| **Specimen 5** | 681.75 | 0.4318 |
| **Specimen 6** | 593.39 | 0.2565 |

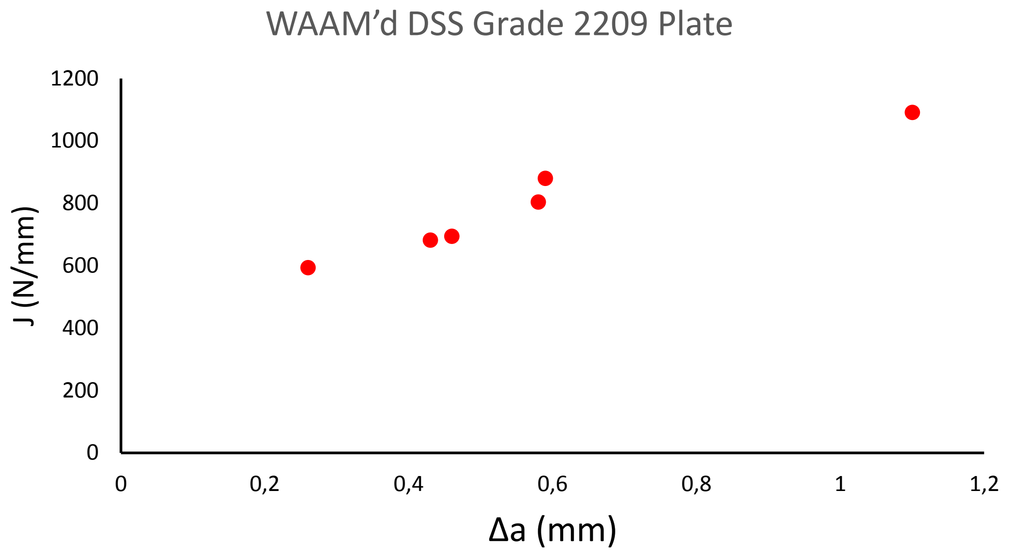


Figure 5.24 J-integral vs crack extension curve for WAAM’d DSS Grade 2209 plate

The J R-curves have been obtained by curve fitting the test data. Normally, a lower-bound curve was used and the R-curve equation is:

$$J = I\,(\Delta a)^{X} \tag{5.1}$$

The fitting parameters I and X for the as-received SDSS plate Grade 2507and WAAM’d DSS Grade 2209 plate are given in Table 5.6. The J value against the crack extension based on fitting parameters were shown in Figure 5.25.

Table 5.6 Fitting parameters of J integral

| Material | $J = I\,(\Delta a)^{X}$ | |
|---|---|---|
| | I | X |
| As-received SDSS plate Grade 2507 | 1749 | 0.65 |
| WAAM’d DSS Grade 2209 plate | 1039 | 0.45 |

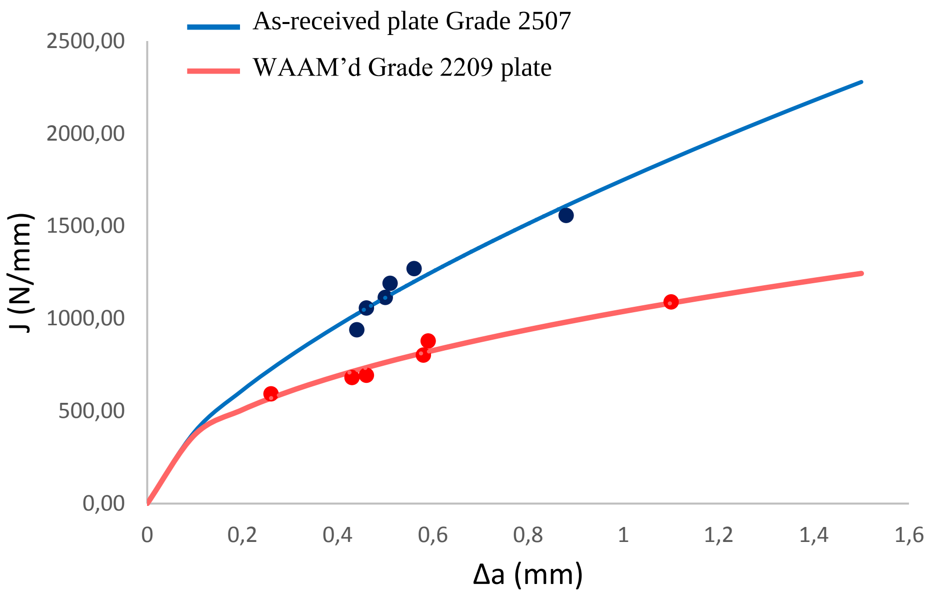


Figure 5.25 J R-curve lower-bound Fitting Parameters

### 5.5.3 Fracture Toughness of WAAM'd SDSS Grade 2509 Plate

For the deposited 2509 Grade SDSS characterization, as mentioned in section 4.6, the study was focused on the overlapping heat affected zones (OHAZ) as depicted in Figure 4.7. The tests were conducted but the results were very low so that a resistance curve for specimens taken out from additively manufactured part of Grade 2509 SDSS could not be generated. Alternatively, their fracture toughness were calculated roughly using load vs. CMOD curves at weld metal (see Figure 5.26) and OHAZ (see Figure 5.27). The technical crack initiation value $a_0$ was determined using a stable crack propagation of $\Delta a$ = 0.2 mm. The results are summarized in Table 5.7.

.

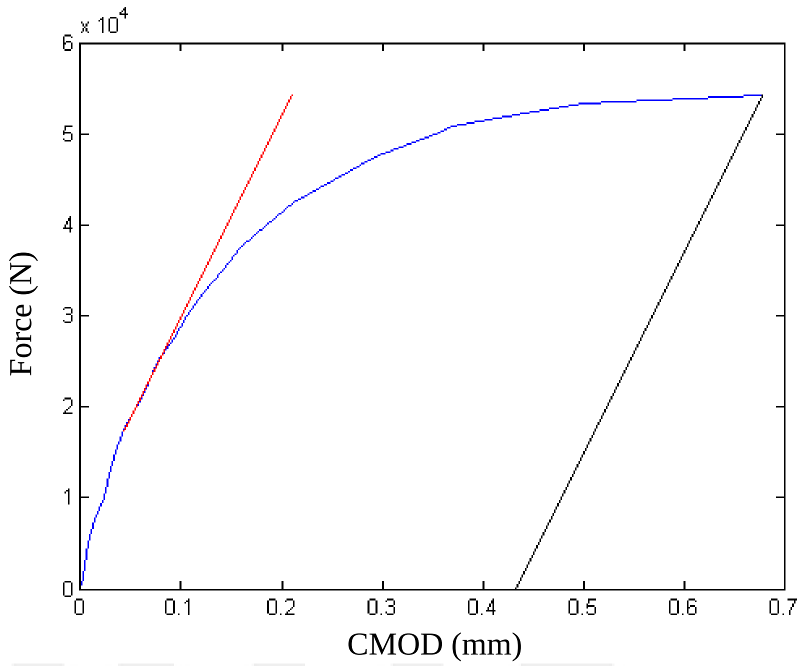


Figure 5.26 Load-CMOD of WAAM’d SDSS Grade 2509 plate at the weld metal.

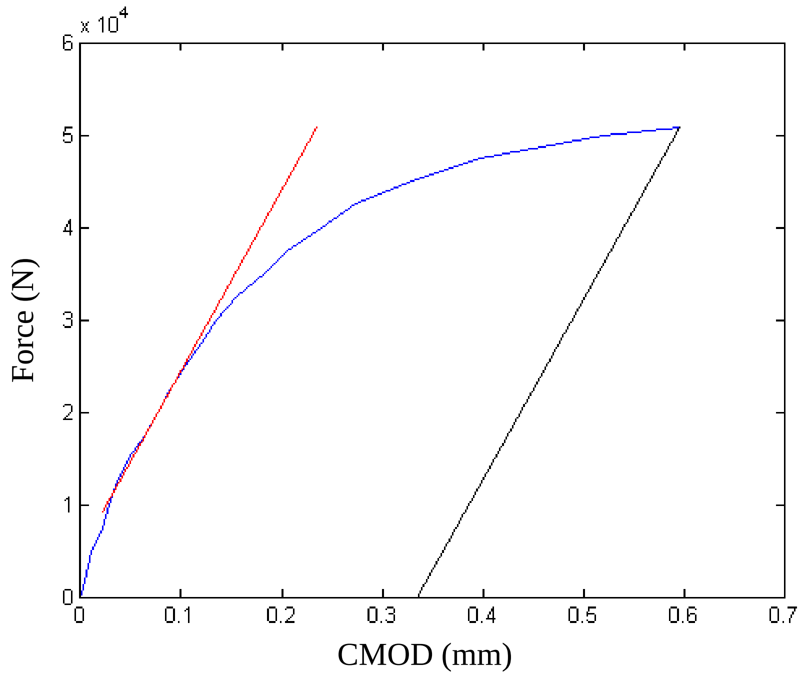


Figure 5.27 Load-CMOD of WAAM’d SDSS Grade 2509 plate at OHAZ.

Table 5.7 J-integral values of WAAM'd SDSS Grade 2509 plate.

| Test location Grade 2509 | P (N) | Up (N.mm) | $a_0$ (mm) | J (N/mm) |
|---|---|---|---|---|
| **Weld metal** | 54166 | 35735 | 5.7 | 421.14 |
| **OHAZ** | 50833 | 18907 | 5.7 | 240.81 |

The fracture toughness results have demonstrated that there is a disparity between J integral values of As-received plate Grade 2507 and WAAM'd DSS Grade 2209 plate. Based on BS 8571 standard, the initiation fracture toughness value is the value of J at 0.2 mm of crack extension and the maximum value at 0.2(W-a0) from the R-curve fit. Figure 5.28 shows the J-R curves obtained for the investigated As-received plate Grade 2507and WAAM'd SDSS Grade 2209 plate and present the values of Ji and Jc which are also summarized in Table 5.8 .

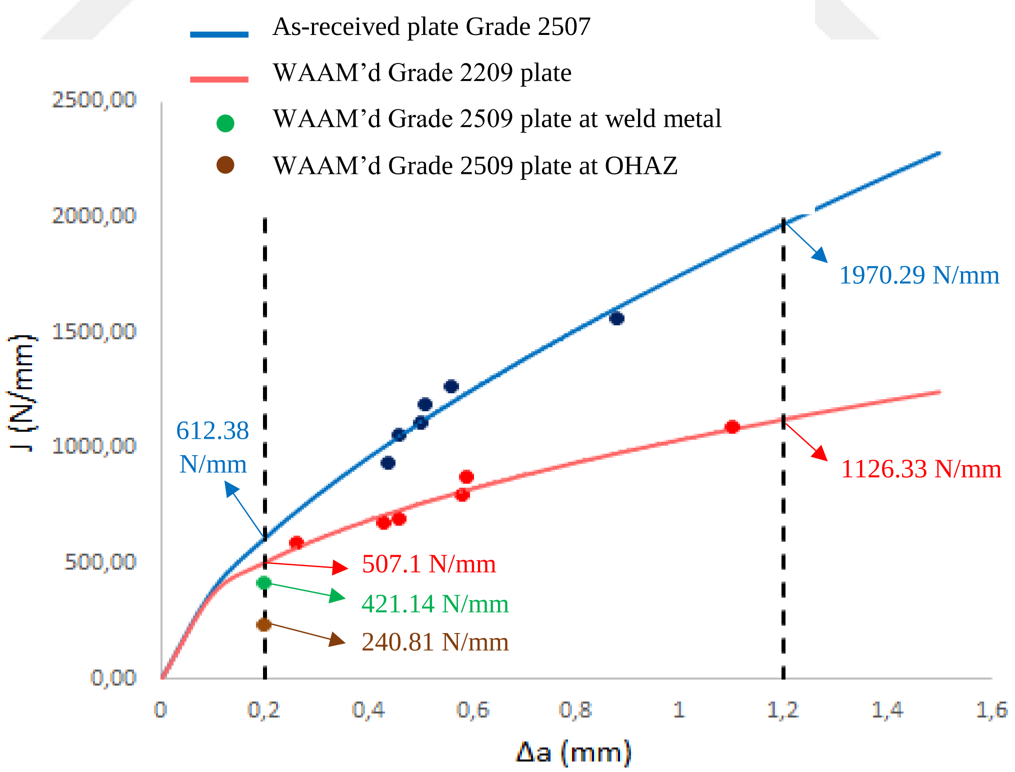


Figure 5.28 J-R curve of different DSS Grades

Table 5.8 J-integral values of different DSS Grades

| Material | Ji (N/mm) | Jc (N/mm) |
|---|---|---|
| As-received rolled plate Grade 2507 | 612.38 | 1970.29 |
| WAAM'd DSS Grade 2209 plate | 507.17 | 1126.33 |
| WAAM'd SDSS Grade 2509 plate at weld metal | 421.14 | --- |
| WAAM'd SDSS Grade 2509 plate at OHAZ | 240.81 | --- |

The Ji values of additively manufactured SDSS Grade 2509 plate at the weld metal and OHAZ also presented as two points. Two results of fracture toughness can be distinguished. On the one hand, 2507 As-received plate and WAAM'd 2209 Grades plate show two J integral values, at crack initiation (Ji = 612.38 N/mm and 507.17 N/mm respectively) and at maximum crack extension (Jc = 1970.29 N/mm and 1126.33 N/mm for 2507 and 2209 Grades respectively). Both DSS grades are characterized by noticeable increase of J values during crack propagation. On the other hand, for WAAM'd SDSS Grade 2509 plate the Ji values at the weld metal and OHAZ were 421.14 N/mm and 240.81 N/mm, respectively.

As-received SDSS plate Grade 2507 specimens have an approximately 17% higher ($J_i$) value than additively manufactured DSS Grade 2209 plate. For the additively manufactured SDSS Grade 2509 plate, the value of ($J_i$) at weld metal was approximately 31% lower than SDSS Grade 2507 and 16 % lower than DSS Grade 2209. As well, the value of ($J_i$) at the OHAZ was approximately 60% lower than SDSS Grade 2507 and 52% lower than DSS Grade 2209. The discrepancy in fracture toughness value could be explained by the fact that both samples had significant anisotropy in terms of distribution and morphologies of the phases, ferrite and austenite. Currently, the reason for a difference in fracture toughness value is an assumption, and further analysis, such as fractography, is required to better understand this behavior.

# CHAPTER 6

# CONCLUSIONS

## 6.1 CONCLUSIONS

In this thesis, cold metal transfer wire arc additive manufacturing was studied to produce rectangular plates out of Grade 2509 and Grade 2209 duplex stainless steel wires. The employed WAAM process parameters were obtained from simulation studies which aimed parameter optimization to minimize the distortion of the plates deposited. Microstructural characterization and conventional tensile and hardness testing of the produced DSS plates were performed. Finally, fracture toughness tests of additively manufactured SDSS were performed at a sub-zero temperature using the single edge notched tension (SENT) specimens. The main conclusions that can be drawn from this study are as follows:

1. It is found that the response surface method, combined with process simulation, can be used to build statistical models to predict the distortion of WAAM products within the working range of process variables and obtain optimum process parameters.

2. The longitudinal and transversal distortions increase with the increase in arc voltage and welding current for any given value of the welding speed. However, this increase in distortion gradually decreases as the welding speed increases.

3. Specific to the CMT WAAM of DSS plates produced in this study, the desirable longitudinal (D1) and transversal (D2) distortions have been found to be 1.17 mm and 0.70 mm corresponding to the input WAAM process variables of 200 A of weld current, 15 V of weld voltage and 10 mm/s of weld speed.

4. The strength of the WAAM parts were comparable to the wrought material. Ultimate tensile strength of samples made out of Grade 2507 and Grade 2509 DSS were determined as 836 MPa and 845 MPa, respectively.

5. Although the ferrite/austenite ratio of the deposited samples varied along the cross section of the deposited samples, the values remained within the range desired from duplex stainless steels. Specifically, the ferrite/austenite ratios determined at fusion line1, fusion line2, upper fusion line and lower fusion line were (62.91/37.09), (63.56/36.44), (59.63/40.37) and (68.48/31.52), respectively.

6. The initiation J (J0.2) values for the as-received rolled plate and WAAM'd plate are 612.38 N/mm and 507.17 N/mm, respectively. For the Grade 2509, the Ji values at the weld metal (deposited during WAAM) were 421.14 N/mm and 240.81 N/mm at the overlapped heat affected zone (OHAZ). Lower fracture toughness is a common weakness of nearly all additive manufacturing processes using raw materials in powder or wire form. It is speculated that the significantly lower fracture toughness values of the WAAM samples should be related with their anisotropy.

## 6.2 SUGGESTIONS FOR FUTURE WORK

Suggestions for future work can be classified into two areas:

1. Modeling and simulation aspect.
    - Extend the simulation work to study the effect of WAAM parameters on the fracture toughness of SDSS.
    - It could be interesting to estimate the J-R curve of additively manufactured SDSS based on simulation.
2. Experimental aspect
    - Detailed fractographic examination of the SENT samples.
    - Inherent aspects of additive manufacturing processes resulting in lower fracture toughness for engineering parts especially for structural applications needs much more attention.
    - Investigation of the impact of post-weld heat treatment on the anisotropic behavior, corrosion and fracture toughness of additively manufactured SDSS.
    - Investigation of the fatigue crack propagation behavior of additively manufactured SDSS.

## REFERENCES


[1] A. Staffanson and P. Ragnartz, “Improving the product development process with additive manufacturing,” , MSc thesis, Mälardalen University, Sweden, 2018.

[2] A. Yadav, A. Ghosh, and A. Kumar, “Thermal transport phenomena in multi-layer deposition using arc welding process,” *3D printing and additive manufacturing,* pp. 15-27, 2019.

[3] S.H. Lee, “Optimization of cold metal transfer-based wire arc additive manufacturing processes using gaussian process regression,” *Metals,* vol. 10, no. 4, p. 461, 2020.

[4] M. Liberini, A. Astarita, G. Campatelli, A. Scippa, F. Montevecchi, G. Venturini, M. Durante, L. Boccarusso, F. Memola, C. Minutolo and A. Squillace, “Selection of optimal process parameters for wire arc additive manufacturing,” *Procedia CIRP,* vol. 62, pp. 470-474, 2017.

[5] C.R. Cunningham, J.M. Flynn, A. Shokrani, V. Dhokia and S.T. Newman, “Invited review article: Strategies and processes for high quality wire arc additive manufacturing,” *Additive Manufacturing,* vol. 22, pp. 672-686, 2018.

[6] B. Wu, Z. Pan, D. Ding, D. Cuiuri, H. Li, J. Xu, and J. Norrish, “A review of the wire arc additive manufacturing of metals: properties, defects and quality improvement,” *Journal of Manufacturing Processes,* vol. 35, pp. 127-139, 2018.

[7] K. Ogawa , “Development and Recent Trends of Duplex Stainless Steel,” *The Japan Welding Engineering Society,* 2015.

[8] B. Jang, I. Moon, M. Lim, S. Kim, S. Kim, J. Lee, H. Park and J. Koh, “Heat Treatment Effect on Super Duplex Stainless Steel UNS S32750 FCA Multipass Welds,” *Journal of Welding and Joining,* vol. 32, no. 2, pp. 48-53, 2014.

[9] X. Zhang, K. Wang, Q. Zhou, J. Ding, S. Ganguly, G. Marzio, D. Yang, X. Xu, P. Dirisu, and S.W. Williams, “Microstructure and mechanical properties of TOP-TIG-wire and arc additive manufactured super duplex stainless steel (ER2594),” *Materials Science and Engineering: A,* vol. 762, p.138097, 2019.

[10] A.O. Humphreys, “The Low Temperature Fracture Behaviour of the Super Duplex Stainless Steel Zeron 100” PhD thesis, University of Birmingham, UK, 1997.

[11] C. Bayley, “Evaluation of the single edge notch tension specimen for quantifying fracture toughness,” Defence Research and Development, Canada, 2015.

[12] K. Davidson and S. Singamneni, “Selective Laser Melting of Duplex Stainless Steel Powders: An Investigation,” *Materials and Manufacturing Processes* , vol. 31, no. 12, pp. 1543-1555, 2016.

[13] F. Hengsbach, P. Koppa, K. Duschik, M.J. Holzweissig, M. Burns, J. Nellesen, W. Tillmann, T. Tröster, K. Hoyer, and M. Schaper, “Duplex stainless steel fabricated by selective laser melting – Microstructural and mechanical properties,” *Materials & Design* , vol. 133, pp. 136-142, 2017.

[14] G. Posch, K. Chladil and H. Chladil, “Material properties of CMT- metal additive manufactured duplex stainless steel blade-like geometries,” *Welding in the World*, vol. 61, no. 5, pp. 873-882, 2017.

[15] M. Eriksson, C. Fredrik, M. Lervåg, C. Sørensen, A. Robertstad, B.M. Brønstad, B. Nyhus, R. Aune, X. Ren and O.M. Akselsen, “Additive manufacture of superduplex stainless steel using WAAM,” in *5th International Conference of Engineering Against Failure (ICEAF-V 2018)*, 2018.

[16] S. Papula, M. Song, A. Pateras, X. Chen, M. Brandt, M. Easton, Y. Yagodzinskyy, I. Virkkunen, and H. Hänninen, “Selective laser melting of duplex stainless steel 2205: effect of post-processing heat treatment on microstructure, mechanical properties, and corrosion resistance,” *Materials* , vol. 12, no. 15, p. 2468, 2019.

[17] F. Hejripour, F. Binesh, M. Hebel, and D.K. Aidun, “Thermal modeling and characterization of wire arc additive manufactured duplex stainless steel,” *Journal of Materials Processing Technology*, vol. 272, pp. 58-71, 2019.

[18] V.A. Hosseini, M. Högström, K. Hurtig, M. Asuncion,V. Bermejo, L. Stridh, and L. Karlsson, “Wire-arc additive manufacturing of a duplex stainless steel: Thermal cycle analysis and microstructure characterization,” *Welding in the World*, vol. 63, no. 4, pp. 975-987, 2019.

[19] J. Stützer, T. Totzauer, B. Wittig, M. Zinke, and S. Jüttner, “GMAW cold wire technology for adjusting the ferrite–austenite ratio of wire and arc additive manufactured duplex stainless steel components,” *Metals*, vol. 9, no. 5, p. 564, 2019.

[20] M. Lervåg, C. Sørensen, A. Robertstad, B.M. Brønstad, B. Nyhus, M. Eriksson, R. Aune, X. Ren, O.M. Akselsen, and I. Bunaziv, “Additive manufacturing with superduplex stainless steel wire by CMT process,” *Metals*, vol. 10, no. 2, p. 272, 2020.

[21] A. Bandyopadhyay, T.P. Gualtieri and S. Bose, “Global Engineering and Additive Manufacturing,” in *Additive Manufacturing*, Taylor & Francis Group, 2016, pp. 1-18.

[22] ADDISPACE team, “State of the Art Additive Manufacturing Technologies: Technologie, Trends, Opportunities, Challenges and Applications to the Aerospatial Sector,” European Regional Development Fund, 2019.

[23] S.W. Williams, F. Martina, A.C. Addison, J. Ding, G. Pardal, and P. Colegrove, “Wire+ arc additive manufacturing,” *Materials Science and Technology*, vol. 32, no. 7, pp. 641-647, 2016.

[24] J.Z. Li, M.R. Alkahari, N.A. Rosli, R. Hasan, M. N. Sudin, and F.R. Ramli, “Review of Wire Arc Additive Manufacturing for 3D Metal Printing,” *International Journal of Automation*, vol. 13, no. 3, pp. 346-353, 2019.

[25] A. Anca, V.D. Fachinotti, G. Escobar Palafox, and A. Cardona, “Computational modelling of shaped metal deposition,” *International journal for numerical methods in engineering*, vol. 85, no. 1, pp. 84-106, 2011.

[26] J. González, I. Rodríguez, J. L. Prado-Cerqueira, J. L. Diéguez, and A. Pereira, “Additive manufacturing with GMAW welding and CMT technology,” *Procedia Manufacturing* , vol. 13, pp. 840-847, 2017.

[27] Z. Pan, D. Ding, B. Wu, D. Cuiuri, H. Li, and J. Norrish, “Arc welding processes for additive manufacturing: a review,” *Transactions on intelligent welding manufacturing* , pp. 3-24, 2018.

[28] P. Kah, H. Latifi, R. Suoranta, J. Martikainen, and M. Pirinen, “Usability of arc types in industrial welding,” *International Journal of Mechanical and Materials Engineering*, vol. 9, no. 1, pp. 1-12, 2014.

[29] S. Selvi, A. Vishvaksenan, and E. Rajasekar, “Cold metal transfer (CMT) technology-An overview,” *Defence technology*, vol. 14, no. 1, pp. 28-44, 2018.

[30] FRONIUS Team, “CMT: Cold Metal Transfer,” FRONIUS INTERNATIONAL. https://1library.net/document/y4kxvm9q-cmt-cold-metal-transfer-mig-mag-transfer-process.html, [May. 12, 2020].

[31] T. P. Hasselberg, “A Feasibility Study of “Cold Metal Transfer” – Gas Metal Arc Welding (CMT-GMAW) Nickel Base Superalloy Inconel 718™,”, MSc thesis, Rensselaer Polytechnic Institute, USA, 2009.

[32] N. R. Tailleart, F. J. Martin, R. J. Rayne, R. A. Bayles, A. Rubinoff, L. Levenberry, and P. M. Natishan, “Communication—Restoring the Pitting Resistance of Sensitized Duplex Stainless Steel Using Interstitial Hardening,” *Journal of The Electrochemical Society*, vol. 163, no. 8, p. C423, 2016.

[33] X. Xu, M. Zhao, Y. Feng, F. Li, and X. Zhang, “A Comparative Study of Critical Pitting Temperature (CPT) of Super Duplex Stainless Steel S32707 in NaCl Solution,” *International Journal of Electrochemcal Science*, vol. 13, pp. 4298-4308, 2018.

[34] J. Charles and P. Chemelle, “The history of duplex developments, nowadays DSS properties and duplex market future trends,” *World Iron & Steel*, vol. 1, pp. 46-57, 2012.

[35] V. Hosseini, “Super Duplex Stainless Steels – Microstructure and Properties of Physically Simulated Base and Weld Metal,” , PhD thesis, University West, Sweden, 2018.

[36] TMR Stainless Steel, “Practical guidelines for the fabrication of Duplex Stainless Steel,” International molybdenum, London, UK, 2014.

[37] K. Yurtisik, “Kinetice and Microstructure Analysis of Fatigue Fracture Progress in Weld Joints of Duples Stainless Steel Grade 2205,” , PhD thesis, Middle East Technical Universty, Turkey, 2013.

[38] R. Cervo, “Experimental and Numerical Analysis of Welding and Heat Treatment of Duplex Stainless Steels,” , PhD thesis, Università degli Studi di Padova, Italy, 2010.

[39] J. Charles, “Duplex Stainless Steels a Review after DSS ‘07 held in Grado,” *Steel Research International* , vol. 79, no. 6, pp. 455-465, 2008.

[40] K. Göransson, M-L. Nyman, M. Holmquist, and E. Gomes, “Sandvik SAF 2707 HD®(UNS S32707): a hyper-duplex stainless steel for severe chloride containing environments,” *Revue de Métallurgie ,* vol. 104, no. 9, pp. 411-417, 2007.

[41] M Knyazeva and M Pohl, “Duplex steels. Part II: carbides and nitrides,” *Metallography, microstructure, and analysis,* vol. 2, no. 5, pp. 343-351, 2013.

[42] S. Sharafi, “Microstructuer of Super- Duples Stainless Steel,” PhD thesis, University of Cambridge, UK, 1993.

[43] J. C. Lippold, D. J. Kotecki, *Welding Metallurgy and Weldability of Stainless Steel,* New Jersey: Jone Wiley & Sons, Inc., 2005.

[44] M. Knyazeva and M. Pohl, “Duplex steels: Part I: Genesis, formation, structure,” *Metallography, Microstructure, and Analysis* , vol. 2, no. 2, pp. 113-121, 2013.

[45] A. Vinoth Jebaraj, L. Ajaykumar, C. R. Deepak, and K. V. V. Aditya, “Weldability, machinability and surfacing of commercial duplex stainless steel AISI2205 for marine applications–A recent review,” *Journal of Advanced Research,* vol. 8, no. 3, pp. 183-199, 2017.

[46] API TECHNICAL REPORT 938-C, “Use of Duplex Stainless Steels in the Oil Refining Industry,” American Petroleum Institute, USA, 2011.

[47] S. Naskar, “IMPROVED CORROSION PERFORMANCE IN SUPER-DUPLEX WELDS,” sandvik research and development centre, Sweden , 2015.

[48] T. Pickle, N. Henry, P. Morriss, L. Tennis, D. Wagner, and R. E. Baumer, “Root pass microstructure in super duplex stainless steel multipass welds,” *Welding Journal* , vol. 98, no. 5, pp. 123s-134s, 2019.

[49] IIS Team, “Assessment of Planar Flaws Fracture Mechanics Basic Principles,” Istituto Italiano della Saldatura, Italy, 2004.

[50] G. Cornacchia, “Numerical Models and Experimental Simulation of Irradiation Hardening and Damage Effects on the Fracture Toughness of 316L Stainless Steel,” , PhD thesis, The University of Manchester, UK, 2012.

[51] Y. Huang, “Numerical Studies for Improving Fracture Toughness Resistance Curve Testing Using Single-Edge (Notched) Tension Specimens,” , PhD thesis, Western University, Canada, 2016.

[52] N. M. Dhansay, “Fracture Mechanics Based Fatigue and Fracture Toughness Evaluation of SLM Ti-6Al-4V,” , MSc thesis, University of Cape Town, South Africa, 2015.

[53] W.D. Callister, *Fundamentals of Materials Science and Engineering*. Fifth Edition, Ed., USA: John Wiley & Sons, Inc., 2001.

[54] T.L. Anderson, *Fracture Mechanics Fundamentals and Applications*. Third Edition ed., UK: Taylor & Francis Group, 2005.

[55] SLV Team, “The Welding Engineer´s Current Knowle,” German welding center, Germany, 2000.

[56] H. Sieurin, “Fracture Toughness Properties of Duplex Stainless Steels,” Royal Institute of Technology, Sweden, 2006.

[57] Z. Liu, X. Chen, and X. Wang, “Analysis of three-dimensional clamped single edge notched tension (SENT) specimens,” in *Pressure Vessels and Piping Conference*, 2018.

[58] C. Soret, Y. Madi, J. Besson and V. Gaffard, “Use of the Sent Specimen in Pipeline Design,” in *20th JTM- EPRG European pipeline research group*, Paris, France, 2015.

[59] P. L. Moore and A. M. Crintea, “Single Edge Notched Tension (SENT) Testing At Low Temperatures,” in *11th International Pipeline Conference IPC2016*, , UK, 2016.

[60] P. Moore, “Optimisation of SENT test specimen design,” in *Eurojoin 9 conference*, Norway, 2015.

[61] The International Organization for Standardization, “Metallic materials — Unified method of test for the determination of quasistatic fracture toughness,” ISO 12135, Second edition, 2016.

[62] British Standards Institution, “Method of Test for Determination of Fracture Toughness in Metallic Materials Using Single Edge Notched Tension (SENT) Specimens,” BS 8571, 2018.

[63] J. Nilsson, “Super duplex stainless steels,” *Materials science and technology* , vol. 8, no. 8, pp. 685-700, 1992.

[64] T.J. Marrow, “Brittle Fracture of Duplex Stainless Steel,” in *12th European Conference on Fracture (ECF12)*, UK, 1998.

[65] J. Pilhagen, “The Fracture Mechanisms in Duplex Stainless Steels at Sub-zero Temperatures,” Royal Institute of Technology, Sweden, 2013.

[66] Stat-Ease, Inc. 2007. Design-Expert® Software, V7, USA.

[67] COMSOL, Multiphysics®, “V. 5.6. www.comsol.com. COMSOL AB, Stockholm, Sweden.”.

[68] V. Gunaraj and N. Murugan, “Prediction and optimization of weld bead volume for the submerged arc process—part 1,” *Welding journal*, vol. 79, no. 10, pp. 286s-294s, 2000.

[69] D. C. Montgomery, *Design and Analysis of Experiments*. John Wiley &Sons, 2001.

[70] V. A. Kostin and G. M. Grygorenko, “Simulation of the Additive Process of Forming 3D Products from HSLA Steel 09G2S,” in *Proceedings of the COMSOL Conference*, Rotterdam, Holland, 2017.

[71] M. T. Santos, P. V. Muterlle and G. C. Carvalho, “Emissivity Caracterization in Stainless Steels Alloys for Application in Hidroeletric Turbines,” *Applied Mechanics and Materials,* vol. 719, pp. 3-12, 2015.

[72] C. R. Xavier, H. G. Delgado, and J. A. de Castro, “An experimental and numerical approach for the welding effects on the duplex stainless steel microstructure,” *Materials Research,* vol. 18, no. 3, pp. 489-502, 2015.

[73] ASTM Subcommitte A01.17, ASTM A240, “Standard Specification for Chromium and Chromium-Nickel Stainless Steel Plate, Sheet, and Strip for Pressure Vessels and for General Applications,” American Society for Testing and Materials, USA, 2005.

[74] European Standard, DIN EN 10088-2, “Stainless Steels - Part 2: Technical Delivery Conditions For Sheet/Plate And Strip Of Corrosion Resisting Steels For General Purposes,” Deutsches Institut fur Normung E.V. (DIN), Germany, 2000.

[75] ESAB Team, “Welding Filler Metal Data book,” ESAB, USA, 2016.

[76] ASTM E1742, “Standard Practice for Radiographic Examination,” American Society for Testing and Material, USA, 2012.

[77] ASME Committe, “ASME Boiler and Pressure Vessel Code, New York:,” The American Society of Mechanical Engineers, USA, 2011.

[78] ASTM Subcommitte E28.04, ASTM E8, “Standard Practice for Radiographic Examination,” American Society for Testing and Materials, USA, 2013.

[79] The International Organization for Standardization, “Metallic materials – Vickers hardness test - Part 1: Test method,” ISO 6507-1, 2018.

[80] ASTM Subcommitte E04.08, ASTM E112, “Standard Test Methods for Determining Average Grain Size,” American Society for Testing and Materials, USA, 2012.

[81] ASTM Subcommitte E04.14, ASTM E562, “Standard Test Method for Determining Volume Fraction by Systematic Manual Point Count,” American Society for Testing and Materials, USA, 2011.

[82] ASTM Subcommitte E04.14, ASTM E1245, “Practice for Determining the Inclusion or Second Phase Constituent Content of Metals by Automatic Image Analysis,” American Society fot Testing and Materials, USA, 2011.

[83] W. Rasband, ImageJ, National Institutes of Health, Bethesda, Maryland, USA, 1997-2018..

[84] A. Putz , M. Althuber, A. Zelić, E. M. Westin, T. Willidal, and N. Enzinger, “Methods for the measurement of ferrite content in multipass duplex stainless steel welds,” *Welding in the World 63, no. 4 (2019):* , vol. 63, no. 4, pp. 1075-1086, 2019.

[85] The International Organization for Standardization, “Petroleum, petrochemical, and natural gas industries — Materials for use in H2S-containing environments in oil and gas production,” ANSI/NACE MR0175/ISO 15156-1, 2015.

[86] R. Mohammed, G. M. Reddy, and K. S. Rao, “Effect of Welding Process on Microstructure, Mechanical and Pitting Corrosion Behaviour of 2205 Duplex Stainless Steel Welds,” in *IOP Conference Series: Materials Science and Engineering*, IOP Publishing, 2018.

[87] V. Hosseini, K. Hurtig, D. Eyzop, A. Östberg, P. Janiak and L. Karlsson, “Ferrite content measurement in super duplex stainless steel welds,” *Welding in the World 63, no. 2 (2019),* vol. 63, no. 2, pp. 551-563, 2019.

[88] Sandvik Team, “Sandvik SAF 2507,” Sandvik Research and Development Centre, Sweden, 2020.

[89] MATLAB and statistics Toolbox R2013a, The MathWorks, Inc., Natick, Massachusetts, United States.

APPENDIX A

**The Developed Matlab Codes to calculate the crack length and J value**

```
%Calculate the crack length
clc
filename = 'AM.xlsx';   % Excel file name
B = xlsread(filename,1); % Sheet 1
W = xlsread(filename,2); % Sheet 2
P1=B(:,1);
ao1=B(:,2);
af1=B(:,3);
P2=B(:,4);
ao2=B(:,5);
af2=B(:,6);
P3=B(:,7);
ao3=B(:,8);
af3=B(:,9);
P4=B(:,10);
ao4=B(:,11);
af4=B(:,12);
P5=B(:,13);
ao5=B(:,14);
af5=B(:,15);
P6=B(:,16);
ao6=B(:,17);
af6=B(:,18);
a11=(((ao1(1)+ao1(9))/2)+ao1(2)+ao1(3)+ao1(4)+ao1(5)+ao1(6)+ao1(7)+ao1(8))/8;
a21=(((af1(1)+af1(9))/2)+af1(2)+af1(3)+af1(4)+af1(5)+af1(6)+af1(7)+af1(8))/8;
a12=(((ao2(1)+ao2(9))/2)+ao2(2)+ao2(3)+ao2(4)+ao2(5)+ao2(6)+ao2(7)+ao2(8))/8;
a22=(((af2(1)+af2(9))/2)+af2(2)+af2(3)+af2(4)+af2(5)+af2(6)+af2(7)+af2(8))/8;
a13=(((ao3(1)+ao3(9))/2)+ao3(2)+ao3(3)+ao3(4)+ao3(5)+ao3(6)+ao3(7)+ao3(8))/8;
a23=(((af3(1)+af3(9))/2)+af3(2)+af3(3)+af3(4)+af3(5)+af3(6)+af3(7)+af3(8))/8;
a14=(((ao4(1)+ao4(9))/2)+ao4(2)+ao4(3)+ao4(4)+ao4(5)+ao4(6)+ao4(7)+ao4(8))/8;
a24=(((af4(1)+af4(9))/2)+af4(2)+af4(3)+af4(4)+af4(5)+af4(6)+af4(7)+af4(8))/8;
a15=(((ao5(1)+ao5(9))/2)+ao5(2)+ao5(3)+ao5(4)+ao5(5)+ao5(6)+ao5(7)+ao5(8))/8;
a25=(((af5(1)+af5(9))/2)+af5(2)+af5(3)+af5(4)+af5(5)+af5(6)+af5(7)+af5(8))/8;
a16=(((ao6(1)+ao6(9))/2)+ao6(2)+ao6(3)+ao6(4)+ao6(5)+ao6(6)+ao6(7)+ao6(8))/8;
a26=(((af6(1)+af6(9))/2)+af6(2)+af6(3)+af6(4)+af6(5)+af6(6)+af6(7)+af6(8))/8;
del1=a21-a11;
del2=a22-a12;
del3=a23-a13;
del4=a24-a14;
del5=a25-a15;
del6=a26-a16;
PW1=W(:,1);
```

```
wo1=W(:,2);
wf1=W(:,3);
PW2=W(:,4);

wo2=W(:,5);
wf2=W(:,6);
PW3=W(:,7);
wo3=W(:,8);
wf3=W(:,9);
PW4=W(:,10);
wo4=W(:,11);
wf4=W(:,12);
PW5=W(:,13);
wo5=W(:,14);
wf5=W(:,15);
PW6=W(:,16);
wo6=W(:,17);
wf6=W(:,18);
w11=(((wo1(1)+wo1(9))/2)+wo1(2)+wo1(3)+wo1(4)+wo1(5)+wo1(6)+wo1(7)+wo1
(8))/8;
w21=(((wf1(1)+wf1(9))/2)+wf1(2)+wf1(3)+wf1(4)+wf1(5)+wf1(6)+wf1(7)+wf1(8))
/8;
w12=(((wo2(1)+wo2(9))/2)+wo2(2)+wo2(3)+wo2(4)+wo2(5)+wo2(6)+wo2(7)+wo2
(8))/8;
w22=(((wf2(1)+wf2(9))/2)+wf2(2)+wf2(3)+wf2(4)+wf2(5)+wf2(6)+wf2(7)+wf2(8))
/8;
w13=(((wo3(1)+wo3(9))/2)+wo3(2)+wo3(3)+wo3(4)+wo3(5)+wo3(6)+wo3(7)+wo3
(8))/8;
w23=(((wf3(1)+wf3(9))/2)+wf3(2)+wf3(3)+wf3(4)+wf3(5)+wf3(6)+wf3(7)+wf3(8))
/8;
w14=(((wo4(1)+wo4(9))/2)+wo4(2)+wo4(3)+wo4(4)+wo4(5)+wo4(6)+wo4(7)+wo4
(8))/8;
w24=(((wf4(1)+wf4(9))/2)+wf4(2)+wf4(3)+wf4(4)+wf4(5)+wf4(6)+wf4(7)+wf4(8))
/8;
w15=(((wo5(1)+wo5(9))/2)+wo5(2)+wo5(3)+wo5(4)+wo5(5)+wo5(6)+wo5(7)+wo5
(8))/8;
w25=(((wf5(1)+wf5(9))/2)+wf5(2)+wf5(3)+wf5(4)+wf5(5)+wf5(6)+wf5(7)+wf5(8))
/8;
w16=(((wo6(1)+wo6(9))/2)+wo6(2)+wo6(3)+wo6(4)+wo6(5)+wo6(6)+wo6(7)+wo6
(8))/8;
w26=(((wf6(1)+wf6(9))/2)+wf6(2)+wf6(3)+wf6(4)+wf6(5)+wf6(6)+wf6(7)+wf6(8))
/8;
del11=w21-w11;
del22=w22-w12;
del33=w23-w13;
del44=w24-w14;
del55=w25-w15;
```

```
del66=w26-w16;
aoB=[a11 a12 a13 a14 a15 a16];
afB=[a21 a22 a23 a24 a25 a26];
aoW=[w11 w12 w13 w14 w15 w16];
afW=[w21 w22 w23 w24 w25 w26];
DB=[del1 del2 del3 del4 del5 del6];
DW=[del11 del22 del33 del44 del55 del66];
Pb=[P1 P2 P3 P4 P5 P6];
Pw=[PW1 PW2 PW3 PW4 PW5 PW6];
%============================================================
===================
% Rolled Plate files
%filename1 = 'b1.xls';
%filename1 = 'b2.xls';
%filename1 = 'b3.xls';
%filename1 = 'b4.xls';
%filename1 = 'b5.xls';
%filename1 = 'b6.xls';
%=====================
%%WAAM'd plate files
%filename1 = 'w1.xls';
%filename1 = 'w2.xls';
%filename1 = 'w3.xls';
filename1 = 'w4.xls';   %RRR
%filename1 = 'w5.xls';
%filename1 = 'w6.xls';
%=====================
AA = xlsread(filename1,1);
H=AA(:,4);
V=AA(:,3);
plot(H,V)
 hold on
[x,y]=ginput(2);
s=(y(2)-y(1))/(x(2)-x(1));
H2=H(size(H));
V2=V(size(V));
n=H2(1)-(V2(1)/s);
Ph=[n,H2(1)];
Pv=[0,V2(1)];
plot(Ph,Pv,'k')
%plot(x,y,'r')
n1=x(1)+((V2(1)-y(1))/s);
ph1=[x(1),n1];
pv1=[y(1),V2(1)];
plot(ph1,pv1,'r');
AA1=trapz(H,V);
AA2=trapz(Ph,Pv);
```

```
AA3=(H2(1)-n)*(V2(1))/2;
xlabel('CMOD (mm) ')
ylabel('Force (N) ')
hold off
B1=AA(1,6);
W1=AA(1,5);
Up1=AA1-AA2;
Pf1=V2(1);
%===================================================
%a0=aoB(1);
%a0=aoB(2);
%a0=aoB(3);
%a0=aoB(4);
%a0=aoB(5);
%a0=aoB(6);
%a0=aoW(1);
%a0=aoW(2);
%a0=aoW(3);
a0=aoW(4);
%a0=aoW(5);
%a0=aoW(6);
t=[1.197 -2.133 23.886 -69.051 100.462 -41.397 -36.137 51.215 -6.607 -52.322
18.574 19.465];
Q=[1 -1.089 9.519 -48.572 109.225 -73.116 -77.984 38.487 101.401 43.306 -
110.770];
E=195000;
V=0.3;
%%%%
Aw1=a0/W1;
for i=1:12;
   G(i)=t(i)*((Aw1)^(i-1));
end;
for k=1:11;
   n(k)=Q(k)*((Aw1)^(k-1));
end;
G1=sum(G);
n1=sum(n);
K1=Pf1*sqrt(pi*a0)*G1/(W1*sqrt(B1*B1));
E1=E/(1-(V^2));
bo=W1-a0;
Je1=((K1^2)/E1);
Jp1=((n1*Up1)/(B1*bo));
J1=Je1+Jp1;
a0
Up1
J1
```

# APPENDIX B

## Fracture Surface and Load-CMOD Curve of Rolled Plate and Additively Manufactured Plate

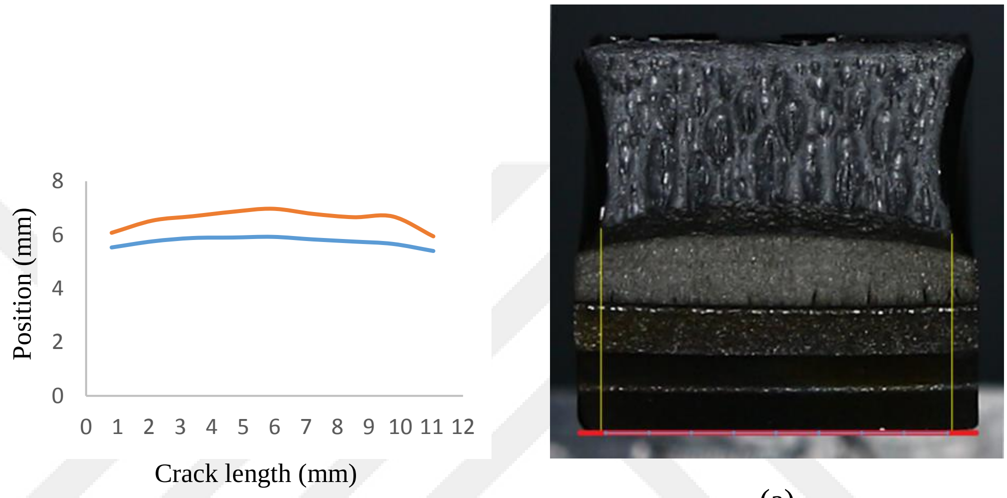


(a)

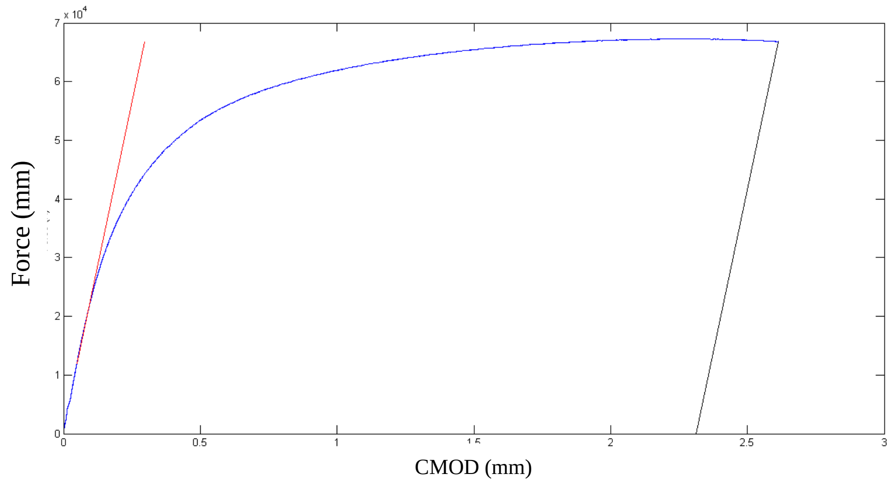


(b)

Figure B.1 a. a) Fracture surface, (b) Load-CMOD of Grade 2507 sample 1

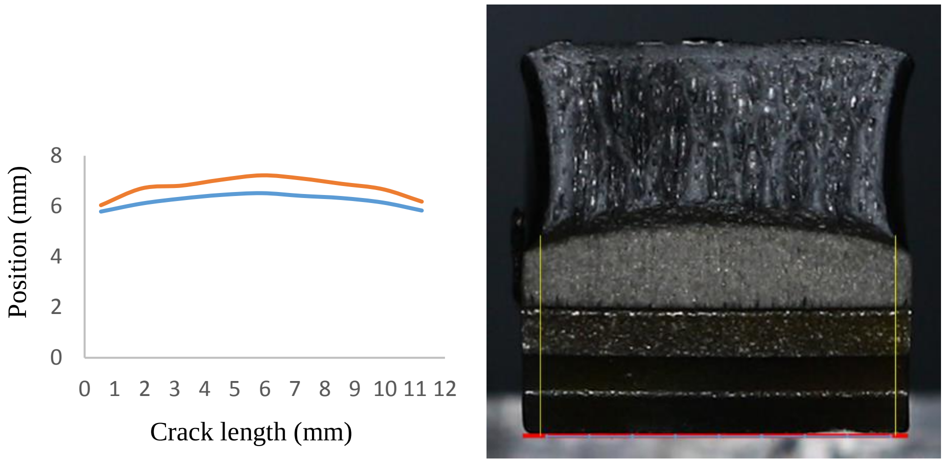


(a)

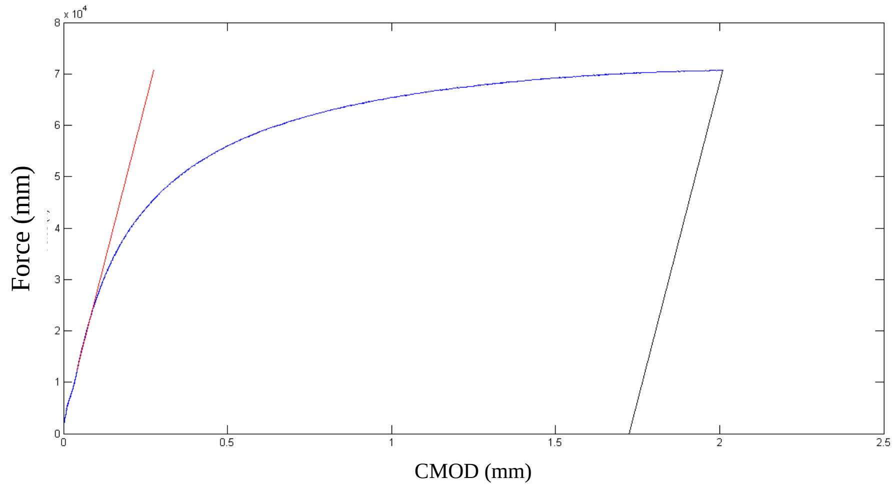


(b)

Figure B.2 a. a) Fracture surface, (b) Load-CMOD of Grade 2507 sample 2

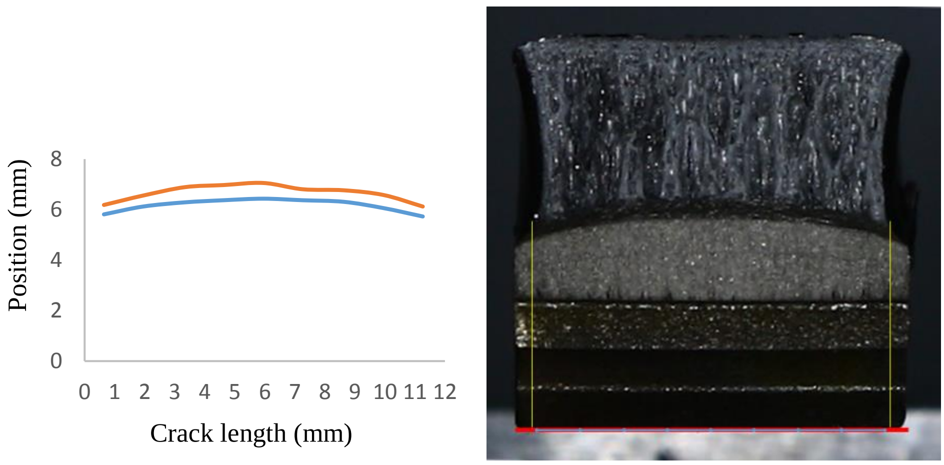


(a)

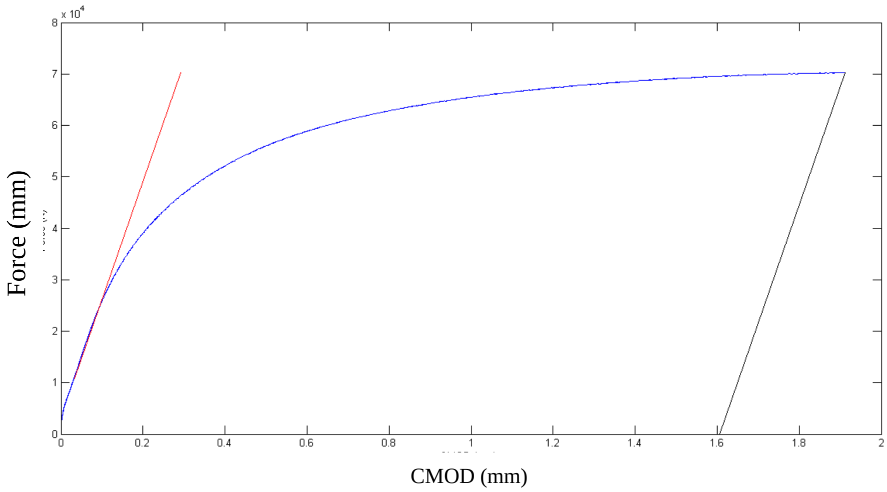


(b)

Figure B.3 a. a) Fracture surface, (b) Load-CMOD of Grade 2507 sample 3

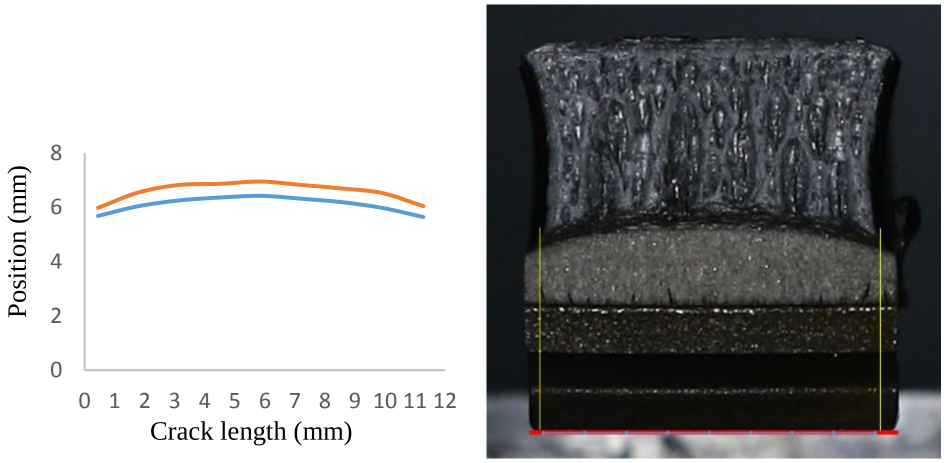


(a)

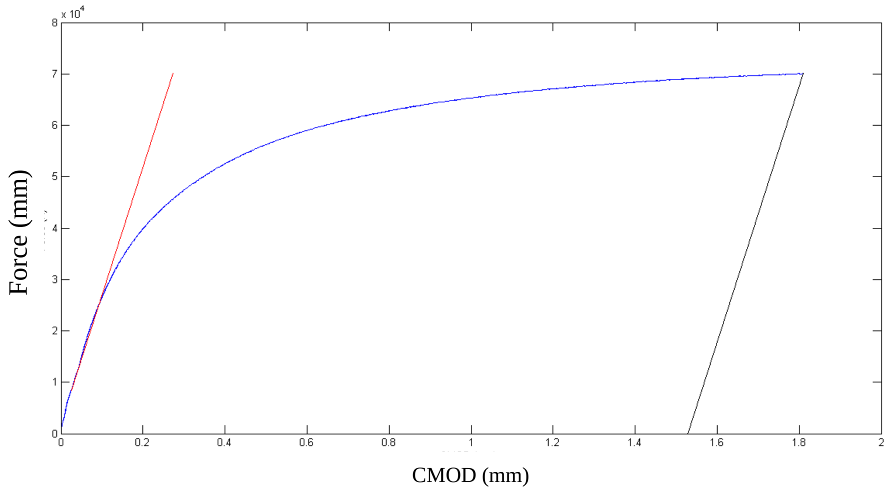


(b)

Figure B.4 a. a) Fracture surface, (b) Load-CMOD of Grade 2507 sample 4

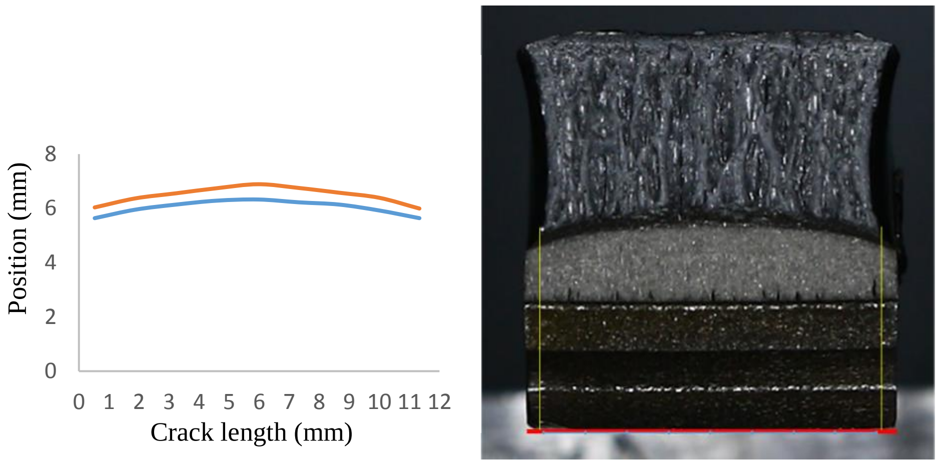


(a)

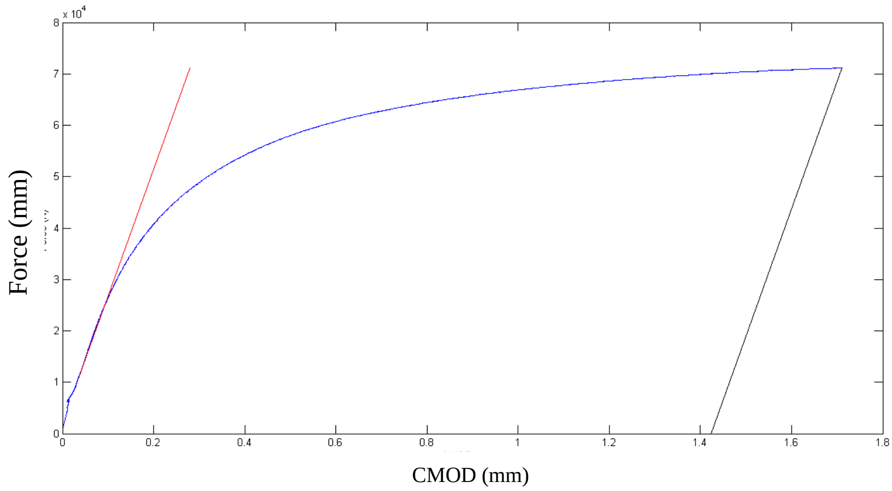


(b)

Figure B.5 a. a) Fracture surface, (b) Load-CMOD of Grade 2507 sample 5

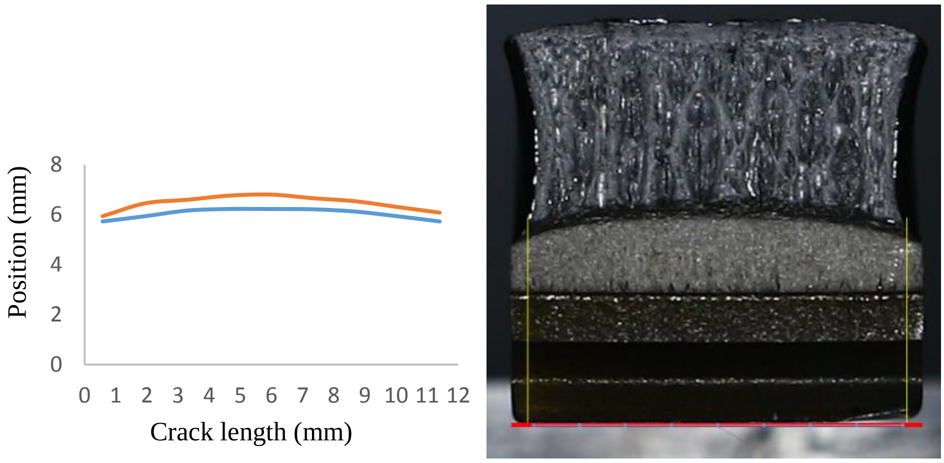


(a)

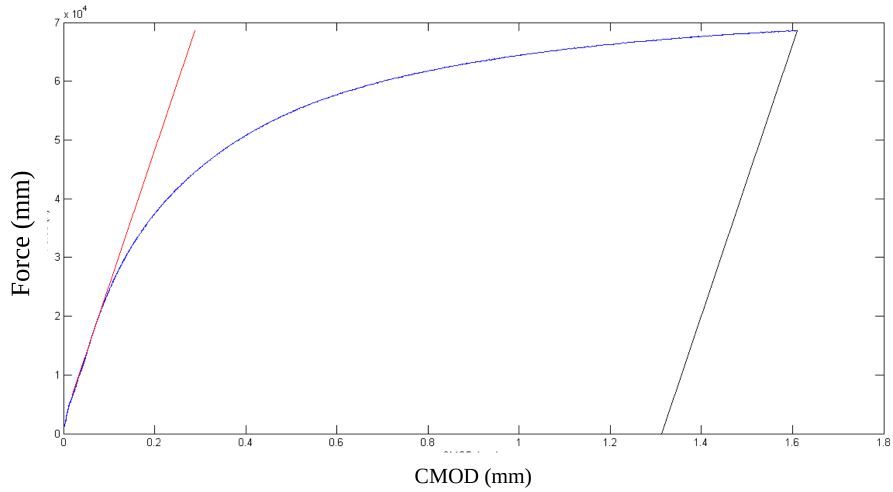


(b)

Figure B.6 a. a) Fracture surface, (b) Load-CMOD of Grade 2507 sample 6

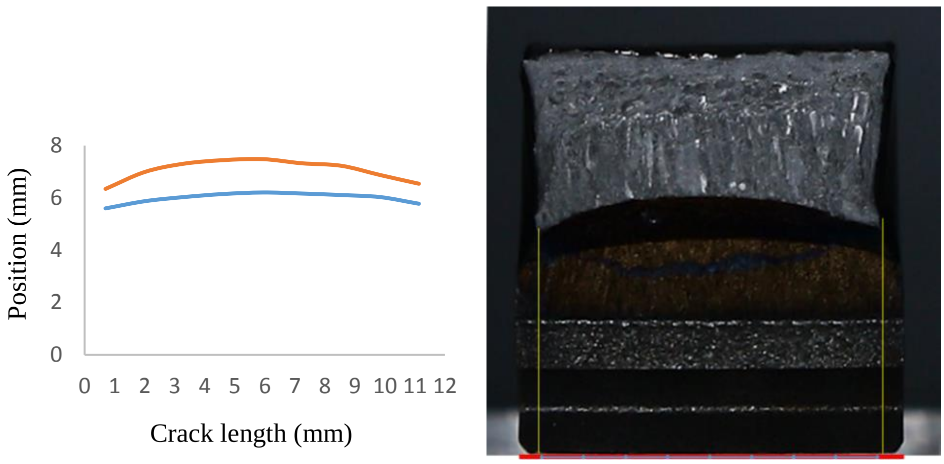


(a)

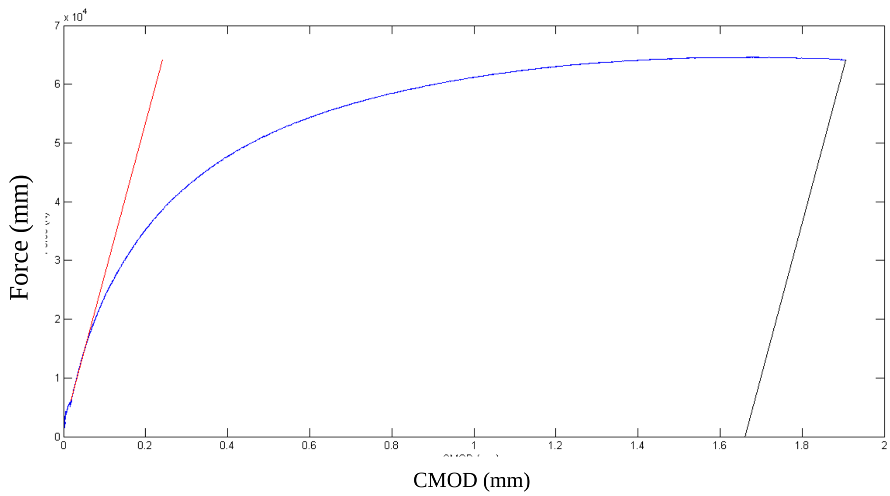


(b)

Figure B.7 a. Fracture surface, (b) Load-CMOD of Grade 2209 sample 1

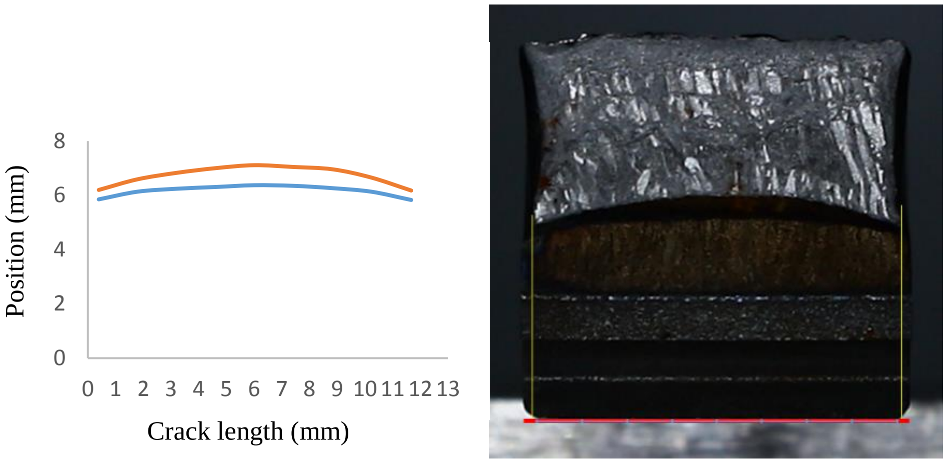


(a)

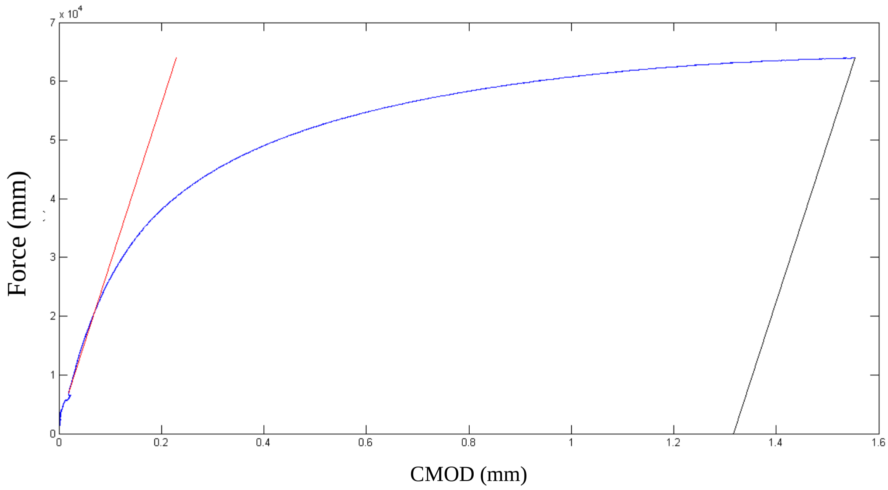


(b)

Figure B.8 a. Fracture surface, (b) Load-CMOD of Grade 2209 sample 2

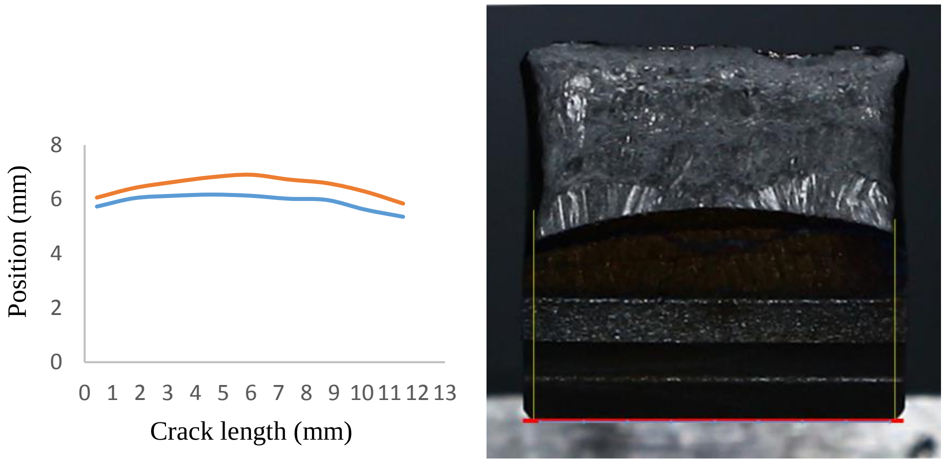


(a)

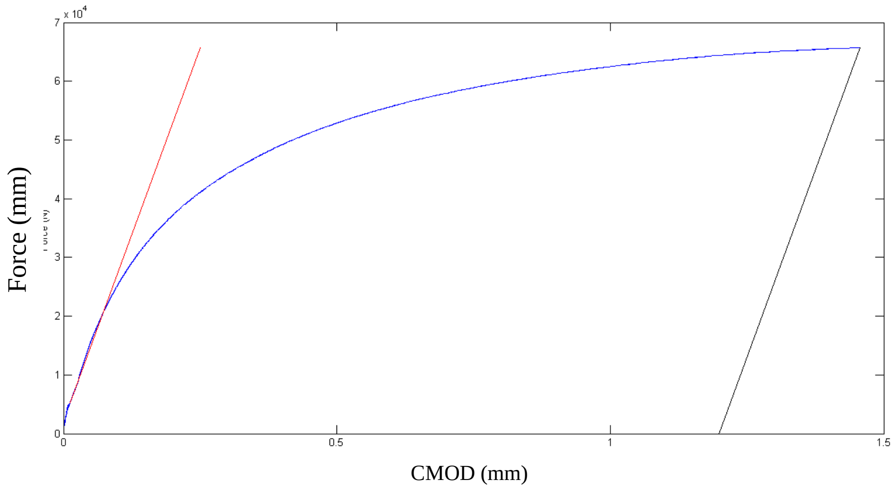


(b)

Figure B.9 a. Fracture surface, (b) Load-CMOD of Grade 2209 sample 3

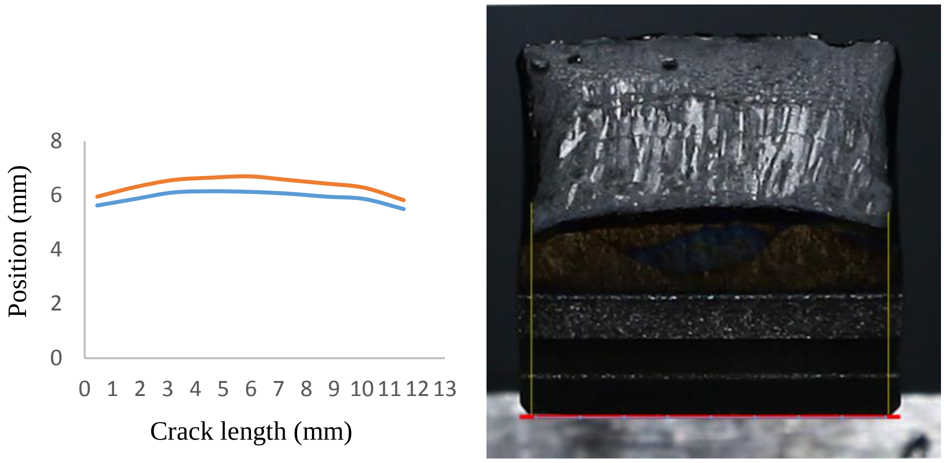


(a)

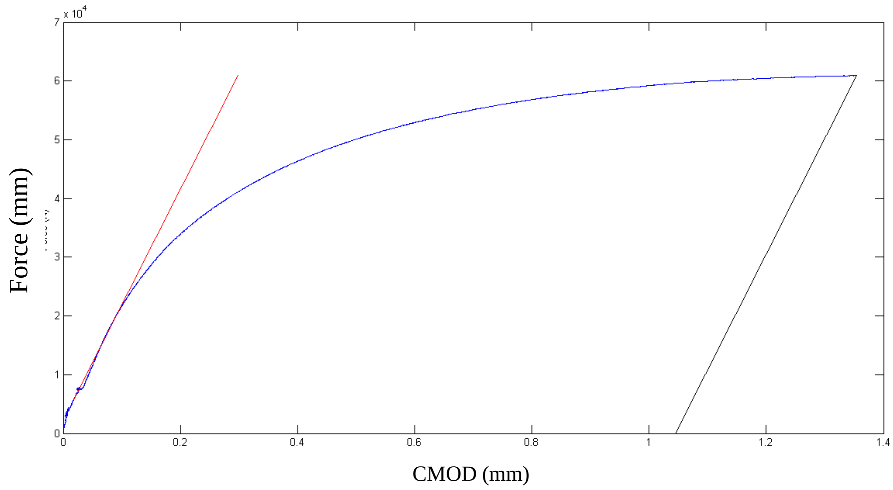


(b)

Figure B.10 a. Fracture surface, (b) Load-CMOD of Grade 2209 sample 4

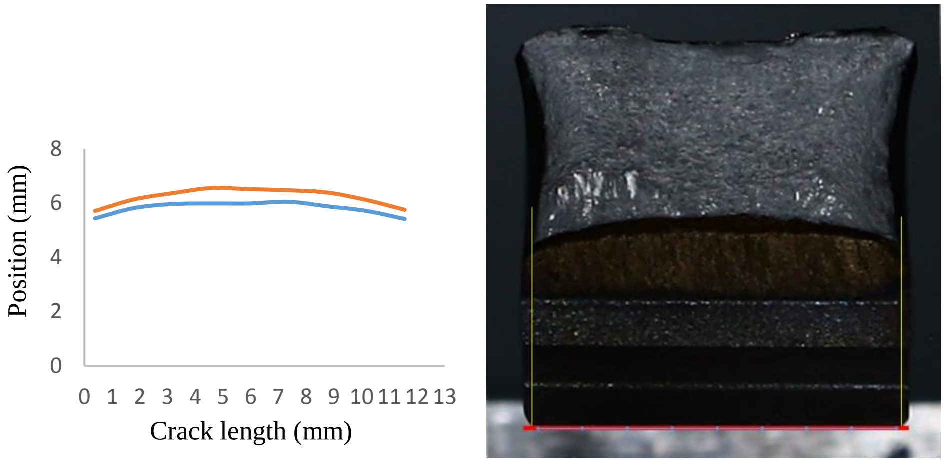


(a)

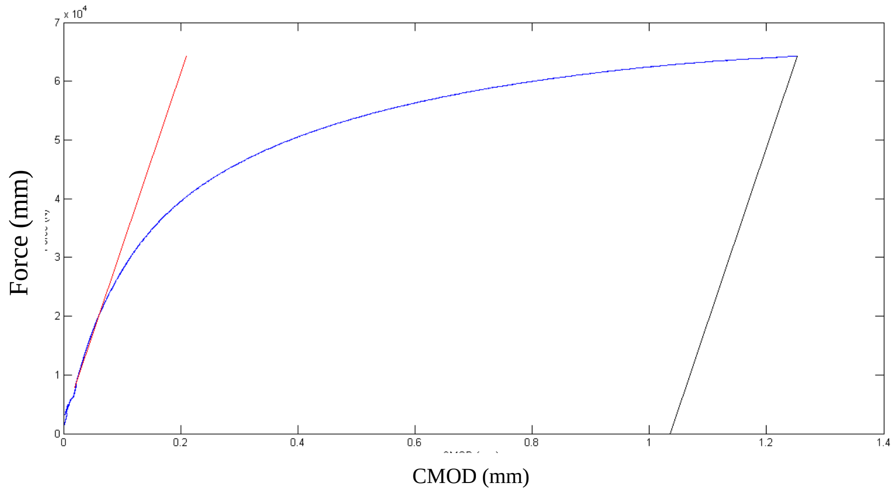


(b)

Figure B.11 a. Fracture surface, (b) Load-CMOD of Grade 2209 sample 5

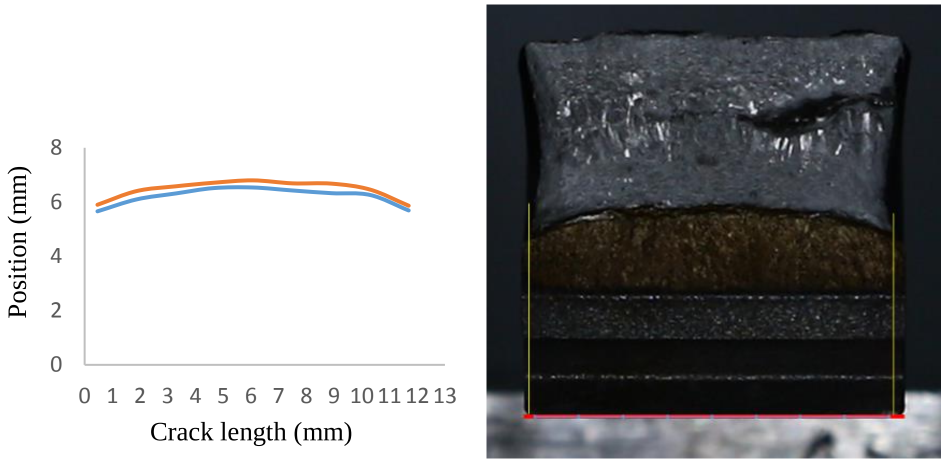


(a)

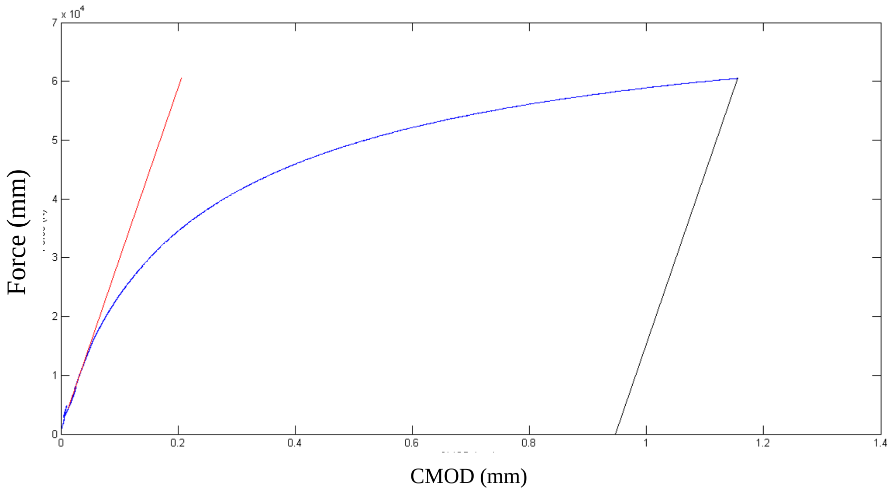


(b)

Figure B.12 a. Fracture surface, (b) Load-CMOD of Grade 2209 sample 6

.

**APPENDIX C**

**Crack Length Measurements of Rolled Plate and Additively Manufactured Plate**

Table C.1 Crack length of as-received SDSS plate Grade 2507 sample 1

| Specimen | SDSS Grade 2509 (1) | |
|---|---|---|
| Width (mm) | 12.05 (mm) | |
| Thickness (mm) | 12.06 (mm) | |
| position | $a_0$ | $a_f$ |
| 0.813 | 5.531 | 6.077 |
| 2.124 | 5.76 | 6.535 |
| 3.394 | 5.883 | 6.694 |
| 4.664 | 5.901 | 6.861 |
| 5.934 | 5.927 | 6.974 |
| 7.225 | 5.83 | 6.782 |
| 8.515 | 5.751 | 6.658 |
| 9.765 | 5.663 | 6.685 |
| 11.055 | 5.399 | 5.945 |
| $\mathbf{a_0}$ (mm) | 5.773 | |
| $\mathbf{a_f}$ (mm) | 6.650 | |
| $\Delta$**a** (mm) | 0.878 | |

Table C.2 Crack length of as-received SDSS plate Grade 2507 sample 2

| Specimen | SDSS Grade 2509 (2) | |
|---|---|---|
| Width (mm) | 12.08 (mm) | |
| Thickness (mm) | 12.07 (mm) | |
| position | $a_0$ | $a_f$ |
| 0.544 | 5.790 | 6.043 |
| 1.911 | 6.110 | 6.710 |
| 3.236 | 6.307 | 6.819 |
| 4.54 | 6.449 | 7.049 |
| 5.907 | 6.519 | 7.225 |
| 7.211 | 6.413 | 7.102 |
| 8.557 | 6.325 | 6.890 |
| 9.925 | 6.148 | 6.678 |
| 11.229 | 5.831 | 6.184 |
| $\mathbf{a_0}$ (mm) | 6.260 | |
| $\mathbf{a_f}$ (mm) | 6.823 | |
| $\Delta$**a** (mm) | 0.563 | |

Table C.3 Crack length of as-received SDSS plate Grade 2507 sample 3

| Specimen | SDSS Grade 2509 (3) | |
|---|---|---|
| Width (mm) | 12.03 (mm) | |
| Thickness (mm) | 12.08 (mm) | |
| position | $a_0$ | $a_f$ |
| 0.642 | 5.811 | 6.184 |
| 1.949 | 6.122 | 6.557 |
| 3.338 | 6.288 | 6.889 |
| 4.624 | 6.371 | 6.972 |
| 5.952 | 6.433 | 7.055 |
| 7.259 | 6.371 | 6.806 |
| 8.628 | 6.309 | 6.765 |
| 9.955 | 6.060 | 6.578 |
| 11.262 | 5.728 | 6.122 |
| $\mathbf{a_0}$ (mm) | 6.215 | |
| $\mathbf{a_f}$ (mm) | 6.722 | |
| $\Delta$**a** (mm) | 0.506 | |

Table C.4 Crack length of as-received SDSS plate Grade 2507 sample 4

| Specimen | SDSS Grade 2509 (4) | |
|---|---|---|
| Width (mm) | 12.05 (mm) | |
| Thickness (mm) | 12.07 (mm) | |
| position | $a_0$ | $a_f$ |
| 0.444 | 5.686 | 5.982 |
| 1.799 | 6.045 | 6.551 |
| 3.153 | 6.256 | 6.826 |
| 4.508 | 6.362 | 6.868 |
| 5.884 | 6.425 | 6.952 |
| 7.217 | 6.319 | 6.826 |
| 8.55 | 6.193 | 6.699 |
| 9.905 | 5.982 | 6.530 |
| 11.28 | 5.644 | 6.045 |
| $\mathbf{a_0}$ (mm) | 6.156 | |
| $\mathbf{a_f}$ (mm) | 6.658 | |
| $\Delta$**a** (mm) | 0.502 | |

Table C.5 Crack length of as-received SDSS plate Grade 2507 sample 5

| Specimen | SDSS Grade 2509 (5) | |
|---|---|---|
| Width (mm) | 12.06 (mm) | |
| Thickness (mm) | 12.05 (mm) | |
| position | $a_0$ | $a_f$ |
| 0.525 | 5.639 | 6.035 |
| 1.881 | 5.954 | 6.369 |
| 3.237 | 6.140 | 6.556 |
| 4.594 | 6.285 | 6.744 |
| 5.971 | 6.327 | 6.890 |
| 7.327 | 6.223 | 6.751 |
| 8.662 | 6.140 | 6.577 |
| 9.998 | 5.922 | 6.390 |
| 11.333 | 5.639 | 5.994 |
| $\mathbf{a_0}$ (mm) | 6.079 | |
| $\mathbf{a_f}$ (mm) | 4.053 | |
| $\Delta\mathbf{a}$ (mm) | 0.458 | |

Table C.6 Crack length of as-received SDSS plate Grade 2507 sample 6

| Specimen | SDSS Grade 2509 (6) | |
|---|---|---|
| Width (mm) | 12 (mm) | |
| Thickness (mm) | 12.06 (mm) | |
| position | $a_0$ | $a_f$ |
| 0.577 | 5.733 | 5.942 |
| 1.938 | 5.942 | 6.458 |
| 3.299 | 6.169 | 6.602 |
| 4.639 | 6.231 | 6.767 |
| 6 | 6.231 | 6.808 |
| 7.34 | 6.220 | 6.664 |
| 8.701 | 6.128 | 6.540 |
| 10.041 | 5.942 | 6.313 |
| 11.402 | 5.733 | 6.087 |
| $\mathbf{a_0}$ (mm) | 6.075 | |
| $\mathbf{a_f}$ (mm) | 6.521 | |
| $\Delta\mathbf{a}$ (mm) | 0.446 | |

Table C.7 Crack length of WAAM'd DSS Grade 2209 sample 1

| Specimen | DSS Grade 2209 (1) | |
|---|---|---|
| Width (mm) | 12.03 (mm) | |
| Thickness (mm) | 12.08 (mm) | |
| position | $a_0$ | $a_f$ |
| 0.697 | 5.600 | 6.346 |
| 2.006 | 5.875 | 6.993 |
| 3.296 | 6.032 | 7.307 |
| 4.606 | 6.149 | 7.444 |
| 5.935 | 6.208 | 7.483 |
| 7.224 | 6.169 | 7.326 |
| 8.553 | 6.110 | 7.228 |
| 9.843 | 6.032 | 6.875 |
| 11.133 | 5.777 | 6.542 |
| $\mathbf{a_0}$ (mm) | 6.033 | |
| $\mathbf{a_f}$ (mm) | 7.138 | |
| $\Delta$**a** (mm) | 1.105 | |

Table C.8 Crack length of WAAM'd DSS Grade 2209 sample 2

| Specimen | DSS Grade 2209 (2) | |
|---|---|---|
| Width (mm) | 12 (mm) | |
| Thickness (mm) | 12.09 (mm) | |
| position | $a_0$ | $a_f$ |
| 0.393 | 5.853 | 6.200 |
| 1.789 | 6.135 | 6.591 |
| 3.207 | 6.244 | 6.830 |
| 4.625 | 6.309 | 7.004 |
| 6 | 6.374 | 7.112 |
| 7.418 | 6.352 | 7.047 |
| 8.836 | 6.265 | 6.960 |
| 10.233 | 6.135 | 6.656 |
| 11.673 | 5.831 | 6.179 |
| $\mathbf{a_0}$ (mm) | 6.207 | |
| $\mathbf{a_f}$ (mm) | 6.799 | |
| $\Delta$**a** (mm) | 0.592 | |

Table C.9 Crack length of WAAM'd DSS Grade 2209 sample 3

| Specimen | DSS Grade 2209 (3) | |
|---|---|---|
| Width (mm) | 12.03 (mm) | |
| Thickness (mm) | 12.02 (mm) | |
| position | $a_0$ | $a_f$ |
| 0.444 | 5.735 | 6.067 |
| 1.797 | 6.045 | 6.421 |
| 3.216 | 6.133 | 6.642 |
| 4.591 | 6.177 | 6.819 |
| 5.989 | 6.133 | 6.908 |
| 7.364 | 6.023 | 6.731 |
| 8.739 | 5.978 | 6.598 |
| 10.115 | 5.624 | 6.288 |
| 11.49 | 5.359 | 5.846 |
| $\mathbf{a_0}$ (mm) | 5.958 | |
| $\mathbf{a_f}$ (mm) | 6.545 | |
| $\Delta\mathbf{a}$ (mm) | 0.588 | |

Table C.10 Crack length of WAAM'd DSS Grade 2209 sample 4

| Specimen | DSS Grade 2209 (4) | |
|---|---|---|
| Width (mm) | 12.05 (mm) | |
| Thickness (mm) | 12.04 (mm) | |
| position | $a_0$ | $a_f$ |
| 0.455 | 5.627 | 5.954 |
| 1.813 | 5.867 | 6.304 |
| 3.192 | 6.107 | 6.566 |
| 4.572 | 6.151 | 6.653 |
| 5.952 | 6.129 | 6.700 |
| 7.353 | 6.063 | 6.566 |
| 8.711 | 5.954 | 6.435 |
| 10.09 | 5.867 | 6.282 |
| 11.514 | 5.496 | 5.823 |
| $\mathbf{a_0}$ (mm) | 5.962 | |
| $\mathbf{a_f}$ (mm) | 6.424 | |
| $\Delta\mathbf{a}$ (mm) | 0.462 | |

Table C.11 Crack length of WAAM'd DSS Grade 2209 sample 5

| Specimen | DSS Grade 2209 (5) | |
|---|---|---|
| Width (mm) | 12.01 (mm) | |
| Thickness (mm) | 12.02 (mm) | |
| position | $a_0$ | $a_f$ |
| 0.382 | 5.438 | 5.713 |
| 1.781 | 5.819 | 6.136 |
| 3.18 | 5.967 | 6.368 |
| 4.58 | 5.988 | 6.558 |
| 5.958 | 5.988 | 6.516 |
| 7.378 | 6.051 | 6.474 |
| 8.777 | 5.882 | 6.389 |
| 10.177 | 5.713 | 6.115 |
| 11.555 | 5.417 | 5.755 |
| $\mathbf{a_0}$ (mm) | 5.854 | |
| $\mathbf{a_f}$ (mm) | 6.286 | |
| $\Delta\mathbf{a}$ (mm) | 0.432 | |

Table C.12 Crack length of WAAM'd DSS Grade 2209 sample 6

| Specimen | DSS Grade 2209 (6) | |
|---|---|---|
| Width (mm) | 12.01 (mm) | |
| Thickness (mm) | 12.05 (mm) | |
| position | $a_0$ | $a_f$ |
| 0.463 | 5.658 | 5.899 |
| 1.875 | 6.097 | 6.404 |
| 3.287 | 6.316 | 6.580 |
| 4.654 | 6.514 | 6.711 |
| 6.066 | 6.536 | 6.799 |
| 7.5 | 6.426 | 6.689 |
| 8.912 | 6.326 | 6.678 |
| 10.301 | 6.260 | 6.458 |
| 11.691 | 5.690 | 5.865 |
| $\mathbf{a_0}$ (mm) | 6.269 | |
| $\mathbf{a_f}$ (mm) | 6.525 | |
| $\Delta\mathbf{a}$ (mm) | 0.257 | |